

Photon-assisted spectroscopy of electronic interface states in perovskite oxide heterostructures

Dissertation

zur Erlangung des akademischen Grades

Doctor rerum naturalium

(Dr. rer. nat.)

vorgelegt von

Dipl.-Phys. Elke Beyreuther

geboren am 26.03.1979 in Dresden

Institut für Angewandte Physik

Teilinstitut Photophysik

Fachrichtung Physik

Fakultät Mathematik und Naturwissenschaften
der Technischen Universität Dresden

2007

1. Gutachter: Prof. Dr. Lukas Eng
2. Gutachter: Prof. Dr. Ludwig Schultz
3. Gutachter: Prof. Dr. Susan Trolie-McKinstry

Die Dissertation wurde eingereicht am 27.07.2007.

Die Dissertation wurde verteidigt am 10.12.2007.

Kurzfassung:

Oxidische Komplexverbindungen können eine Vielzahl an funktionellen Eigenschaften, wie z.B. Ferroelastizität, Ferroelektrizität, Ferro- und Antiferromagnetismus sowie kompliziertere magnetische Ordnungen, die Kombination und Interaktion solcher ferroischer Eigenschaften (Multiferroizität), hohe Spinpolarisation oder Hochtemperatursupraleitung aufweisen und gelten daher als aussichtsreiche Materialien für die zukünftige Mikroelektronik. Entscheidend für die Funktionsfähigkeit oxidischer Bauelemente sind deren elektronische Transporteigenschaften, die in äußerst sensibler Weise von der Verteilung und Dichte von ex- oder intrinsischen elektronischen Defektzuständen an Grenz- und Oberflächen innerhalb der Bauelementstruktur abhängen.

Die vorliegende Arbeit beschäftigt sich mit der Spektroskopie solcher elektronischer Eigenschaften mittels photonenbasierter Methoden. Im Fokus stehen dabei perowskitische Oxide (Oxide mit ABO_3 -Struktur), speziell das Modellperowskit Strontiumtitanat ($SrTiO_3$) als Substrat und darauf mittels gepulster Laserdeposition (PLD) abgeschiedene dünne Filme (10-15 nm Dicke) dotierter Lanthanmanganate ($La_{0.7}Sr_{0.3}MnO_3$, $La_{0.7}Ca_{0.3}MnO_3$, $La_{0.7}Ce_{0.3}MnO_3$).

Im Rahmen einer halbleiterphysikalischen Interpretation widmet sich der erste Teil der Identifikation elektronischer Ober- und Grenzflächenzustände an der $SrTiO_3$ -Oberfläche sowie an verschiedenen Lanthanmanganat/ $SrTiO_3$ -Grenzflächen mittels dreier unterschiedlicher experimenteller Methoden zur Vermessung der Oberflächenphotospannung: der Photoelektronenspektroskopie unter zusätzlicher optischer Anregung, einer kapazitiven Detektionsmethode in Plattenkondensatorgeometrie unter modulierter optischer Anregung und der optischen Kelvin-Sonde. Neben einem auf die bei oxidischen Ober- und Grenzflächen auftretenden besonderen Herausforderungen zugeschnittenen Methodenvergleich werden Grenzflächenzustände bezüglich ihrer energetischen Position in der Bandlücke des $SrTiO_3$ und ihres Relaxationsverhaltens analysiert, als substrat- oder filminduziert klassifiziert, und die Verringerung ihrer Dichte nach geeigneter Ausheilprozedur wird nachgewiesen.

Der zweite Teil der Arbeit befasst sich mit der in der Literatur bisher kontrovers diskutierten Frage, ob sich die isolierende Stammverbindung $LaMnO_3$ durch Dotierung mit tetravalenten Kationen, wie z.B. Ce^{4+} , in einen elektronendotierten Halbleiter verwandeln lässt - analog zur Herstellung lochdotierter Lanthanmanganate durch Dotierung mit divalenten Kationen, wie z.B. Sr^{2+} oder Ca^{2+} . Die Frage ist äquivalent zur Betrachtung, ob unter Beibehaltung der Stabilität des Kristallgitters ein Teil der Manganionen vom Mn^{3+} -Zustand in den Mn^{2+} -Zustand übergehen kann. Um einen Beitrag zur Klärung dieses Problems zu leisten, wurden als elektronisch sensitive Methoden die Röntgen- und UV-Photoelektronenspektroskopie (XPS/UPS) gewählt. Die oben genannten Lanthanmanganatfilme wurden dazu hinsichtlich der Austauschspaltung der Mangan-3s-Linie im XP-Spektrum, die in linearer Weise von der Manganvalenz abhängt, und der anhand der Breite des UP-Spektrums ermittelten Austrittsarbeit jeweils nach Reinigung der Oberfläche im Ultrahochvakuum (UHV) vergleichend untersucht. Die Messungen wurden nach unterschiedlich starker Desoxidation durch Heizen im UHV und Reoxidierung durch Heizen in Sauerstoffatmosphäre durchgeführt. Es konnte nachgewiesen werden, dass eine Elektronendotierung des $La_{0.7}Ce_{0.3}MnO_3$ -Films bei geeigneter Einstellung des Sauerstoffgehalts tatsächlich möglich ist. Außerdem wurde gezeigt, dass sich sowohl in di- als auch in tetravalent dotierten Lanthanmanganatfilmen die Manganvalenz und damit der Dotierungstyp reversibel durchstimmen lässt.

Abstract:

Complex oxides are an intriguing field of solid-state research, as they can exhibit a wide variety of functional properties, such as ferroelasticity, ferroelectricity, ferro- and antiferromagnetism or an even more complicated type of magnetic ordering, the combination or interaction of those ferroic properties (multiferroicity), high spin polarization, or high-temperature superconductivity. Thus they are prospective candidates for future materials in microelectronics. It is a matter of fact that the performance of such oxide-based devices depends mainly on transport properties, which in turn depend on the distribution and density of intrinsic or extrinsic electronic interface states across the device structure.

The present thesis focuses on the identification and characterization of such electronic properties by two different photoassisted spectroscopy techniques: surface photovoltage spectroscopy and photoelectron spectroscopy. This work especially deals with perovskite oxides, namely with the model perovskite strontium titanate (SrTiO_3) as a substrate and three differently doped lanthanum manganite thin films (10-15 nm thickness) grown by pulsed laser deposition (PLD) on the SrTiO_3 substrate ($\text{La}_{0.7}\text{Sr}_{0.3}\text{MnO}_3$, $\text{La}_{0.7}\text{Ca}_{0.3}\text{MnO}_3$, $\text{La}_{0.7}\text{Ce}_{0.3}\text{MnO}_3$).

The first part aims at the identification of electronic surface and interface states at the free SrTiO_3 surface as well as at the three different lanthanum manganite/ SrTiO_3 interfaces. For that purpose three different experimental realizations of the surface photovoltage spectroscopy technique were implemented and employed: photoelectron spectroscopy under additional optical excitation, the capacitive detection of the photoinduced displacement current in a parallel-plate capacitor geometry under modulated optical excitation, and the classical Kelvin probe technique. The methods are evaluated comparatively with respect to their suitability to analyze the given oxidic interfaces. The main result of this first part is a map of the energetic positions and relaxation time constants of the surface states at the SrTiO_3 surface as well as of the interface states at the lanthanum manganite/ SrTiO_3 interfaces within the SrTiO_3 bandgap. The interface states were classified into film- and substrate-induced states and it could be demonstrated that an appropriate annealing procedure can dramatically decrease their densities.

The second part tackles the problem of the manganese valence and the doping type of di- and tetravalent-ion-doped LaMnO_3 . The question whether the insulating parent compound LaMnO_3 becomes an electron-doped semiconductor after doping with tetravalent cations such as Ce^{4+} - which would be in analogy to the well-established hole doping after partial substitution of La^{3+} by divalent cations such as Sr^{2+} or Ca^{2+} - has been discussed controversially in the literature so far. Due to the physics of the manganite crystal lattice the question can also be formulated in a different way: Can part of the manganese ions be driven from the Mn^{3+} state towards the Mn^{2+} state without any crystal instabilities or phase separation phenomena? In order to contribute to the clarification of this question, an extensive X-ray- and UV-photoelectron spectroscopy (XPS/UPS) investigation was performed. The three differently doped lanthanum manganite thin films were comparatively studied considering the exchange splitting of the Mn 3s core level line, which is a linear function of the Mn valence, as measured by XPS and the work function as extracted from UPS. All measurements were performed at different states of deoxygenation after heating in ultrahigh vacuum and reoxidation after heating in a pure oxygen atmosphere. Strong evidence for electron doping of the $\text{La}_{0.7}\text{Ce}_{0.3}\text{MnO}_3$ film after deoxygenation was found. Furthermore, the reversible tunability of the Mn valence by variation of the oxygen content could be demonstrated for both tetravalent- and divalent-ion-doped lanthanum manganite films.

List of abbreviations

AFM	atomic force microscopy
BFO	BiFeO ₃
CMR	colossal magnetoresistance
FeRAM	ferroelectric random-access memory
FET	field effect transistor
GMR	giant magnetoresistance
LCAO	linear combination of atomic orbitals
LCeMO	La _{1-x} Ce _x MnO ₃ (here: x=3)
LCMO	La _{1-x} Ca _x MnO ₃ (here: x=3)
LO	longitudinal optical
LSMO	La _{1-x} Sr _x MnO ₃ (here: x=3)
LEED	low-energy electron diffraction
MIT	metal-insulator transition
MOSFET	metal-oxide-semiconductor field effect transistor
MR	magnetoresistance
MRAM	magnetic random-access memory
PC	photoconductivity/photocurrent
PL	photoluminescence
PLD	pulsed laser deposition
RAM	random-access memory
SPS	surface photovoltage spectroscopy
SPV	surface photovoltage
STM	scanning tunneling microscopy
STO	SrTiO ₃
T _C	Curie temperature
UHV	ultrahigh vacuum
UPS	ultraviolet photoelectron spectroscopy
XAS	x-ray absorption spectroscopy
XRD	x-ray diffraction
XPS	x-ray photoelectron spectroscopy

Contents

1	Introduction	9
2	Oxides - an intriguing class of materials	13
2.1	Strontium titanate (SrTiO_3)	18
2.1.1	Basic properties within the perovskite family	19
2.1.2	Doping	19
2.1.3	Surfaces	20
2.1.4	Band structure and optical response	21
2.1.5	Charge transport	23
2.2	Lanthanum manganites ($\text{La}_{1-x}\text{A}_x\text{MnO}_3$)	24
2.2.1	Review on manganite research	26
2.2.2	The parent compound LaMnO_3	27
2.2.3	Electronic and magnetic structure upon doping	29
2.2.4	Additional physics of manganites	32
2.3	Oxide samples of the present study	35
3	Surface photovoltage investigations	37
3.1	Fundamental considerations	37
3.1.1	The physics of surface photovoltage phenomena	37
3.1.1.1	Electronic structure of semiconductor surfaces	38
3.1.1.2	The surface photovoltaic effect	39
3.1.1.3	Sensitivity to buried interfaces	41
3.1.2	Electronic interface states of SrTiO_3 and ferroic systems - a literature review	42
3.1.2.1	Electronic properties of SrTiO_3 surfaces and interfaces	42
3.1.2.2	Photon-assisted spectroscopy for the investigation of ferroic interfaces	44
3.1.2.3	Interface investigations of perovskite heterostructures without optical excitation	45
3.1.2.4	Conclusions drawn from the literature results	45
3.2	Experimental approaches and results	46
3.2.1	Sample illumination	46
3.2.2	X-ray photoelectron spectroscopy under additional optical illumination (X-SPS)	48
3.2.2.1	Principle and realization	48
3.2.2.2	Results	49
3.2.3	Parallel-plate capacitor under modulated optical excitation (C-SPS)	51
3.2.3.1	Principle and realization	51
3.2.3.2	Results	52
3.2.4	The optical KELVIN probe (K-SPS)	58
3.2.4.1	Principle	58
3.2.4.2	Realization	62

3.2.4.3	Results	65
3.3	Summary and discussion	69
4	Photoelectron spectroscopy investigations	73
4.1	Fundamentals	73
4.1.1	The principle of photoelectron spectroscopy	73
4.1.1.1	The photoelectric effect and its physical information content	73
4.1.1.2	Setup	75
4.1.2	Calibration	77
4.1.3	Quantification	78
4.2	Deducing the manganese valence in hole- and electron-doped lanthanum manganite thin films	80
4.2.1	Motivation and state of the scientific discussion	80
4.2.2	Experimental approach of the present work	81
4.2.3	Results and discussion	85
4.2.3.1	XPS peak areas and stoichiometry	85
4.2.3.2	O 1s core level signal	87
4.2.3.3	Ce 3d and Ca 2p core level signals	88
4.2.3.4	La 3d core level signal	89
4.2.3.5	Mn 2p core level signal	91
4.2.3.6	Mn 3s exchange splitting	94
4.2.4	Summary and outlook	97
5	Summary and outlook of the thesis	101
	Bibliography	105
	Appendix	129
A	MATHEMATICA[®] scripts	129
A.1	Electrical field intensity at buried interfaces – calculation with the FRESNEL matrix formalism	129
A.2	Calculation of the optical constants of a weakly absorbing substrate from transmission and reflection measurements	137
B	Addenda to the surface photovoltage part	139
B.1	Collection of SPV spectra from C-SPS	139
B.2	Further theoretical treatment of the Kelvin probe current	146
B.2.1	Decomposition into harmonics	146
B.2.2	Plots of the total current and its first two harmonics	149
B.3	Signal flow diagram of the Kelvin probe SPV measurement	152
C	Own publications	153
C.1	Journal articles	153
C.2	Conference contributions	154
C.2.1	Talks	154

<i>CONTENTS</i>	3
C.2.2 Posters	154
Acknowledgments	157
Erklärung	159

List of Figures

1.1	Scope of the thesis	11
2.1	Metal-oxide-semiconductor field effect transistor	15
2.2	Perovskite structure	18
2.3	Magnetoresistance of manganites.	28
2.4	3d orbitals of the Mn ion.	30
2.5	Phase diagrams of LCMO and LSMO.	33
2.6	Phase diagram of LCeMO	33
3.1	Band alignment of a depleted semiconductor surface and SPV generation.	39
3.2	Possible SPV generation mechanisms under sub-bandgap illumination.	40
3.3	SPV spectrum of a CdS surface and derivation of the surface state distribution.	40
3.4	Possible band alignment at the manganite/SrTiO ₃ interface.	41
3.5	Illumination setup for surface photovoltage spectroscopy.	47
3.6	SPV-related O1s core level shifts in the x-ray photoemission spectra of LSMO.	50
3.7	SPV as a function of illumination intensity.	50
3.8	Setup for surface photovoltage measurements in parallel-plate capacitor geometry.	53
3.9	SPV spectra of the LSMO/STO system.	54
3.10	Comparison of the SPV spectra of LSMO/STO, LCMO/STO, and LCeMO/STO.	57
3.11	Contact potential difference between two different metals forming a capacitor.	59
3.12	Mechanical parts of the KELVIN probe.	63
3.13	Electrical circuitry for KELVIN probe SPV measurements.	64
3.14	SPV spectrum of the pure undoped SrTiO ₃ surface.	66
3.15	Surface photovoltage transients of SrTiO ₃	67
4.1	Basic setup for a photoelectron spectroscopy experiment.	75
4.2	Energy level diagram for sample and spectrometer in photoelectron spectroscopy.	77
4.3	Ultraviolet photoelectron spectrum of a clean Au(110) surface.	78
4.4	X-ray photoelectron spectrum of a clean Au(110) surface.	79
4.5	XPS survey scan of the cleaned LCeMO thin film.	83
4.6	Mn 3s core level signal and La 4d satellite signal for the LCeMO thin film.	85
4.7	O 1s core level signals for LCMO and LCeMO.	88
4.8	Ce 3d signals of the LCeMO surface.	89
4.9	Work function changes of LCMO and LCeMO after deoxygenation	90
4.10	La 3d signal of the cleaned LCMO surface.	91
4.11	Development of the La 3d _{5/2} binding energy after the different heating steps.	92
4.12	Mn 2p doublet of the LCeMO film.	93

4.13	Mn 3s signals of the LCeMO film	95
4.14	Mn valences of the LCMO and LCeMO film.	96
4.15	Plot of the Mn 3s exchange splitting energy versus the formal Mn valence	97
4.16	Photoconductivity of an oxygen-deficient LCeMO film.	98
A.1	Notation for optical calculations of a layered system	130
A.2	Photon flux at the LSMO/STO interface	136
A.3	Optical transmission and reflectivity of a SrTiO ₃ substrate.	137
B.1	Reproducibility of a C-SPS measurement on LCeMO/STO.	140
B.2	SPV spectrum of the LCeMO/STO system.	141
B.3	SPV spectra of the LCeMO/STO system, as-prepared and annealed.	142
B.4	SPV spectrum of the LCMO/STO system.	143
B.5	SPV spectra of the LCMO/STO system, as-prepared and annealed.	144
B.6	Energetic positions of trap states in different manganite/STO systems.	145
B.7	KELVIN probe current for $d_1/d_0 = 0.25$	150
B.8	KELVIN probe current for $d_1/d_0 = 0.8$	150
B.9	KELVIN probe current for $d_1/d_0 = 0.05$	151

List of Tables

3.1	Interface trap levels of the manganite/STO interfaces as extracted from the SPV spectra acquired with the capacitive method.	55
3.2	Trap levels of a SrTiO ₃ sample, as extracted from the SPV spectra acquired with the KELVIN probe.	66
4.1	Description of the seven different surface treatment steps applied to the LCMO and LCeMO thin films.	85
4.2	Chemical compositions of the LCMO and LCeMO films after different treatment steps.	87
A.1	Sources of the optical constants for the air/manganite/STO/Ag system. . .	131

1 Introduction

This introductory chapter explains the scope and the historical background of the present thesis. The more specific scientific introductions to both the materials and methods that were under investigation within the thesis will be given throughout the subsequent chapters 2, 3, and 4.

First of all, let me comment on the overall frame into which my work was integrated. When I joined the group of Prof. Lukas Eng at the Institute of Applied Photophysics in October 2003, the financial support of the *Research Group 520: Ferroic functional elements - physical principles and concepts*¹, which can be described as an interdisciplinary compound of interlinked projects, had just recently been approved by the German Research Foundation for a period of three years. In this first period the *Research Group* covered eight different projects with contributions from the departments of physics, chemistry, and engineering at Dresden University of Technology, as well as from the Leibniz Institute for Solid State and Materials Research (IFW). It would be beyond the scope of this introductory chapter to comment on the whole topical frame of all those projects. Thus I focus only on the project that finally became *my* project and which had the working title: *Identification of electronic defect states at inner interfaces of perovskite heterostructures*. What was behind this title?

Concerning materials, this project was focused the interface between lanthanum strontium manganite ($\text{La}_{1-x}\text{Sr}_x\text{MnO}_3$) films² and strontium titanate (SrTiO_3) substrates. Why the $\text{La}_{1-x}\text{Sr}_x\text{MnO}_3$ system and, more generally, doped lanthanum manganites of the structure $\text{La}_{1-x}\text{A}_x\text{MnO}_3$, with A being a nontrivalent metal cation, on the one hand and strontium titanate on the other hand are worth being investigated, what intriguing physical properties those two systems show, and how puzzling their properties are — all those points will be explained in chapter 2. Before those two quite different types of complex oxides are illuminated in detail, a short general discussion of the fast-growing field of oxide research, especially oxide electronics, and the motivation behind it will open chapter 2.

Concerning experimental methods, the focus of the project was intended to be the

¹<http://www.for520.de>

²The films were fabricated at the IFW Dresden. Further comments on film preparation, which, however, is not in the focus of this thesis, will be given in chapters 3 and 4.

utilization of surface photovoltage (SPV) phenomena as a probe for the analysis of the electronic properties of the buried manganite/strontium titanate interface. Here, it must be stressed that the main challenge of this project is the fact that a nonstandard experimental method³, which only in a few cases is straightforward in the interpretation of the experimental data⁴, is applied to a nontrivial object, namely the manganite/strontium titanate interface. This statement is intensified when we realize that, on the one hand, SPV phenomena are commonly explained in terms of classical semiconductor physics, but on the other hand materials with correlated electrons, such as lanthanum manganites, cannot be fully described in those terms. The heretical reader could ask now why this experimental method is chosen at all? The first answer is that there are almost no alternatives, because standard interface-state-sensitive analysis methods from semiconductor physics, such as deep-level transient spectroscopy (DLTS), fail for wide-gap semiconductors such as SrTiO₃. Thus optical methods, e.g. surface photovoltage methods, are the only alternatives. For a second answer let me cite M. COEY, author of one of the most comprehensive review articles [Coe99] on manganites [Coe04]:

The stock response that everything is more complicated than we first thought is never much help. [...] simple ideas have the power to guide us even when they are only half-truths.

After all, it could be shown within the present thesis that we can indeed gain information on the interface of interest and that the chosen experimental approach is – within distinct borders – a promising tool for *characterizing and evaluating* oxidic interfaces with respect to the distribution of their electronic states. How this can be achieved will be illustrated in chapter 3, which starts with a short introduction into the physics of surface photovoltage phenomena and their application in surface and interface analysis. Subsequently, the manganite/strontium titanate interface will be described within the paradigm of semiconductor physics and a literature review on related approaches will be given. The main part of chapter 3 will be dedicated to the several experimental realizations of spectral and time-resolved SPV measurements that were developed and applied within this work, the

³Of course, this classification is subjective but supported by the experience that the *common solid-state physicist* has a certain imagination on what standard methods such as photoelectron spectroscopy or electron diffraction are about, but not what surface photovoltage exactly means. On the other hand, it has to be noted that SPV techniques are being applied industrially — but exclusively for the analysis of *classical* semiconductors, especially silicon.

⁴In their extensive review article on *Surface photovoltage phenomena: theory, experiment, and applications* [Kro99] KRONIK and SHAPIRA write: *The sensitivity of SPV measurements to a plethora of physical phenomena is a double-edged sword because it requires very careful experiment design and data interpretation for the (qualitative or quantitative) extraction of specific properties.*

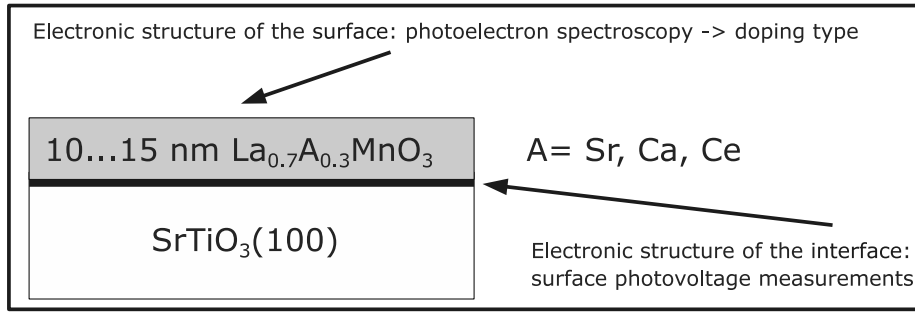


Figure 1.1: Scope of the thesis. The work focuses on thin films of differently doped lanthanum manganites on strontium titanate substrates. The *surface* electronic properties of the films, esp. the manganese valence as an indicator of the doping type, of the films were studied by photoelectron spectroscopy. The *interface* electronic properties, esp. the energetic distribution of trap states within the band gap of the strontium titanate substrate, were studied by surface photovoltage spectroscopy.

results of those measurements, and their interpretation.

The thesis covers also a second branch of research, which focuses on lanthanum manganites as well, especially on the surfaces of $\text{La}_{0.7}\text{Ca}_{0.3}\text{MnO}_3$ (LCMO) and $\text{La}_{0.7}\text{Ce}_{0.3}\text{MnO}_3$ (LCeMO) thin films. In that part, which will be described in chapter 4, a comparative x-ray and ultraviolet photoelectron spectroscopy investigation was performed on the two differently doped lanthanum manganite films named above. The study must be seen as a contribution to the ongoing scientific debate (which is itself reviewed within chapter 4) on whether electron doping of LaMnO_3 by substitution of part of the trivalent lanthanum ions by tetravalent cations, such as Ce^{4+} , is possible or not and which analysis method gives reliable information on the doping type of a given sample. The whole study was originally not scheduled - it is an example of how the interaction of different groups within a project network such as the *Research Group 520* can spread fruitful ideas for scientifically interesting explorations.

Figure 1.1 summarizes the scope of this thesis in a compact way.

It is a well-known phenomenon that, the deeper one dives into a field of research, the more unsolved questions come to one's mind. Thus much work remains to be carried out, and a summary of both reached goals and open problems will be given in chapter 5.

2 Oxides - an intriguing class of materials

The purpose of this chapter is to give an introduction into a fast-growing and fascinating field of condensed-matter physics and materials science - the field of complex oxides¹. It is explained why those materials are worth being investigated from the viewpoints of both fundamental physics and applications in microelectronics. After some general considerations, which clearly cannot be complete due to the immense diversity of the field, two subsections are dedicated to the two members of the perovskite oxide family that were investigated within the present work: strontium titanate and lanthanum manganites. Their importance as model systems and their basic physical properties are reviewed. The last subsection describes the concrete samples that were studied within the thesis.

Oxidic compounds exhibit a wide variety of so-called *functional* properties, such as ferroic² behavior and high-temperature superconductivity³. This variety is even broadened by the fast-developing field of thin-film technology, which provides high-quality oxidic thin films, tailor-made multilayer structures, as well as superlattices [Oht02]. Oxides crystallize in a wide range of structures. Among those structures are

- the outstanding *perovskite* structure (see figure 2.2), as found in BaTiO_3 , which itself is one of the most-investigated ferroelectric crystals,
- *perovskite-related* structures as in $\text{YBa}_2\text{Cu}_3\text{O}_7$, the prototype of a high-temperature superconducting oxide,
- the *rutile* structure (CrO_2 , TiO_2),

¹The term *complex oxide* is widely used in materials science, but to find a clear definition is not easy. It might stem from inorganic chemistry, where a *complex compound* is a compound with a central atom, in most cases a metal atom with a nonclosed outer electron shell, being surrounded (*coordinated*) by a certain number of anions (oxygen in our case). Another definition is given by the simple statement that a *simple oxide* has the formula $A_m\text{O}_x$, while a *complex oxide* contains more than one cation according to $A_mB_n\dots\text{O}_x$. However, concerning the physics of oxidic crystals, the term *complex* has also been used in the sense of *complicated* and *polymorphic* [Nog04, Dag05, Mor06] — and this may apply also to a simple oxide.

²The term *ferroic* is a generic term for the terms ferro-, ferri-, and antiferromagnetic, ferro- and antiferroelastic, ferro- and antiferroelectric, and their simultaneous occurrence. For clear definitions, see e.g. [Eer06].

³For an overview see for example [Ore00], the pioneering work can be found in [Bed86].

- the *spinel* structure, as in Fe_3O_4 , the prototype of a charge-ordered oxide ⁴,
- or even more complex structures, such as modulated intergrowth structures as discussed in [Dav99].

This diversity of crystallographic structures, the tendency of oxygen ions to form tetra- or octahedra with the d electrons of the metal ions, the possibility to vary the oxygen stoichiometry, as well as the possibility of doping are reflected by complex electronic properties [Man05]. In the easiest case, oxides are band insulators⁵ with an energy gap of several electron volts. The much more complicated physics is shown by those oxides that have correlated electron systems, in most cases transition metal oxides and rare-earth oxides. Those compounds can show a complicated interplay between different degrees of freedom. In other words, lattice, spin, orbital [Tok00], or charge order may be sensitively interconnected, leading to extremely rich phase diagrams, with the possibility that several phases coexist in a chemically homogeneous specimen [Dag01, Mil05].

The above facts should make clear that the study of oxide physics was initially motivated by the desire to understand very fundamental phenomena of condensed-matter physics, such as phase transitions. Another strong motivation has its origin in the limits of today's silicon-based semiconductor technology. To insure the continuous downscaling of the metal-oxide-semiconductor field effect transistor (MOSFET), the workhorse in microelectronics (explained in figure 2.1), the Si-SiO₂-poly-Si triad has to be replaced by an alternative Si-dielectric-metal system. The drawback of silicon dioxide (SiO₂) is its low dielectric constant $k = 3.9$. This means that, to maintain a sufficient field effect while reducing the gate voltage⁶, one has to shrink the thickness of the SiO₂ layer. At thicknesses around 1 nm, which have been reached now, tunneling becomes a severe problem. Consequently, a dielectric with a higher dielectric constant is needed. Such a material provides the same field effect at a greater thickness in comparison to SiO₂. The research on so-called *high- k dielectrics* has attracted the attention of semiconductor physicists for

⁴*Charge ordering* means the long-range ordering of two different transition metal charge states (oxidation states) [Att06]. An experimental visualization is given e.g. in [Mor98] or [Ren02]. However, there are also serious doubts about the validity of the purely ionic picture, which commonly is used to explain the charge ordering [Coe04].

⁵The term *band insulator* appears when we consider a solid in BLOCH's picture of independent electrons. There, a solid with completely filled bands is an insulator and a solid with one partially filled band is a metal. However, this picture fails as soon as there are strong correlations between the electrons, in the simplest case by COULOMB interactions. Then a solid expected to be metallic in the independent-electron picture might be insulating, a so-called MOTT insulator. This case can be described e.g. within HUBBARD models of different stages of sophistication [Sac03, Hag05].

⁶In view of an increasing integration density, the gate voltage of one single FET should be as low as possible to prevent serious overheating problems.

many years, since a sufficiently high k value is not the only requirement the alternative gate dielectric has to fulfill. Furthermore the material of choice must (i) show a low density of electrically active defects at the interface to silicon, (ii) have a band gap of at least 4-5 eV to minimize leakage currents, (iii) be thermally stable up to 1200 K, and (iv) show sizable band offsets at the heterojunction to silicon⁷. For the time being, hafnium-based oxides seem to be the candidates of choice and are at the threshold to being applied industrially.

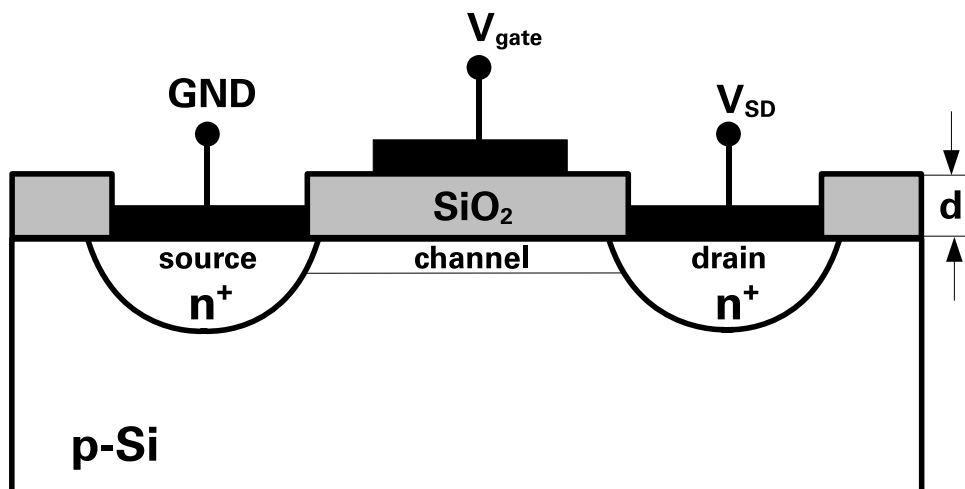


Figure 2.1: Metal-oxide-semiconductor field effect transistor (MOSFET). The figure shows a two-dimensional sketch of an n-channel MOSFET. In this case, p-type silicon serves as the substrate, which contains two highly n-doped regions: source and drain. Both regions are separated from each other. The region in-between source and drain is covered by the gate oxide (SiO_2) of thickness d , which itself is covered by a poly-silicon gate electrode. When no voltage V_{gate} is applied to the gate, the source-to-drain electrodes correspond to two $p-n$ junctions connected back to back. The only current that can flow from source to drain is the reverse leakage current. When a sufficiently large positive voltage is applied to the gate, an inversion layer (also called *channel*) is formed between the two n^+ regions. This means that a large current can flow between source and drain. The conductance of the channel can be modulated by variation of V_{gate} . Further details, such as the function of a substrate contact or different nonequilibrium regimes, are omitted here. They are comprehensively discussed for instance in [Sze81]. How the overall FET principle, namely the modulation of a certain quantity via an electrical field, might be adopted within all-oxide structures is explained in the text.

As one can guess from the previous text, there are more functional properties of oxides besides the dielectric ones. A number of those striking phenomena are listed and shortly explained below:

- Let us continue with another example which has already reached its readiness for marketing: ferroelectric oxides as part of nonvolatile random-access memories. A

⁷A clear and systematic theoretical treatment of the band alignment problem at the high-k-dielectric/silicon interface, exemplarily calculated for the SrTiO_3/Si case, is for example presented in [Zha03].

ferroelectric material exhibits a stable and switchable electrical polarization resulting from cooperative atomic displacements. This functional property is used within so-called FeRAMs (ferroelectric random-access memories) in the way that a ferroelectric layer (typically $\text{PbZr}_{0.3}\text{Ti}_{0.7}\text{O}_3$ (PZT) or $\text{SrBi}_2\text{Ta}_2\text{O}_9$) is polarized via a gate electrode [Auc98]. This polarization process is equivalent to the writing of one bit. The functionality is the same as in conventional flash RAMs, but shorter writing cycles are possible: some tens of nanoseconds compared to a few microseconds. Up to now, the lower achievable integration density has been a drawback of FeRAMs, but the implementation of a scanning-probe-based approach for reading/writing might overcome certain limitations [Par06].

- Another type of long-range order in a solid than the above-mentioned order of electric dipoles is the order of magnetic moments. Such a ferromagnetic or otherwise magnetically ordered material is characterized by a stable and switchable magnetization, which can be explained by the quantum mechanical phenomenon of exchange. Oxides, esp. the transition metal or rare-earth oxides, can show extraordinary magnetic properties. Closely linked to ferro-, ferri-, or antiferromagnetic order, also *spin polarization*⁸, which means that the charge carriers have the same spin direction, is observed. At least at low temperatures the degree of spin-polarization can be nearly 100 %, e.g. in $\text{La}_{0.7}\text{Sr}_{0.3}\text{MnO}_3$ and CrO_2 . Unfortunately, the degree of spin polarization decreases dramatically with increasing temperature. However, there are exceptions, such as the already mentioned Fe_3O_4 , which shows a spin polarization of -80% at room temperature. Consequently this material is potentially attractive as a source of or a detector for spin-polarized electrons. Other key words that must be mentioned in the context of magnetic properties of oxides are the *colossal magnetoresistance effect (CMR)* in certain rare-earth manganites and *dilute magnetic semiconductors* such as Co-doped TiO_2 or Mn- or Co-doped ZnO . Some comments on the CMR effect will be given in the section 2.2 on doped lanthanum manganites. Dilute magnetic semiconductors, which combine semiconducting properties with potentially high spin polarization, are candidates for magnetic tunnel contacts in nonvolatile magnetic random-access memories (MRAMs); for a short review see [Pea04].
- After the discussion of ferroelectric and ferromagnetic (or other magnetic) phenomena in oxides, it is straightforward to shed light on *multiferroicity*, one of the

⁸The spin of the electron is the key quantity that is utilized as the information-carrying unit in the field of *spintronics*. Possible device concepts of spintronics can be found e.g. in [Pea05].

upstarts among materials science topics during recent years. A multiferroic material exhibits both ferroelectricity and ferromagnetism within the same phase. For several reasons (among them symmetry considerations), there are only very few single-phase materials that show this property [Hil00]. One of the most widely investigated multiferroic oxides is BiFeO_3 (BFO), which is ferroelectric and anti-ferromagnetic at room temperature. In general, it has been suggested that both magnetization and electrical polarization could independently encode information in a single multiferroic bit. In practice, however, it is more likely that the two order parameters are not independent but coupled, which would be also attractive in that, in an appropriate device, data could be written electrically and read magnetically. This concept would combine the best aspects of the FeRAM concept and magnetic data storage. From the term *coupling of order parameters* it is not far to the term *magnetoelectric coupling*, which is often cited in one breath with multiferroicity or even mixed up with it. However, magnetoelectric coupling is a more widespread phenomenon and describes the influence of a magnetic (electric) field on the polarization (magnetization) of a material. There are several review articles dealing with multiferroicity and magnetoelectric coupling; two of the most recent ones are the articles by EERENSTEIN et al. [Eer06], who try to explain the *tortuous taxonomy* of the field in a clear manner and discuss the most promising single-phase oxides or oxide heterostructures showing those phenomena, and by RAMESH and SPALDIN [Ram07], who focus especially on thin-film multiferroics, where the epitaxial strain provides an additional degree of freedom to tune the film properties.

- There are several other facts that should be mentioned in an introductory chapter on oxides, without however being directly related to this thesis. Among them are the cuprates as high- T_C superconductors, self-cleaning TiO_2 surfaces, ZnO as a material for blue light-emitting diodes, or the application of oxides as catalysts for a wide variety of chemical reactions.

Before we finish this general introduction into oxides and oxide electronics, we come back to the concept of the electric field effect transistor once more. As said before, the classical semiconductor FET is based on the principle that the conductivity of a semiconductor channel is tuned by a gate voltage via the field effect. This principle can be universalized, since it is conceivable to modulate or switch also a property different from the conductivity, such as a certain phase transition in an oxide channel, via the field effect [Ahn03]. Such FETs could be *all-oxide* structures, devices made of epitaxial heterostructures of oxides beyond any silicon-based technology. The family of perovskite

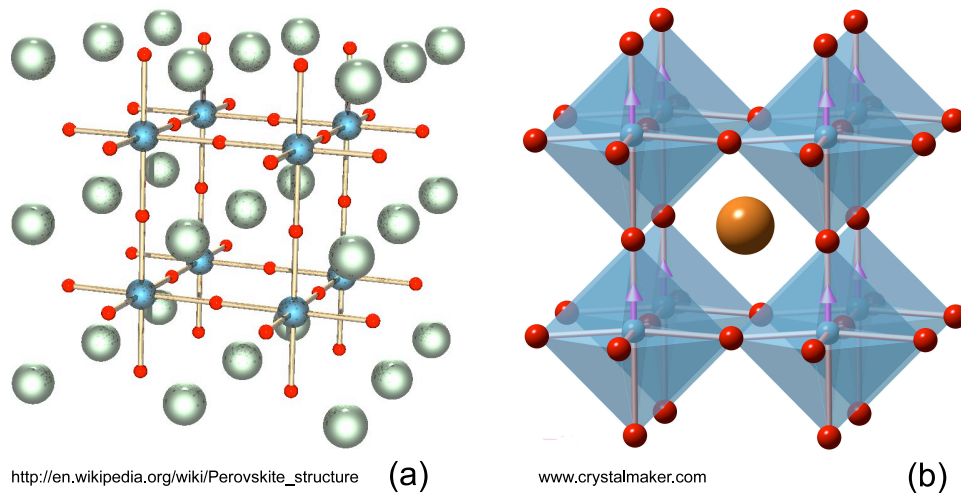


Figure 2.2: Perovskite structure. Originally, the name *perovskite* was exclusively used for the compound CaTiO₃. Later on, the term *perovskite* became common for a whole class of crystals of the general chemical formula ABO₃ (A, B are metal cations, O stands for an anion, in most cases oxygen), which all show the same general crystallographic structure. There are several approaches to explain this structure: As shown in (a), one can imagine a cube with the larger A ion in the center, the smaller B ions at the corners, and the anions (the smallest of all three ions) in the centers of the edges. Consequently, the B ion is sixfold coordinated and the A ion twelvefold. Alternatively, as shown in (b), the oxygen ions can be considered to form octahedra with the B ions in the center (BO₆ octahedra). Eight of those octahedra include one A ion in their center. Depending on the ratio of the ionic radii of the two cations, the structure might be distorted. The undistorted perovskite structure is found in SrTiO₃. However, the distortions are in many cases the very origin of functional properties, e.g. the cooperative displacement of the B ions, as indicated by the arrows in figure (b) for BaTiO₃, leads to ferroelectricity. For a readable review on the basics, the history, and the versatility of perovskite structures see for example [Bha00].

oxides (figure 2.2) is most promising as the material class of choice for those all-oxide devices, since its diverse members show only small structural differences and are therefore capable of being grown on each other with sharp atomic interfaces⁹. Here we close the cycle and continue with a more detailed view on two quite different but outstanding members of the perovskite family and, later in chapter 3, with the experimental inspection of their interface.

2.1 Strontium titanate (SrTiO₃)

Strontium titanate has been the subject of a vast amount of experimental and theoretical studies with currently around three hundred publications per year. Some of the most important properties concerning crystal structure, surfaces, band structure, as well as

⁹As to the structure and transport along and across perovskite *interfaces*, further remarkable phenomena have been predicted theoretically and observed experimentally, for example, the occurrence of a two-dimensional electron gas (2DEG) at the interface between two insulating perovskites [Oht04, Oka04].

optical, transport and electronic properties are summarized in the following text. We consider exclusively single crystals and omit thin films, ceramics, bicrystals, or nanostructures.

There are mainly two reasons for the immense interest in SrTiO₃. First, as already mentioned, it is *the* model perovskite with undistorted cubic symmetry at room temperature. At the same time, the properties of SrTiO₃ may show dramatic changes depending on several parameters, such as oxygen stoichiometry, doping, annealing procedures, mechanical stress, or external electric fields. Thus, it is the perfect subject for fundamental studies. Second, SrTiO₃ is a widely used substrate for thin-film epitaxy of many other perovskites. It is completely clear that the first prerequisite for the understanding of such heterostructures is the understanding of each single component, including the substrate.

2.1.1 Basic properties within the perovskite family

Stoichiometric SrTiO₃ single crystals¹⁰ are transparent, paramagnetic across the whole temperature range, dielectric with a dielectric constant $\epsilon = 310$, and insulating with a band gap of approximately 3.2 eV at room temperature. They show a cubic perovskite structure with a lattice parameter $a = 3.905$ Å. The space group is $Pm\bar{3}m$. At 105 K SrTiO₃ undergoes a cubic-to-tetragonal phase transition, which is also referred to as antiferrodistortive (AFD) phase transition. Concerning ferroelectricity, different statements can be found in the literature. There is a general agreement that SrTiO₃ is paraelectric at room temperature. While WEAVER [Wea59] observed that SrTiO₃ shows ferroelectric hysteresis below 45 K, MÜLLER and coworkers [Mül79] claim SrTiO₃ to be a quantum paraelectric that never becomes ferroelectric. In summary, it is the message of the majority of publications that the phase transitions and almost all other physical properties are strongly influenced by the real structure of a given sample.

2.1.2 Doping

Another route to changing the properties, first of all the conductivity, of the ideal stoichiometric SrTiO₃ crystal is doping, for example with Nb, Fe, La, Y, In, Sc, or by oxygen vacancies after reduction by heating in a hydrogen atmosphere or in ultrahigh vacuum. The most common doping ion is Nb⁵⁺ which occupies part of the Ti sites, resulting in n doping. Also La³⁺, Fe³⁺, Y³⁺ on the Sr site and oxygen vacancies lead to n -type SrTiO₃.

¹⁰Commercially available single crystals are typically grown by the VERNEUIL flame fusion process [Bed77], for references on alternative methods see e.g. [Nas88, Nab03].

Codoping with iron and molybdenum leads to *photochromism*: In equilibrium the doping ions are in their Fe^{3+} and Mo^{6+} states, and the crystal is transparent. Upon illumination at a wavelength of 430 nm a charge transfer between the two different dopants takes place, leading to a $\text{Fe}^{4+}/\text{Mo}^{5+}$ state, which is accompanied by a coloring of the crystal. Erasure of this state happens by diffusion over time and can be accelerated by illumination with red light [Wil71]. The effect is also observed with the nickel/molybdenum system and under single nickel, iron, and cobalt doping [Fau71]. It was proposed as a possible basis for new *oxide memory concepts* in the 1970s [Sta75] but later disappeared from research interest.

In^{3+} or Sc^{3+} on the Ti site provoke *p* doping, which seems to have been less investigated so far. An all-oxide *pn* junction based on Nb- and In-doped SrTiO_3 was reported recently [Zho05]. Furthermore it is noteworthy that doped SrTiO_3 becomes superconductive below 0.3 K [Sch64, Amb66].

Within the field of diluted magnetic semiconductors, it has been shown that doping of SrTiO_3 with Co or Mn ions by ion implantation leads to ferromagnetism at room temperature [Lee03].

2.1.3 Surfaces

Let us continue our survey with an as important as difficult topic — the physics of the SrTiO_3 surface. Concerning experimental studies of the SrTiO_3 surface, the most serious problem lies in the fact that pure strontium titanate is insulating. Thus, the most powerful analysis methods in surface science, such as scanning tunneling microscopy (STM), low-energy electron diffraction (LEED), or ultraviolet and x-ray photoelectron spectroscopy (UPS/XPS), which urgently need a sufficient conductivity of the specimen under investigation, fail. As a consequence, most surface investigations have been performed on doped SrTiO_3 , which, according to our previous statement, is a quite different material. Nevertheless, concerning the surface structure, i.e., possible surface reconstructions, much work has been done on the $\text{SrTiO}_3(100)$ surface, which has been shown to be more stable and easier to prepare than the (110) and (111) surfaces [Zeg82]. A comparative combined LEED/STM study of all three surface orientations was presented by ZEGENHAGEN et al. [Zeg82], who showed that the $c(6 \times 2)$ reconstruction of the (100) surface, which had been prepared by annealing in pure oxygen, is stable in air. Other reconstructions, namely (2×1) , (2×2) , and $c(\sqrt{5} \times \sqrt{5})$ were found to be unstable due to their oxygen deficiency. Another extensive STM/LEED investigation of the (100) surface is that by CASTELL [Cas02a] on Nb-doped SrTiO_3 , where additionally $c(4 \times 2)$ and $c(4 \times 4)$ reconstructions

are presented, structure models are proposed, and an overview on previous literature on surface reconstructions is given. Another reconstruction, $c(\sqrt{13} \times \sqrt{13})$ was found by KUBO et al. within a combined STM/first-principles study. In the theory branch, there are several first-principles studies showing that the surface structure is a sensitive function of oxygen partial pressure and temperature [Joh04] and that the TiO₂-terminated surface behaves very differently from the SrO-terminated one [Li98, Hei02]. The TiO₂ termination is considered to be stable and the recipe by KAWASAKI et al. [Kaw94] how to prepare TiO₂-terminated SrTiO₃ samples by etching in NH₄F-buffered hydrofluoric acid solution with a pH value between 4.4 and 4.6 has become very popular. Other publications report on the formation of islands with electronic properties different from those of the bulk [Lia94] or nanostructures [Szo00, Cas02b] after certain treatments, which again shows the diversity of the field.

The same tendency, namely that general statements are not possible, becomes obvious when we look at the variety of investigations on the electronic surface properties, which are, of course, inherently interlinked with the atomic structure. There are indications for the existence of shallow as well as midgap surface states [Wol73, Pow76, Hen78, Hei02], depending on the history of sample treatment in experimental studies or on the model assumed in theoretical works.

The statement that the most common surface analysis techniques need conductive surfaces is not true for one powerful technique: atomic force microscopy (AFM), which *is* able to image also undoped SrTiO₃ surfaces. An elaborate AFM investigation of reduced, oxidized, *and* also original stoichiometric (as-grown) SrTiO₃ surfaces was published by SZOT and SPEIER [Szo99]. The authors presented both an excellent introduction to the diverse and often contradictory findings within SrTiO₃ surface physics and a systematic study of the surface structure after many different treatment procedures.

2.1.4 Band structure and optical response

Shortly after the establishment of the flame fusion growth method of SrTiO₃, first optical investigations showed that the optical band gap of the new material is 3.2 eV and that no birefringence occurs at room temperature [Nol54, Lev55]. First values of the refractive index were published and SrTiO₃ was proposed as a material for optical windows, prisms, or lenses. The strong dependence of the optical constants on doping were shown by GANDY [Gan59] and later by several other groups, e.g. [Bae66, Zol00, Fry03]¹¹.

¹¹For optical data of only n-doped SrTiO₃ see [Lee75, Cra99].

The probably first theoretical band structure calculation was performed by KAHN and LEYENDECKER, who used the method of linear combination of atomic orbitals (LCAO) and adjusted the ionic charges to match the previously measured band gap, which was treated as a direct band gap. They showed that the uppermost valence band has oxygen $2p$ character and the lowest conduction band has titanium $3d$ character [Kah64]. This work was followed by a fundamental and frequently cited UV reflectance study by CARDONA [Car65], which partially reproduced the theoretical findings and provided data of the complex dielectric function in a wide wavelength range. Later, a complementary study using the same technique was published by BÄUERLE [Bäu78]. Other band structure investigations are those by REIHL [Rei84] and HIGUCHI [Hig00] by x-ray absorption spectroscopy, which were, however, performed on doped SrTiO_3 . In the meantime, further band structure calculations applying a different model have been carried out for undoped [Sou72, Mat72, Sah00] and n -doped SrTiO_3 [Sha98, Guo03]. There, it was stressed that Nb-doped SrTiO_3 ($\text{SrTi}_{1-x}\text{Nb}_x\text{O}_3$) and oxygen-vacancy-doped (reduced) SrTiO_3 ($\text{SrTiO}_{3-\delta}$) cannot be described within a rigid band model. On the contrary, La-doped SrTiO_3 ($\text{Sr}_{1-x}\text{La}_x\text{TiO}_3$) fits into such a band model. The explanation for this peculiarity is that the electronic properties of the titanates are mainly dictated by the electrons of the TiO_6 octahedra, which are strongly influenced by oxygen vacancies and dopants on the Ti site.

The question whether the band gap of SrTiO_3 is of direct or indirect nature turned out to be a challenge. COHEN found from comparative absorption, reflectivity, and electroreflectance measurements around the fundamental absorption edge that the absorption coefficient as a function of the incident photon energy shows an exponential behavior (URBACH behavior) and can consequently not be fitted by a power law [Coh68]. Thus he was not able to decide on the nature of this fundamental transition. Furthermore he claimed that there were no excitons due to the large dielectric constant, which results in a very small binding energy of WANNIER excitons, and he also excluded the existence of a FRANZ-KELDYSH effect. However, after an investigation of the *fine structure* of the absorption edge of several samples with different degrees of purity, CAPIZZI et al. found the band gap to be an indirect one at 3.27 eV, which is followed by the first direct transition at 3.46 eV [Cap70]. The indirect transition goes from Γ_{15} to X_3 , mediated by a LO phonon with an energy of 51 meV, whereas the direct transition takes place at the X point of the BRILLOUIN zone. The indirect nature of the band gap was later confirmed by several groups [Red72, Yac73, Wea74]. The latter two used the alternative techniques of electroabsorption and wavelength modulation spectroscopy to improve the resolution of the fine-structure data. Surveys of the history of the understanding of the optical

properties of SrTiO₃ can be found e.g. in [Wea75], where another unusual fact, namely the relative temperature independence of the band gap, is discussed, or in [Gol87].

A similar puzzling situation shows up if we focus on the photoluminescence (PL) of SrTiO₃. In his extensive PL and photoconductivity (PC) study SIHVONEN [Sih67] reports on a broad *green* luminescence band with a peak at 500 nm and several bands in the infrared region. Concerning photoconductivity, long-term relaxation behavior is found. Recombination is proposed to happen via multiple defects. Both phenomena, PL and PC were observed to be sensitive to the cubic-tetragonal phase transition at 105 K and the para-to-ferroelectric transition at 45 K. Up to now, divergent explanations for the green luminescence have appeared in the literature. While LEONELLI et al. [Leo86] explain it as an intrinsic effect due to self-trapped excitons resulting from strong lattice relaxation, MOCHIZUKI et al. [Moc05] question the intrinsic nature of this process on the basis of their observation that the green PL disappears when the sample is treated by a continuous oxygen flow. Thus, they argue that the effect must be extrinsic, namely due to oxygen defects. Recently, an additional blue luminescence band was observed and discussed by several groups, which is without doubt of extrinsic nature (different kinds of doping) [Kan05, Moc05, Kan06]. Coming back to photoconductivity once more, we note that recent findings do not confirm the strong sensitivity of the photocurrent to phase transitions [Ros07].

2.1.5 Charge transport

Since undoped high-quality SrTiO₃ single crystals exhibit high specific resistances greater than 10⁷ Ωm at room temperature [Mit81]¹², it is not surprising that the majority of transport investigations have been performed on doped crystals.

From a combined HALL, SEEBECK, and conductivity investigation on reduced and doped SrTiO₃ crystals FREDERIKSE and coworkers derived an effective electron mass $m^* = 16m_e$ at 300 K [Fre64], which was in good agreement with the first band structure calculations [Kah64]. Later on, the explanation of the temperature dependences of the HALL mobility and the conductivity by possible scattering mechanisms turned out to be not fully straightforward. Within a common picture of classical semiconductor physics, the low-temperature carrier mobility is limited by scattering at ionized impurities, whereas the high-temperature mobility is governed by phonon scattering. From HALL mobility measurements it was concluded that for SrTiO₃ this prediction is not completely fulfilled, since the temperature dependence of the mobility does not fit theoretical curves, neither

¹²Depending on the actual defect concentration of the crystal under investigation, much higher resistivities have been reported, for example 10¹¹ Ωm in an early conductivity study by LINZ [Lin53].

for Nb-doped nor for oxygen-vacancy-doped SrTiO₃ [Tuf67].

An even more complicated situation exists for highly resistive undoped SrTiO₃, which was examined by transient-charge measurements [Ker84]¹³. In this study, the carriers were assumed to be holes and it was shown that the transport mechanism changes from band-type transport, controlled by longitudinal-optical (LO) phonon or impurity scattering, at high temperatures to a hopping mechanism (small-polaron transport) at low temperatures with a transition temperature of 180 K. In a subsequent work [Kho88] the picture was refined by preparing only weakly reduced SrTiO₃ samples and demonstrating that the low-temperature transport mechanism changes from small-polaron transport to impurity scattering with increasing reduction level and thus rising carrier concentration.

The FERMI level position of undoped SrTiO₃ crystals was estimated by DEDYK et al. [Ded93] from conductivity measurements and the mobility data of [Ker84]. At room temperature, the authors find the FERMI level be located at 0.71 eV above the valence band edge. In the same paper also the electron affinity is given: $\chi = 3.2$ eV.

On the basis of those statements we consider the undoped SrTiO₃ substrates that were under investigation within the present thesis to be p-type wide-bandgap semiconductors with a work function of 5.7 eV.¹⁴

Here we close our brief survey on strontium titanate and continue with some facts on lanthanum manganites.

2.2 Lanthanum manganites (La_{1-x}A_xMnO₃)

In the run-up of writing some introductory sections on a certain class of materials, as needed in a thesis such as the present one, one naturally starts with an extensive study of the literature. After finishing this phase, we can draw the following conclusions:

- Going through *all the* literature is quite hopeless, since the number of publications on manganites¹⁵ exceeds eight hundred per year.

¹³Here [Ker84], the authors give a value of $p = 3 \times 10^{10} \text{cm}^{-3}$ for the carrier concentration of an undoped crystal. For comparison, n-doped crystals typically show carrier concentrations $n > 10^{18} \text{cm}^{-3}$.

¹⁴This value follows directly from the above-given positions of the FERMI level and the electron affinity, in so far as the electron affinity is defined as the difference in energy of a free electron (represented by the so-called vacuum level in an energy level diagram) and the bottom of the conduction band on the one hand and the work function as the difference between the vacuum level and the FERMI level on the other hand.

¹⁵The term *manganites* refers to manganese oxides of the general formula R_{1-x}A_xMnO₃ (R= La, Y, Bi or a rare-earth metal; A= nontrivalent doping element). Depending on the special context, one also finds the terms *rare-earth manganites*, *CMR manganites*, or *mixed-valence manganites*.

- On the other hand, there are a couple of review articles on manganites which finally served as the basis for the following text [Ram97, Coe99, Sal01, Edw02, HG03, Gor04, Dör06]. Consequently, individual original articles are cited only in a few cases, for further references we refer to the voluminous bibliographies of each of the review articles.
- However, upon going through each of those articles, it becomes more and more clear that a description of manganite physics being simultaneously complete, coherent, and well understandable is obviously hard to realize. Rather, it seems to be common practice to simply *itemize* the most important *issues* of manganite physics. Those issues, which clearly happen or are apparent at the same time in a crystal, cannot be linked into a unified phenomenological picture. Not only once authors use phrases such as *puzzle* or *complex interplay*.
- Several reasons for this somewhat confusing situation can be established. First, and to this point all review authors agree, there *is* a complex interplay between different interactions and degrees of freedom that determines the physics of manganites. There is no complete model describing all relevant interactions at once, at least not on a phenomenological level. Among those interactions are in all cases magnetic interactions. The fact that they, in general, can be only fully explained within quantum mechanics does not contribute to a simple intuitive understanding. Second, mixed-valence manganites show very rich electronic and magnetic phase diagrams. Their properties strongly depend on intrinsic parameters, such as the doping level x , type of dopant, or oxygen stoichiometry, and on extrinsic parameters, such as temperature. Consequently, it is often not appropriate to speak of *the* manganites, but each single compound in a certain temperature range must, strictly speaking, be considered separately, which leads to a substantial inflation and complexity of published data on manganites. The other way around, it has to be admitted that the *systematic* observation of certain physical properties, such as conductivity or magnetization as a function of the above-mentioned parameters, has contributed a lot to our current understanding of manganites. Third, it seems that an in-depth clarification of the behavior of manganites (and other correlated-electron materials) is only possible within the framework of modern solid-state theoretical calculations, which are unfortunately not so transparent to the average experimentalist.
- To illustrate the immense intellectual challenge we are confronted with if we try to understand the manganites without any theoretical calculations, let me pose the following question: Is it possible to imagine a solid by *simultaneously* taking care of

- the crystallographic structure including distortions and possible charge order,
- both itinerant and localized $3d$ electrons of the manganese ions with their spins, which are subject to quantum mechanic exchange interactions,
- the coupling of the itinerant electrons to the crystallographic lattice (to phonons) or to the spin lattice, leading to polaron formation,
- the exact geometry/symmetry of the $3d$ orbitals surrounding the Mn ions with their consequences to transport and spin alignment

and finally to derive predictions concerning, e.g., transport and magnetic properties or even whole phase diagrams?

The aim of the above text is not to be discouraging but rather to explain why the following summary of the most important facts on doped lanthanum manganites cannot provide a complete picture. After some historical remarks, I will first comment on the undoped parent compound LaMnO_3 and, second, specify some of the key characteristics of the electronic and magnetic structure of doped LaMnO_3 . The subsection will be closed with a listing of the above-mentioned review articles, including comments on their very different individual approaches to the topic.

2.2.1 Review on manganite research

Early work on polycrystalline $\text{La}_{1-x}\text{A}_x\text{MnO}_3$ (A=Sr, Ca, Pb, Ba) was published by JONKER, VAN SANTEN, and VOLGER in the 1950s [Jon50, Vol54]. They reported on ferromagnetism and metallic conductivity as well as negative magnetoresistance (MR) in a certain composition range. The question as to which type of magnetic exchange mechanism was responsible for the ferromagnetism resulted in the development of the concept of *double exchange* (DE) by ZENER [Zen51] and later by ANDERSON and HASAGAWA [And55] and DE GENNES [Gen60], with the latter two refining the respectively previous DE model. In this model the ferromagnetic interaction of the localized Mn $3d$ electrons is mediated by spin-polarized itinerant $3d$ electrons. Another important theoretical concept that was developed within the course of manganite research is the JAHN-TELLER polaron, see e.g. [Opi57, Pol82].

There was not much activity in the 1970s and 1980s before a revival of the interest occurred in the 1990s. This renewed activity in manganite research was strongly correlated to the desire of a basic understanding of the structurally similar high- T_C superconducting cuprates and to the accompanying expanded possibilities of sample preparation by newly developed thin-film deposition technologies. Large magnetoresistance [Hel93], later

referred to as *colossal magnetoresistance* (CMR) by JIN et al. [Jin94], was found in manganite thin films, and consequently manganites were discussed as potential materials for the arising spintronics technology. To illustrate this outstanding property of a number of manganite compounds, figure 2.3 shows results on the magnetoresistance effect from both periods of intensive manganite research.

To finish this short historical survey, it must be admitted that in the case of the CMR effect the transfer into device technology turned out to be not as straightforward as in the case of the *giant magnetoresistance* (GMR) of metallic multilayers. The main reason lies in the fact that for manganites the Curie temperature T_C is intrinsically inversely proportional to the strength of the MR effect and moreover the highest T_C , as observed for $\text{La}_{0.7}\text{Sr}_{0.3}\text{MnO}_3$, is only around 370 K, which is very low for magnetic device applications. On the other hand, the field of manganites is not yet exhausted and still offers new phenomena and unsolved questions.

2.2.2 The parent compound LaMnO_3

Before we make the attempt to outline some key features of doped lanthanum manganites, we should focus on the physical properties of the parent compound LaMnO_3 , which is in some sense even more complex than its La-substituted relatives. LaMnO_3 is commonly characterized as being an antiferromagnetic insulator in its ground state. The crystallographic structure is heavily distorted, which means that the MnO_6 octahedra are tilted and elongated due to both the mismatch of the ionic radii and a local JAHN-TELLER effect. As a result, the Mn-O-Mn bond angle is much smaller than 180° , namely 155° - 164° , depending upon the exact oxygen stoichiometry. The compound tends to overoxygenation: $\text{LaMnO}_{3+\delta}$. Under oxygen excess, part of the Mn ions, which have a valence of 3+ in the stoichiometric case, are forced to the 4+ valence state to preserve charge neutrality of the crystal. Thus, already the parent compound can show a *mixed* Mn valence, which is the starting point for ferromagnetic ordering and magnetoresistance. Both properties, however, are achieved in a much more effective way by extrinsic doping as described in the next paragraph. Indeed, for $\delta > 0.03$ $\text{LaMnO}_{3+\delta}$ orders ferromagnetically.

The question which type of insulator LaMnO_3 is has been under debate as well, since the compound is a MOTT insulator on the verge of being a charge transfer insulator¹⁶.

¹⁶As discussed in an earlier footnote, a transition-metal oxide might be insulating due to strong electron correlation by COULOMB interaction even when the $3d$ band is only partially filled. This phenomenon is called MOTT insulation and the criterion for its occurrence is that the d bandwidth W is smaller than the correlation energy U , which is also referred to as MOTT-HUBBARD gap. However, especially from optical spectroscopy, it has been found that in certain compounds strong optical absorption occurs below the MOTT-HUBBARD gap [Hüf85]. These absorption peaks are attributed to the bridging of another gap,

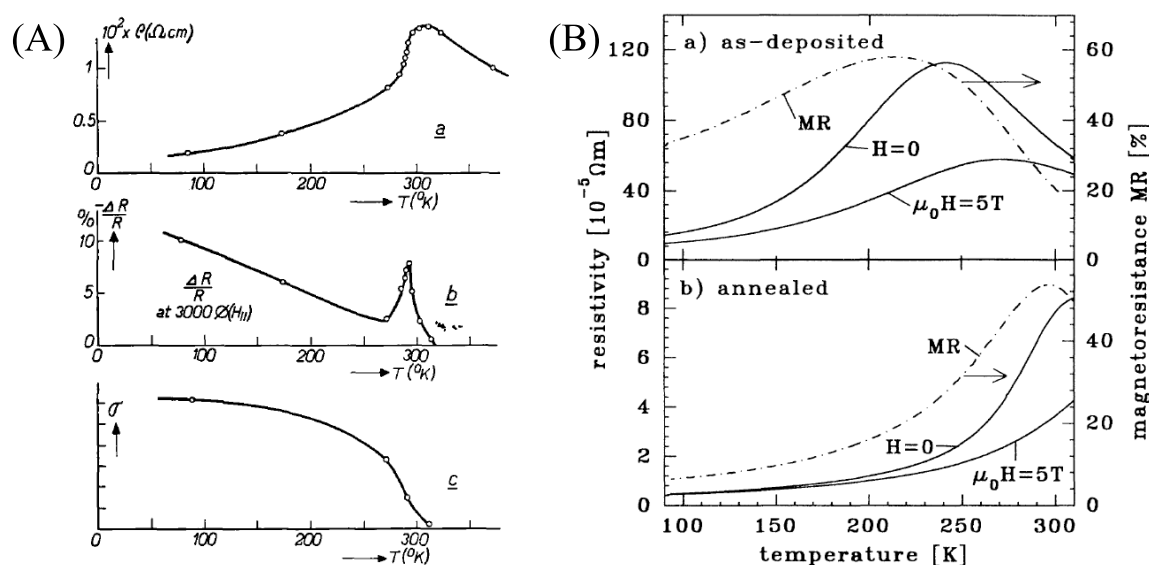


Figure 2.3: Magneto-resistance of manganites.

(A) Reproduction of experimental results on a sintered ceramic $\text{La}_{0.8}\text{Sr}_{0.2}\text{MnO}_3$ sample from the early work of VOLGER [Vol54], which already includes the main features of perovskite manganites. Part c), which is a plot of the saturation magnetization σ against temperature, shows the sample to be ferromagnetic up to the Curie point slightly below 300 K. Intriguingly, as shown in part a), which is a plot of the sample resistivity ρ against temperature, there is also a metal-insulator transition near the magnetic Curie point. Below T_C the sample shows metallic conductivity in the sense of $d\rho/dT > 0$, above T_C it behaves insulating ($d\rho/dT < 0$). Part b) depicts the magneto-resistance at constant magnetic field. The MR value is calculated as the difference between the resistivity at zero field and at a certain magnetic field divided by the zero field resistivity: $\text{MR} = [R(0) - R(H)]/R(0)$. As a further striking fact, the MR peaks at T_C .

(B) Reproduction of data from the work of VON HELMHOLT et al. [Hel93] on pulsed-laser deposition-made epitaxial *thin films* of $\text{La}_{2/3}\text{Ba}_{1/3}\text{MnO}_x$. This work triggered the new interest in manganite research. The data demonstrate again that (i) the samples show a metal-insulator transition, (ii) the MR effect is highest around the transition temperature, and (iii) the MR is negative in the sense that the resistivity drops in response to a magnetic field. Furthermore the strong dependence of the temperature and sharpness of the transition on the degree of disorder and the oxygen stoichiometry can be seen from the comparison of an as-deposited film (a) with a film annealed in air (b). For the latter, one assumes less disorder and a higher oxygen content which decisively raises T_C and decreases the resistivity.

Band structure calculations [Sat96] find LaMnO_3 to have an indirect band gap smaller than 0.5 eV, which agrees with conductivity data (activation energies between 0.1 and 0.36 eV) but is small compared with the charge transfer gap of 1.0 eV or 1.3 eV from optical and photoelectron spectroscopy, respectively.

In summary, the parent compound LaMnO_3 is already a challenging research subject, which is admittedly much more of fundamental than of technological interest and therefore has been much less considered in the literature than the *doped* lanthanum manganites.

the *charge transfer gap* Δ , which arises from transitions between the d band and the oxygen $2p$ band (hybridization). For a detailed discussion of the nature and optical analysis of the different energy scales and energy gaps in strongly correlated systems, such as manganites, see e.g. [Rau06].

2.2.3 Electronic and magnetic structure upon doping

For LaMnO_3 the ion valences are La^{3+} , Mn^{3+} , and O^{2-} in the stoichiometric case and chemical substitution is possible on all lattice sites:

- La^{3+} can be partially replaced by
 - trivalent cations such as rare-earth ions as well as Y^{3+} or Bi^{3+} , where the latter has recently been shown to act as a multiferroic tunnel barrier in the composition $\text{La}_{0.9}\text{Bi}_{0.1}\text{MnO}_3$ [Gaj07],
 - divalent cations such as Sr^{2+} , Ca^{2+} , Ba^{2+} , Pb^{2+} , which, to preserve charge neutrality, forces part of the Mn^{3+} ions to go into the 4+ state, resulting in a mixed Mn valence accompanied by hole doping,
 - monovalent cations such as Na^+ and K^+ ,
 - or, as shown by the research activities of the last decade, tetravalent cations such as Ce^{4+} , Te^{4+} , Sn^{4+} , Zr^{4+} , which force part of the Mn^{3+} ions into the 2+ state. This type of substitution results in a mixed Mn valence, too, but is accompanied by electron doping.
- Mn might be replaced by most $3d$ (e.g. Ti) and some $4d$ (e.g. Ru) elements, which in most cases suppresses ferromagnetic ordering. This case is not considered further here.
- The oxygen content can be enhanced or decreased, the first case being equivalent to metal vacancies, the latter to oxygen vacancies, since no interstitial sites are available in the lattice.

From the above listing it becomes clear that a wide variety of compounds arise by doping of LaMnO_3 . In the present work we focus on divalent-cation substitution of La^{3+} by Sr^{2+} and Ca^{2+} as well as tetravalent-cation substitution by Ce^{4+} . The latter case poses special challenges and is still under debate. We come back to this issue in chapter 4. Here, we limit our considerations to the classical case of divalent-cation substitution, which was already explored in the first period of manganite research. The explanations below follow the train of thoughts from the review article by DÖRR [Dör06].

The physics of manganites is mainly determined by the behavior of the manganese ions. A first valuable step in understanding the mixed-valence manganites is to imagine a simple ionic scheme as depicted in figure 2.4. Mn^{2+} , Mn^{3+} , and Mn^{4+} valence states, which can all occur in manganites depending on the composition, have 5, 4, or 3 electrons

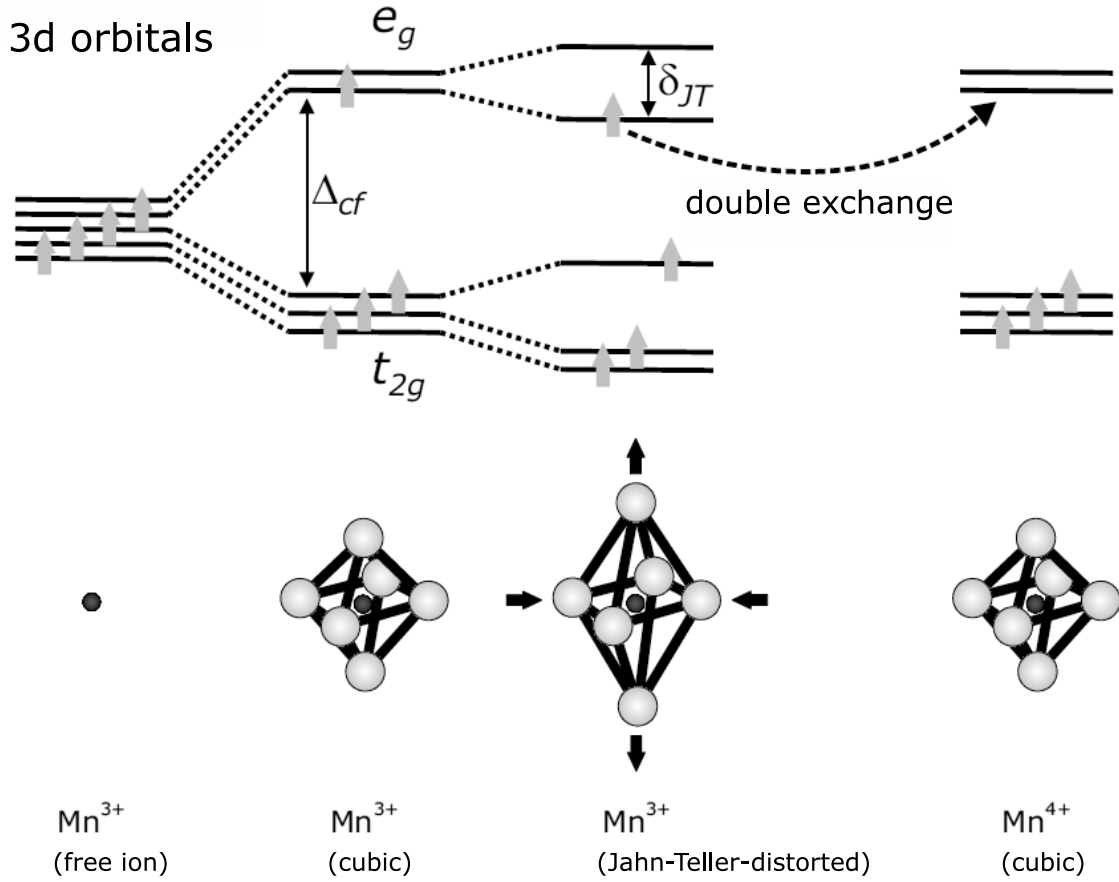


Figure 2.4: Basic properties of the Mn ion in manganites in a simplified single-electron term scheme. While in the isolated Mn ion five degenerate $3d$ levels exist, the crystal field of the oxygen octahedron in the perovskite structure causes a level splitting into three levels with t_{2g} orbital symmetry and two levels with e_g symmetry. The energy difference is denoted as crystal field splitting energy Δ_{cf} ($\Delta_{cf} = 1.8$ eV for undoped LaMnO_3 [Coe99]). Due to the JAHN-TELLER effect around the Mn^{3+} ion the e_g degeneracy is also lifted. The corresponding JAHN-TELLER splitting energy δ_{JT} is typically in the range 1.0...1.5 eV for manganites. The dashed arrow indicates the spin-conservative electron transfer between Mn^{3+} and Mn^{4+} , whereas the intermediate oxygen $2p$ orbital is omitted here. (Reproduced after [Dör06, Thi06].)

in the $3d$ shell. According to HUND's first rule their spins align parallel with a quite large coupling energy $U_H = 2.0$ eV. The crystal field of the surrounding oxygen octahedron splits those five $3d$ levels into three lower-lying t_{2g} levels and two higher-lying e_g levels (the notation derives from group theory). The t_{2g} electrons are localized and form a magnetic core moment of $3\mu_B$. The remaining electrons occupy the e_g levels and are more or less delocalized. In the case of delocalization, the electron movement takes place by hopping via oxygen $2p$ orbitals, with the hopping probability being highest for a Mn-O-Mn bond angle of 180° and decreasing for smaller angles. This hopping mechanism is inherently interweaved with the magnetic exchange interaction: The delocalized e_g electrons couple with their spins parallel to the Mn core moments and thus mediate a ferromagnetic

exchange interaction when moving with conserved spins. As already mentioned within the historical remarks, ZENER worked out a theoretical model for this process [Zen51]: the *double-exchange* model, in which he assumed two *simultaneous* electron hopping processes. One electron is transferred from Mn^{3+} to a neighbouring oxygen $2p$ orbital, and a second electron from this oxygen $2p$ orbital to an adjacent Mn^{4+} ion, with the initial and final states being degenerate and consequently coexisting and coupling the Mn spins ferromagnetically. In general one could say that double exchange means the magnetic interaction mediated by itinerant spin-polarized d electrons which couple to the localized core moments according to HUND's rule. A full understanding of this model is only possible on the basis of corresponding theoretical calculations, which aim at minimizing the total energy of the system.

The above explications provide a phenomenological understanding of the ferromagnetic and conductive ground state of the mixed-valence manganites (at least in a certain composition range), but the origin of the magnetoresistance effect needs further considerations. In a semiclassical approach the double-exchange model yields a certain relation between the electron transfer probability between the two Mn ions and the angle Θ between their magnetic moments. The transfer probability is proportional to $\cos(\Theta/2)$. If an external magnetic field is strong enough to align the Mn moments parallel to each other ($\Theta = 0^\circ$), the transfer probability becomes unity and the resistance drops dramatically.

Furthermore it is noteworthy that, apart from double exchange, superexchange interactions of both Mn t_{2g} and e_g orbitals via O $2p$ orbitals are present. Those interactions can be ferro- or antiferromagnetic depending on the orbital orientation, which demonstrates the importance of the orbital degree of freedom. Since the present work is not related to magnetic properties, we omit an in-depth discussion of this phenomenon.

Besides the strong interconnection between spin and orbital degrees of freedom, as indicated above electron-lattice coupling plays a crucial role in manganite physics. There are two different sources of electron-lattice coupling. First, as already noted, the Mn-O-Mn bond angle varies depending on the misfit of the anion radii. The reduction of this bond angle goes along with a decrease of the conduction bandwidth due to a smaller orbital overlap. The second source of electron-lattice coupling is the JAHN-TELLER effect¹⁷,

¹⁷The JAHN-TELLER effect in its simplest form is an effect in molecular physics and was described by JAHN and TELLER in the 1930s. It assumes a vibrating molecule where a multiplicity of electronic states interact with one or more modes of vibration. The theorem says that for almost any set of degenerate electronic states associated with a (geometrical) molecular configuration there will exist some symmetry-breaking interaction in which in turn the molecular distortion is created simultaneously with the removal of the electronic degeneracy. The proof is given by a group theoretical argumentation. The effect is observed also in solids, where the electrons interact with lattice vibrational modes (phonons). For a review see e.g. [O'B93].

which can be either static or dynamic depending on the composition and temperature regime. Basically, the Mn^{3+} ion deforms its surrounding oxygen octahedron. This distortion goes along with the lifting of the degeneracy of the e_g states. The motion of such e_g electrons leads to the formation of polarons, the JAHN-TELLER polarons. Again, a detailed understanding is not possible without entering solid-state theory.

Regarding the subtle interplay between different degrees of freedom that we have tried to introduce so far, it is not surprising that lanthanum manganite systems show rich phase diagrams with respect to their electronic and magnetic structure. For two of the most investigated systems, which were also under inspection in the present work, namely $\text{La}_{1-x}\text{Sr}_x\text{MnO}_3$ (LSMO) and $\text{La}_{1-x}\text{Ca}_x\text{MnO}_3$ (LCMO), such phase diagrams are depicted in figure 2.5. The technologically interesting ferromagnetism occurs in a limited composition range with a maximum CURIE temperature T_C for $x = 0.3$. For this composition, both compounds exhibit a ferromagnetic metallic low-temperature phase, which appears logical from the point of view that electronic conduction and ferromagnetism are inherently coupled within the double-exchange mechanism. The ferromagnetic-to-paramagnetic phase transition is accompanied by a metal-to-insulator transition in the case of LCMO, while LSMO, which has the highest T_C among the doped lanthanum manganites, stays metallic (however with a reduced slope of the resistivity-versus-temperature characteristics). We have to note that, according to latest publications, those phase diagrams are still simplified. It has been proven that manganites tend to phase coexistence within a chemically homogeneous state. To be complete, figure 2.6 shows the phase diagram of $\text{La}_{1-x}\text{Ce}_x\text{MnO}_3$ (LCeMO), which was also under investigation in this thesis. In contrast to LSMO and LCMO, LCeMO is nominally electron-doped due to its mixed $\text{Mn}^{2+}/\text{Mn}^{3+}$ valence resulting from tetravalent-ion doping. The phase diagram is valid only for epitaxial thin films, since single-phase bulk samples seem to be impossible to synthesize, as will be discussed in detail in chapter 4. The CURIE temperatures are similar to those of the hole-doped LCMO system.

2.2.4 Additional physics of manganites

Since the above introduction to the physics of doped lanthanum manganites is far from being complete, the section will be closed by a chronological listing of some review articles on the field. The very different approaches of the authors are just another indicator of the extreme complexity of the topic.

- The article of RAMIREZ [Ram97] is entitled *Colossal magnetoresistance* and considers not only the mixed-valence manganites, but also other compounds that show

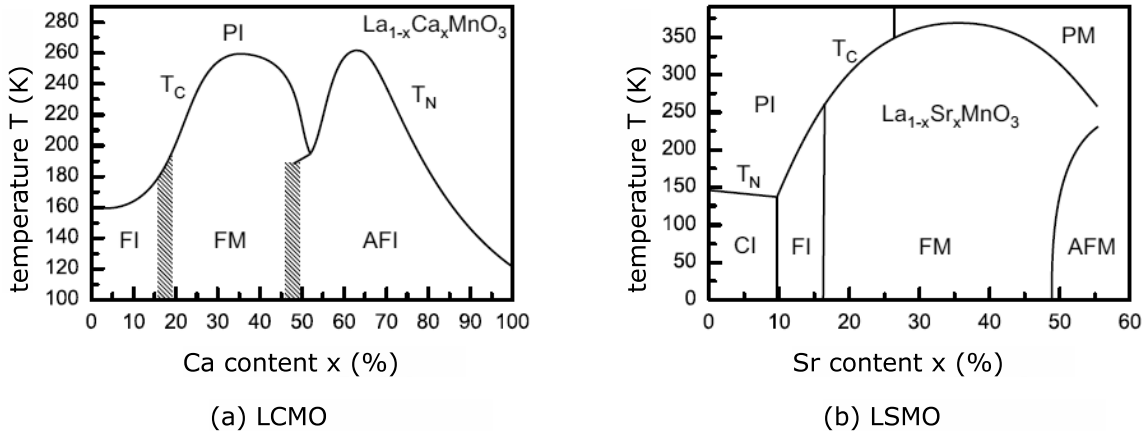


Figure 2.5: Phase diagrams of the hole-doped systems $\text{La}_{1-x}\text{Sr}_x\text{MnO}_3$ (LSMO) and $\text{La}_{1-x}\text{Ca}_x\text{MnO}_3$ (LCMO). The abbreviations are to be interpreted as follows: F - ferromagnetic, AF - antiferromagnetic, P - paramagnetic, C - canted magnetic order, T_C - CURIE temperature, T_N - NÉEL temperature, I - insulating, M - metallic. (Reproduced from [Ram97].)

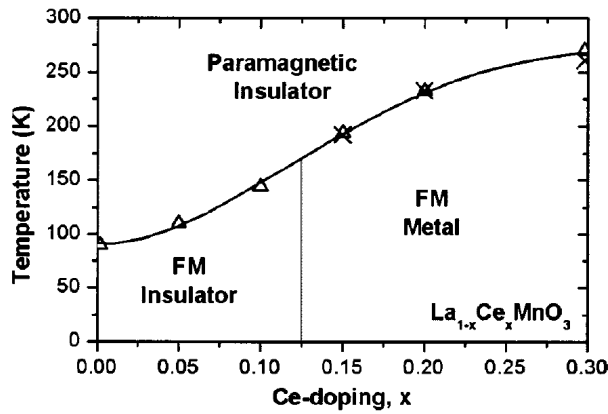


Figure 2.6: Phase diagram of the electron-doped system $\text{La}_{1-x}\text{Ce}_x\text{MnO}_3$ (LCeMO). FM stands for *ferromagnetic*. Note that a single-phase preparation is only possible for thin films in a limited composition range. (Reproduced from [Ray03].)

the CMR effect, such as certain spinels and pyrochlores. The article is a collection of experimental results, aiming at a phenomenological understanding of CMR compounds. The validity of a simple band picture is questioned for the manganites, because HALL and thermopower results do not correspond to the nominal conduction type. Especially for the lanthanum manganites the different dopings (Sr, Ca, Ba) leading to quite different physical properties are discussed individually and in detail.

- One of the most complete compilations of knowledge on mixed-valence manganites can be found in the paper by COEY et al. [Coe99]. The authors tackle the topic from the materials science point of view. A profound base of knowledge concerning

the historical results on manganites, fundamental magnetic interactions in solids, magnetic semiconductors in general, as well as bulk and thin-film preparation is given. The electronic structure is discussed in the ionic picture as well as in the band picture, and the most important results from measurements of magnetic properties, electronic and thermal transport, and of the optical response are summarized.

- In contrast to [Coe99] MOREO et al. [Mor99] strongly stress the importance of phase separation scenarios in theory and experiment. Refined phase diagrams for LSMO and LCMO are presented.
- The article by SALAMON et al. [Sal01] points out the significance of the manganites as a model system for modern solid-state theory due to the many degrees of freedom, and emphasizes the role of theory for a *complete* understanding of those compounds. The key feature of the paper is that listings of the most important phenomenological facts in manganite physics are given for different *temperature regimes*, since manganite behavior is very different above and below T_C .
- In the mainly theoretically oriented paper by EDWARDS [Edw02] the author limits his considerations to doped manganites in the ferromagnetic regime ($x=0.2 \dots 0.4$) and highlights the role of electron-phonon coupling. The different behaviors of LCMO and LSMO above T_C are explained as a result of diverse degrees of localization of the e_g electrons. The role of disorder is stressed. The author prefers the band rather than the ionic picture. For instance, photoemission spectra of LCMO, in which a FERMI edge becomes visible below T_C are discussed as evidence that, within certain limits, the manganites can be described within the terminology of a band model.
- Another theoretical work is that by GOR'KOV et al. [Gor04], where the main features of mixed-valence manganites are explained by *analytical* calculations. It is explained which interactions play a role and how they contribute to the Hamiltonian of the whole system. The authors deal separately with low- and high-doping regimes and with metallic and insulating phases. Special attention is drawn to percolation (phase separation) phenomena and to interface and tunneling phenomena.
- The review papers of HAGHIRI-GOSNET et al. [HG03] and DÖRR [Dör06] lay a special focus on manganite *thin films* and possible device structures. Besides summaries of general manganite physics, the role of epitaxial strain in thin films is discussed as an additional and controllable degree of freedom.

2.3 Oxide samples of the present study

As sample preparation was performed at the IFW Dresden and thus was not part of this thesis, only the most important information will be given here. For an in-depth description of the deposition technique and the film growth conditions, refer to the thesis of C. THIELE [Thi06].

Epitaxial thin films of 10 nm $\text{La}_{0.7}\text{Ca}_{0.3}\text{MnO}_3$, 10 nm $\text{La}_{0.7}\text{Ce}_{0.3}\text{MnO}_3$, and 15 nm $\text{La}_{0.7}\text{Sr}_{0.3}\text{MnO}_3$ were deposited on undoped $\text{SrTiO}_3(100)$ single-crystal substrates¹⁸ of $10 \times 10 \times 0.5 \text{ mm}^3$ by pulsed-laser deposition in off-axis geometry. For comparison, one 15-nm-thick $\text{La}_{0.7}\text{Sr}_{0.3}\text{MnO}_3$ film was also grown on Nb-doped SrTiO_3 (0.5 wt%). Stoichiometric targets were ablated with a KrF excimer laser at a wavelength of 248 nm.

X-ray diffraction (XRD) measurements were employed to ensure single-phase and epitaxial growth.

All films were additionally characterized by atomic force microscopy in the contact mode in air. The AFM measurements revealed a root-mean-square roughness of 1 nm, 2 nm, and 7 nm for LCeMO, LCMO, and LSMO, respectively.

The samples were cut into halves. One half of each sample was loaded into an ultrahigh-vacuum environment for the photoelectron-spectroscopy-based investigations (chapter 4), the other halves were kept in air for surface photovoltage investigations (chapter 3). After completion of the photoelectron spectroscopy study, those sample halves were moved back into air and also studied by surface photovoltage measurements.

Now we finish our view on oxide physics, being aware of not having considered all points of importance. Some special issues that are directly related to the experimental studies of the present thesis, such as the formation of the manganite/strontium titanate interface including its photoresponse and the challenge of electron doping of manganites, are reviewed in chapters 3 and 4, respectively.

¹⁸The supplier was Crystec GmbH, Berlin. The substrates were polished to a root-mean-square (rms) roughness smaller than 0.5 nm.

3 Surface photovoltage investigations of the manganite/SrTiO₃ interface

In the following we introduce the technique of surface photovoltage (SPV) spectroscopy as a unique tool to identify and classify electronic defect states at oxidic interfaces, especially the manganite/ strontium titanate interface. After some considerations on SPV in general and with respect to oxides in particular, a comparative study of the electronic interface state distribution at three different perovskite oxide interfaces, formed by epitaxial thin films of La_{0.7}Sr_{0.3}MnO₃ (LSMO), La_{0.7}Ca_{0.3}MnO₃ (LCMO), and La_{0.7}Ce_{0.3}MnO₃ (LCeMO) on SrTiO₃ substrates, is presented. The information content and applicability of different experimental approaches are discussed critically.

3.1 Fundamental considerations

3.1.1 The physics of surface photovoltage phenomena

The subsequent overview, which is based on the comprehensive review articles by KRONIK and SHAPIRA [Kro99, Kro01], of the physical background of surface photovoltage has been kept as phenomenological and intuitive as possible, since the presentation of all formal and mathematical details¹ would clearly go beyond the scope of the present work. Depending on the case (i.e. the concrete material or device structure) SPV is, in principle, capable of providing information on a variety of quantities, e.g., the carrier diffusion length, surface band bending, surface charge, and surface dipole, as well as surface and bulk recombination rates, distribution and properties (time constants and optical cross sections) of surface states, distinction between surface and bulk states, conduction type, or construction of band diagrams.

¹Typically, mathematical descriptions of SPV phenomena are not general but start from rigid assumptions, e.g. constant recombination rates throughout the space charge region (SCR), the existence of only one surface state, the existence of a depletion regime, a certain signal level (small- and large-signal SPV), unipolar carrier excitation, a certain quantum efficiency, certain doping and temperature regimes, a diffusion length larger than the SCR, the existence of an ohmic back contact, and the neglect of bulk states and intra-conduction-band transitions. Especially for a material with a quite low carrier concentration, such as undoped SrTiO₃, at least the condition that the SCR has to be smaller than the diffusion length is violated with the result that a quantitative analysis is not straightforward.

Historically, SPV phenomena were already known during the pioneering period of semiconductor physics, i.e., back in the 1940s and 1950s (see e.g. [Joh58]). SPV in classical semiconductors such as Si and Ge is well understood and industrially employed for the contamination analysis of wafers [Lag92, Sch06]. For wide-bandgap materials, where purely electrical characterization methods fail due to low carrier concentrations – and this applies to our study – SPV has been found to be a valuable tool for surface gap state spectroscopy since the 1970s [Gat73, Lag94].

3.1.1.1 Electronic structure of semiconductor surfaces

An indispensable prerequisite for a later understanding of SPV phenomena is the examination of the basic electronic properties of semiconductor surfaces. We note here that the terms *surface* and *interface* mean the same thing, namely the boundary between two media with different physical properties. Commonly, the term *surface* is used for the boundary between a solid and a gas or vacuum and the term *interface* is used for the solid-solid boundary. The first case is also called *free surface* and will be considered here first.

The periodic structure of an ideal crystalline semiconductor results in the occurrence of allowed energy bands separated by forbidden gaps. The termination of such a periodic structure at a free surface leads to a number of effects which are subject to an own area of solid-state physics: surface physics. Roughly speaking, this termination involves not only symmetry breaking but also more complex processes, e.g. lattice relaxation, the formation of dangling bonds, steps, and kinks, or adsorption of impurity atoms. In the band picture, those structural changes are inevitably connected with the formation of surface-localized electronic states within the semiconductor band gap and/or a double layer of charge, known as surface dipole.

In order to establish thermal equilibrium between bulk and surface, characterized by a constant FERMI level throughout the crystal, a charge redistribution between the two must take place. Consequently the surface carries a charge that is balanced by the same amount of an opposite space charge in the bulk, which depletes² the subsurface layer of majority carriers. According to POISSON's equation, such a charge distribution results in an electric field, also named *built-in field*, accompanied by a band bending. Furthermore, the band bending can be interpreted as an energy barrier, the so-called SCHOTTKY barrier, for majority carriers moving towards the surface. The term SCHOTTKY barrier originally stems from the theory of rectifying metal-semiconductor junctions, also known

²In most reports on this topic only the case of depletion is discussed. Of course, also accumulation or inversion might occur.

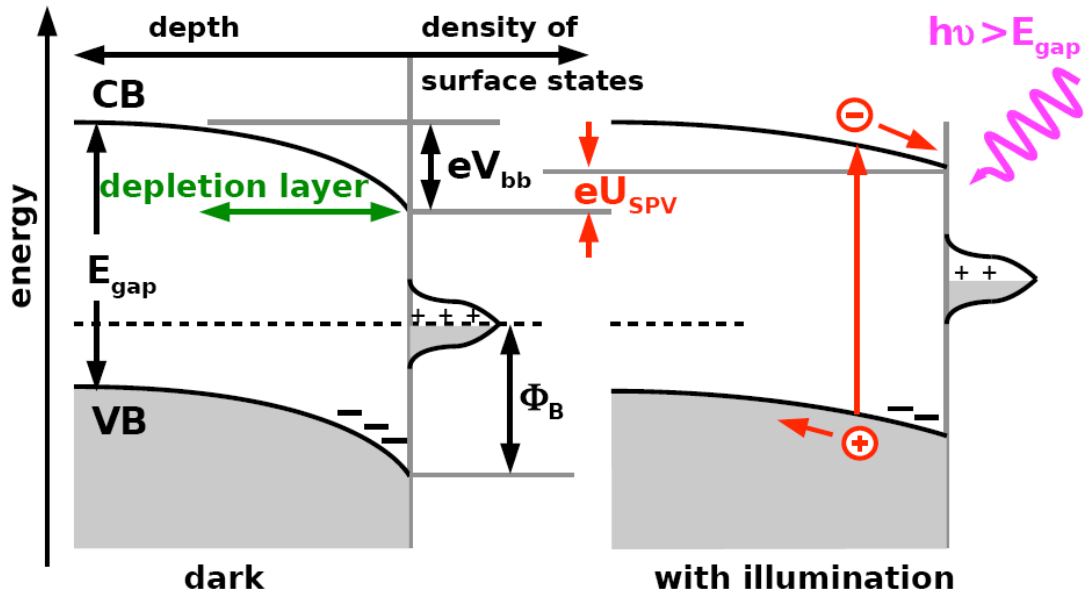


Figure 3.1: Bands in the subsurface region of a depleted p-type semiconductor having surface states within the band gap, shown without and with super-bandgap illumination. U_{SPV} denotes the surface photovoltage, V_{bb} the band bending, and ϕ_B the SCHOTTKY barrier.

as SCHOTTKY contacts, which show a pretty similar physical behavior, see e.g. [Bri82].

3.1.1.2 The surface photovoltaic effect

When a semiconductor surface with a built-in field is illuminated by light with a photon energy greater than the band gap, electron-hole pairs are generated and separated by the built-in field. Thus, again a charge redistribution takes place along with a change of the band bending. The shift of the band bending compared to the equilibrium value is called surface photovoltage. The situation is visualized in figure 3.1.

A SPV is also observed when the surface is illuminated with photon energies smaller than the band gap, due to the photostimulated population and depopulation of distinct and energetically localized trap states within the band gap (figure 3.2). The effect is also called sub-bandgap SPV and has been realized to be the key to a nondestructive versatile tool for analyzing the distribution of gap states: *surface photovoltage spectroscopy (SPS)*. The principle is as follows: The wavelength of the incident photons is swept and the corresponding SPV is recorded. Population or depopulation of a distinct trap state will become visible in the SPV-vs.-wavelength plot as a point of slope change. Thus a mapping of trap energies E_t across the band gap can be performed and the trap levels can be classified into those which communicate with the conduction band and those which exchange carriers with the valence band. Figure 3.3 depicts a SPV spectrum and the

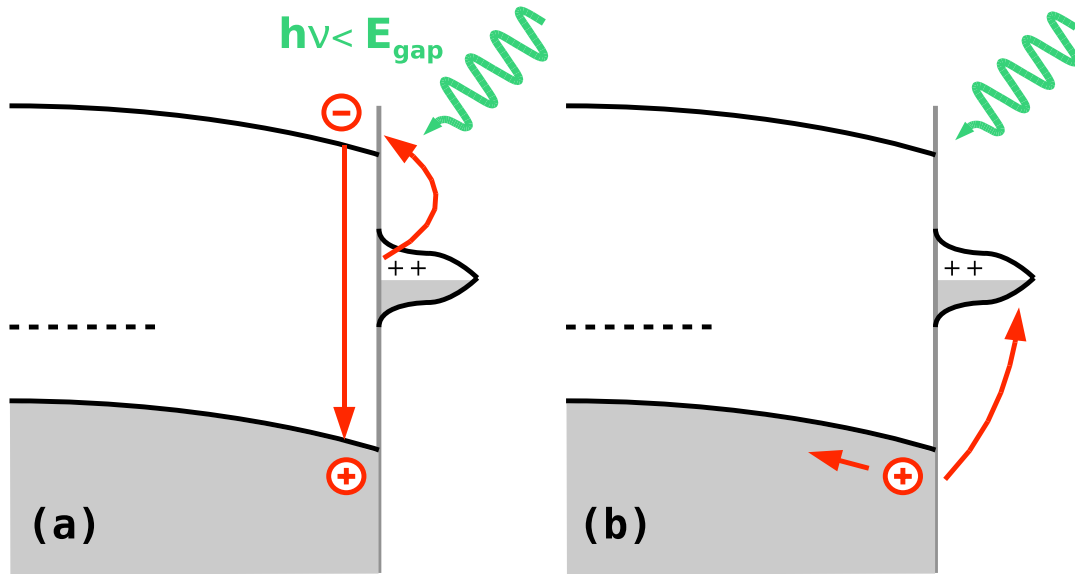


Figure 3.2: Under sub-bandgap illumination, a surface photovoltage can be generated by direct charge exchange between gap states and one of the bands. Part (a) shows the excitation of an electron from a surface state to the conduction band. The SPV is lowered in this case provided that there is significant recombination between the bands or (not shown in the picture) significant diffusion into the bulk. Part (b) illustrates how an electron is excited from the valence band into a surface state, leading to an increase of the SPV. Note that also more complex scenarios, such as transfer between gap states, are possible.

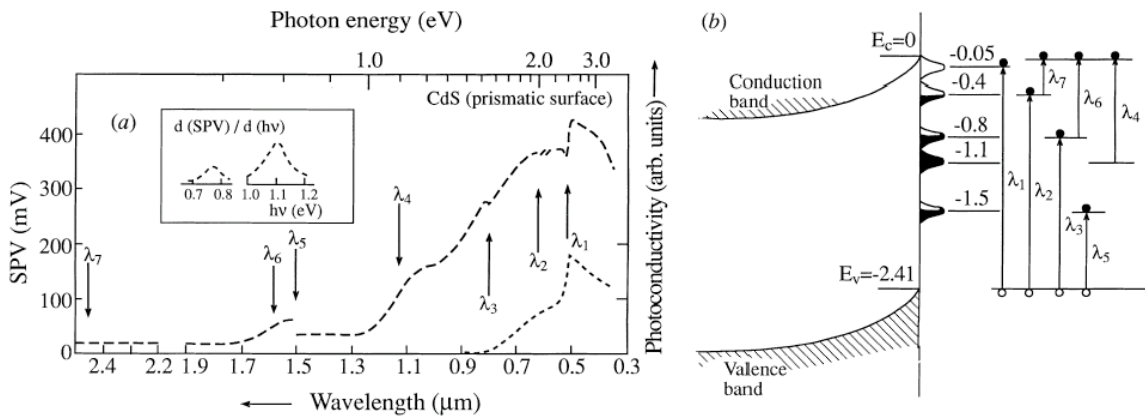


Figure 3.3: Reproduction of an early SPV spectrum from a n-type CdS surface from [Bal71]. Part (a) depicts both the SPV and the photoconductivity spectrum, where the first is interpreted in terms of slope changes, which are indicated by arrows. The energetic (or wavelength) positions are assigned to carrier transitions between localized surface states and one of the two bands [part (b)]. Unfortunately, up to now no generally accepted method has been established concerning the exact analysis of SPV spectra. Thus, questions, such as why the slope changes at around 1.0 eV or 1.2 eV are not assigned to a transition, but also similar inconsistencies in other SPS publications, remain unanswered or uncommented.

assignment of the slope changes to gap states from an early SPS publication about the CdS surface [Bal71].

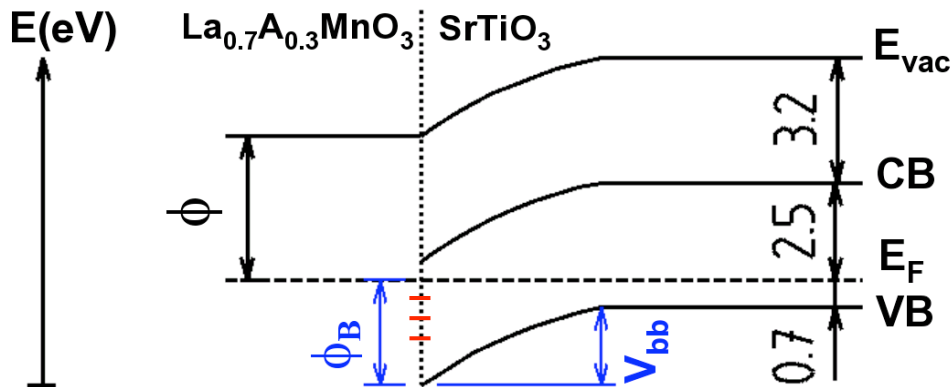


Figure 3.4: Assumed band alignment at the manganite/SrTiO₃ interface (A in the chemical formula stands for either Sr, Ca, or Ce). Here, ϕ denotes the work function of the manganite film, ϕ_B the SCHOTTKY barrier, and V_{bb} the band bending. The ϕ values were determined by an ultraviolet photoemission (UPS) experiment (for details see chapter 4) and evaluated to be 5.2 eV for LSMO, 4.8 eV for LCMO, and 5.1 eV for LCMO. The values of the FERMI level position and the work function of undoped SrTiO₃ have been taken from [Ded93]. Note that the depicted case is, strictly speaking, only valid for LSMO, see text. In this case we get a total band bending of 0.5 eV. We further note that for the above scheme the so-called SCHOTTKY limit (no Fermi level pinning) was assumed, which is, according to certain literature results [Sch78], not the case for SrTiO₃, so that the true band alignment cannot be fully reconstructed from only the difference of the electron affinities.

3.1.1.3 Sensitivity to buried interfaces

Naively one could think that interfaces that are buried deep enough into a sample are unable to contribute to the SPV signal, due to screening by a thick-enough quasi-neutral region. However, this statement is wrong. To explain why, we assume a simple heterostructure: a thin semiconductor film on a semiconductor substrate, both with different material parameters. In such a structure we expect two different space charge regions (excluding the back contact, which is assumed to be ohmic): one at the junction (buried) and one at the free surface of the film. Since the energy bands of both materials are connected *in series*, the potential of the free surface (where the SPV is finally probed, see the following sections) is linked to any other illuminated region inside the whole structure. Thus the optical absorption in *any* non-neutral region of the sample might contribute to the SPV signal. In other words, any interface that produces a space charge region and is optically accessible can potentially be characterized by surface photovoltage measurements. Albeit the separation of different SPV contributions in heterostructures is quite a challenge, SPV techniques have been extensively employed in the characterization of buried interfaces, mainly within the research on III-V semiconductor heterostructures.

In the case of the manganite/SrTiO₃ interfaces investigated here, we expect a SCHOTTKY contact in the case of La_{0.7}Sr_{0.3}MnO₃, since this manganite shows metallic conductivity at room temperature and SrTiO₃ may be modeled as a wide-bandgap semiconductor.

For the two other manganites considered here, $\text{La}_{0.7}\text{Ca}_{0.3}\text{MnO}_3$ and $\text{La}_{0.7}\text{Ce}_{0.3}\text{MnO}_3$ we expect semiconductor heterojunctions, because both materials have band gaps at room temperature, which are, however, smaller than 1 eV (see section 2.2). Nevertheless, for all three cases we expect the essential preconditions for a measurable SPV signal, namely space charge regions and optical accessibility at/of the interface, to be fulfilled, which justifies our experimental approach. Further details on the assumed band alignment are given in figure 3.4.

3.1.2 Electronic interface states of SrTiO_3 and ferroic systems - a literature review

For a better consolidation of the experiments presented below, we summarize the current state of research with respect to the investigation of the electronic properties³ of ferroic, or more generally, perovskite interfaces by techniques based on optical excitation. Since the examination of an interface needs the familiarization with either of the participating materials, we first give an overview of the knowledge on electronic states at pure SrTiO_3 surfaces and conventional metal/ SrTiO_3 interfaces. We will close the subsection with a description of some promising nonoptical, solely electrical investigations on perovskite interfaces.

3.1.2.1 Electronic properties of SrTiO_3 surfaces and interfaces

According to the statements of section 2.1, it is almost self-explaining that the inspection of inner and outer SrTiO_3 interfaces has constituted a challenge for several decades and is still in progress. The main reason for this elaborateness is again the dramatic change of the electronic properties even by small changes of the oxygen stoichiometry, as was demonstrated e.g. by photoelectron spectroscopy [Pow76, Hen78]. Furthermore, the treatment within the framework of the common semiconductor band diagrams turns out to be partially critical, since at least undoped SrTiO_3 has a such a very low carrier concentration that a strict consideration within the terms of classical semiconductor physics is highly questionable⁴. However, most of the studies mentioned below used doped SrTiO_3 (the reasons were discussed in section 2.1), where the band diagram should be applicable.

³We do not discuss structural interface investigations with cross-sectional transmission electron microscopy (TEM) and with TEM-derived techniques such as electron energy-loss spectroscopy (EELS) or electron energy-loss near-edge spectroscopy (ELNES), despite the fact that EELS and ELNES are sensitive to the electronic structure in the sense of spatially resolved valence sensitivity. Results on LSMO and the LSMO/ SrTiO_3 interface can be found in [Rie07] and [Mau06], respectively.

⁴Let us illustrate this statement with an example: We consider the LSMO/ SrTiO_3 interface as a SCHOTTKY contact and calculate the depletion width W in SrTiO_3 according to the well-known formula

Especially the fundamental question whether SrTiO₃ tends to intrinsic surface states and subsequent strong FERMI level pinning (BARDEEN limit) or not (SCHOTTKY limit) was discussed controversially [Kur69, Sch78]. While the first work mentioned assumes the SCHOTTKY limit, the latter one - after the evaluation of a comparative study of different metal/SrTiO₃ junctions - considers SrTiO₃ as an intermediate case [Nev72]. The SCHOTTKY barrier heights were determined by I-V measurements⁵ and photoresponse techniques.

In an earlier work, electrical characterization techniques (I-V, C-V measurements) were applied as well, in order to investigate the rectifying behavior of several metal/SrTiO₃ contacts [Car67].

Anomalous C-V characteristics of metal/SrTiO₃ junctions were found within another study [Nev75] and interpreted in terms of the formation of a heavily doped SrTiO₃ layer at the interface during the metal evaporation process. This highlights how difficult it is to prepare a high-quality SrTiO₃ surface and to keep this quality during further processing.

In recent times, within the framework of the search for alternative gate oxides, further activities aiming at an understanding of the band alignment at interfaces of SrTiO₃, especially its interface with silicon, were reported [Zha03, Dem04]. There, a good agreement between experiment and theory (density functional theory, DFT) was found.

Similarly to one of the early works on the topic [Nev75], a recent investigation of the relation between the diode behavior of a Au/SrTiO₃:Nb junction and the crystallographic orientation of the SrTiO₃ substrate found that an interlayer having a different dielectric constant forms [Shi00]. The same problem of unintentional interlayer growth was discussed for a SrTiO₃/p-Si heterojunction [Hun06].

So far, only few interface studies employing photovoltaic effects⁶ have been reported, e.g. the studies of ZHAO and coworkers, who reported on a strong photovoltaic effect in a SrTiO₃/Si junction [Zha05] and a high open-circuit photovoltage of SrTiO₃ single crystals [Zha06]. In both cases ultraviolet and thus super-bandgap illumination was applied with no attention paid to possible gap states. One real *surface* photovoltage study employing

[Sze81] $W = \sqrt{\frac{2\epsilon\epsilon_0}{qN} \left(V_{bi} - \frac{kT}{q} \right)}$. We use $\epsilon = 310$ as the static dielectric constant for SrTiO₃, $V_{bi} = 0.7$ eV as the built-in potential (which corresponds to the band bending in figure 3.4) and $N = 5 \times 10^{13} \text{ m}^{-3}$ as the acceptor concentration (which corresponds to the hole concentration in insulating SrTiO₃ crystals as determined in [Ded93] from transport measurements). Then, the an extremely large value results for W , namely around 14 cm, which is much larger than the sample thickness. Obviously, several of the assumptions that lead to the above formula, such as complete ionization of all acceptors and the validity of the already discussed SCHOTTKY limit, are not true in our case.

⁵Two very common interface-sensitive methods to characterize semiconductor device structures are current-voltage (I-V) and capacitance-voltage (C-V) measurements, see e.g. [Sch06].

⁶We omit all studies dedicated to SrTiO₃ within solar cell structures and within manganite heterostructures, since the latter are reviewed in the next subsection.

both sub- and super-bandgap illumination described two distinct energetically localized surface states near midgap with different response time constants as derived from SPV transients [Mav78].

Finally, it must be stressed that at least the interlayer problem seems not to be relevant for manganite/SrTiO₃ interfaces as proven by numerous cross-sectional transmission electron microscopy investigations, which show sharp atomic interfaces (primarily due to the relatively small lattice misfit within the perovskite family).

3.1.2.2 Photon-assisted spectroscopy for the investigation of ferroic interfaces

The application of spectroscopic techniques based on optical excitation of the surface or interface of interest to the manganite/SrTiO₃ system has taken place only rudimentarily so far. Thus we include in our survey also (i) other ferroic interfaces, such as interfaces with the widely studied, highly interesting lead zirconate titanate (PbZr_{1-x}Ti_xO₃, PZT) system, and (ii) spectral measurements not only of the SPV but also of photocurrents, which are also sensitive to gap states:

A photovoltaic effect under ultraviolet illumination has been shown to occur in heterojunctions of e.g. La_{0.8}Sr_{0.2}MnO₃/SrTiO₃:Nb [Mur04], La_{0.7}Ce_{0.3}MnO_{3- δ} /SrTiO₃:Nb [Sun04], and PZT/SrTiO₃ [Wat04], but those experiments were not *spectroscopic* in the sense of a *wavelength-dependent* mapping of photoinduced quantities, and the works were not dedicated to the detection of electronic states within the SrTiO₃ band gap.

Thin PZT films with Pt electrodes were investigated by measuring the transient photocurrent, which was recorded as a function of the ferroelectric polarization, with the incident photon energy corresponding to the PZT band gap (3.5 eV) [Kho98]. The possibility to read the polarization state of the material in a nondestructive manner by this method was discussed. Photocurrents in a decisively larger spectral range (4.5...2.6 eV) were investigated by YANG et al., again for PZT films [Yan99]. The deviation of the photocurrent spectrum from a LORENTZIAN fit curve was taken as a hint to the existence of oxygen and Pb³⁺ centers within the PZT bandgap. Furthermore, significant features at wavelengths corresponding to the indirect and first direct bandgaps of PZT confirmed that the method maps the electronic band structure. Moreover, the spectrum was taken after different numbers of switching cycles and fatigue was demonstrated. Detailed information on modulation frequencies, photon flux, and on assumptions made on the band alignment are, however, missing. The same group acquired I-V characteristics of a Pt/PZT/Pt capacitor structure with and without UV illumination, but without varying the wavelength [Yan00]. The wavelength-dependent photoconductivity across a

PZT:Nb/Pt junction [Boe04] and a Au/PZT/Pt structure [Boe03] was investigated and significant contributions within the PZT bandgap were found, but the fine structure of the spectra was not discussed.

3.1.2.3 Interface investigations of perovskite heterostructures without optical excitation

There are several examples in the literature of ferroic interfaces being treated as a SCHOTTKY diode whose properties are accessible by I-V measurements. That way, BLOM et al. [Blo94] modeled the Au/PbTiO₃ junction within the SCHOTTKY model, taking the variable polarization of the ferroelectric into account, and interpreted experimental results within this frame, but neglected the problem of discrete interface states.

In the more recent literature, further work on I-V characterization of perovskite SCHOTTKY contacts has appeared. For instance, interfaces of SrRuO₃/SrTiO₃:Nb [Fuj05] or the manganite/SrTiO₃ contacts Pr_{0.7}Sr_{0.3}MnO₃/SrTiO₃:Nb and La_{0.7}Sr_{0.3}MnO₃/SrTiO₃:Nb [Saw05] were investigated, with the latter paper also presenting suggestions concerning the band alignment.

Only very few examples of the measurement of *energetically localized electronic interface states* with concrete values of their energetic *positions* and the *density* of states within the bandgap on perovskite structures exist, among them the DLTS (deep-level transient spectroscopy) analysis of TiO₂/SrTiO₃:Nb [Miy01], Pt/PZT/Ir [Del05], and Au/PZT/ZrO₂ [Fuj03].

3.1.2.4 Conclusions drawn from the literature results

In summary, we notice that a systematic, comparative and – with respect to interface quality – evaluative application of surface photovoltage spectroscopy to perovskite and/or ferroic inner and outer interfaces, especially the manganite/SrTiO₃ interface, has not been realized so far. This is the strong motivation behind the present study, since the progress in the field of oxide electronics seems to be decisively determined by the quality of the interfaces, because the functional properties have been shown to be crucially influenced by the distribution of intrinsic and defect-related electronic interface states. Not for nothing is the outstanding success of silicon mainly based on the high achievable quality of the Si/SiO₂ interface.

3.2 Experimental approaches and results

Many elaborate techniques - all of them show specific advantages and drawbacks - have been developed to measure the surface photovoltage. They include all methods that are able to measure the surface work function, since, if we reexamine figure 3.1, we find that the SPV is nothing else than the surface work function difference between the dark and the illuminated state. The two most common methods are the KELVIN probe and the capacitive SPV detection under modulated illumination. Other, less used, methods are based on photoelectron spectroscopy and electron beam analysis. Furthermore two scanning probe techniques, namely scanning tunneling microscopy (STM) and KELVIN probe force microscopy (KPFM), under additional optical excitation can be employed to measure the (spatially resolved) SPV.

In the present study, three different experimental approaches were chosen to acquire SPV spectra of the manganite/SrTiO₃ interface and, for comparison, of the SrTiO₃ surface: x-ray photoelectron spectroscopy under additional optical excitation (in the following denoted by X-SPS), the capacitive SPV detection under modulated illumination (C-SPS), and the KELVIN probe technique (K-SPS). In what follows, the implementation of those methods is described and the respective results are presented and critically discussed (in historical order), after some details on sample illumination have been pointed out.

The experimental details on sample preparation and structural characterization were already given in section 2.3.

3.2.1 Sample illumination

The illumination setup (see figure 3.5) used in this study is, apart from slight modifications, the same for all SPV detection methods. A 1000-W xenon arc lamp⁷ serves as a white-light source, offering a usable spectrum between 280 nm and 780 nm. The hot spot of the light arc is focused on the entrance slit of a grating monochromator⁸ by a pair of fused-silica lenses. The light exiting the monochromator passes an edge filter⁹

⁷The Xe arc lamp from Oriel Instruments was operated with the appropriate lamp housing and power supply from the same manufacturer. In the meantime the product line is distributed by Newport Instruments.

⁸Cornerstone 260 by Oriel Instruments: grating monochromator in asymmetric CERNY-TURNER configuration, equipped with two interchangeable diffraction gratings with blaze wavelenths of $\lambda_b = 400$ nm and $\lambda_b = 750$ nm.

⁹Depending on the scanned wavelength range, filters with cut-off wavelengths of 550 nm, 395 nm, and 310 nm were used. The filters were changed manually while the beam path was completely blocked, since already a small amount of high-order diffraction photons would create a super-bandgap SPV, which is orders of magnitude higher than the sub-bandgap SPV and decays only over hours.

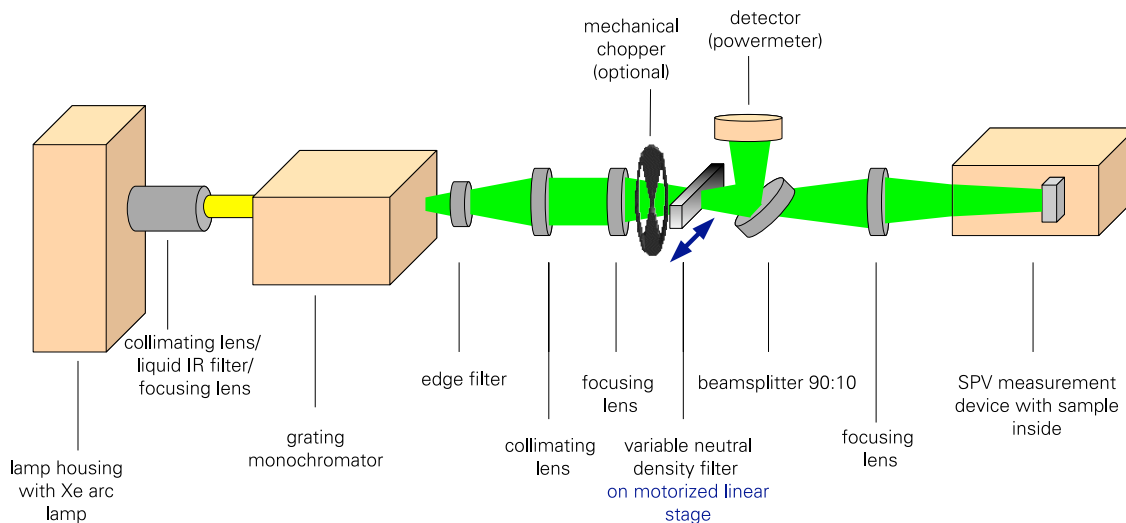


Figure 3.5: Illumination setup for surface photovoltage spectroscopy. Note that for X-SPS the sample is not in a shielding box in air as shown here, but in an ultrahigh-vacuum chamber with a fused silica viewport. The remote connections of monochromator, the translation stage, the powermeter, and the SPV signal are, for convenience, not shown here. A complete signal flux diagram, showing all connections between the instrumental setup and the control computer, can be found in appendix B.3 for the case of K-SPS.

and a second pair of fused-silica lenses, which produce a focus into which a mechanical chopper¹⁰ can be placed. This is optional for the XPS-based technique and the KELVIN probe, but essential for the capacitive approach. At a short distance before this focus, a fused-silica beam splitter reflects 10% of the incident power onto a power meter¹¹. A software feedback loop¹² controls and varies the position of a motorized linear translation stage¹³ that carries a variable neutral density filter¹⁴ to keep the photon flux constant across the whole spectrum. The light spot is imaged onto the sample surface by a third pair of lenses. The sample is located either in an ultrahigh-vacuum chamber in the XPS approach or in a metal box (for electric shielding) in the capacitive approach as well as in the KELVIN probe measurement. In the first two cases, the whole sample surface ($5 \times 10 \text{ mm}^2$) is illuminated, in the last case only an area of the size of the semitransparent probe, which has a diameter of 5 mm, is illuminated.

In order to obtain a realistic photon flux value at the manganite/ SrTiO_3 interface, also the transmission and reflection characteristics of all optical elements in the beam path are taken into account. Moreover, the manganite/ SrTiO_3 samples must be considered as a layered system with multiple reflections resulting in interference effects. The details on

¹⁰Thorlabs MC1000 with 5-slot wheel.

¹¹Newport 1835-C optical meter with detector UV-818.

¹²Own development, based on National Instruments LabVIEW.

¹³Pollux VT 80 by Edmund Optics.

¹⁴Thorlabs NDL-25C-4.

the calculation of the electric-field intensity at the interface are given in appendix A.1.

The above-mentioned feedback loop serving to stabilize the photon flux while a certain wavelength range is scanned works as follows:

In general, the photon flux density Φ is defined as the ratio between intensity I and photon energy $h\nu$: $\Phi = I/h\nu$. With the relation $\lambda\nu = c$, it follows that the photon flux density Φ is proportional to λI . In our experiment, we measure 10% of the light intensity that is incident on the beam splitter; we call this value I_m , while I_S denotes the desired setpoint value, which corresponds to a certain desired photon flux density. Before we perform a wavelength scan, we define a photon flux density setpoint value (which is only proportional but not equal to the real photon flux density) Φ_S :

$$\Phi_S = I_S(\lambda)K(\lambda)\lambda = \text{const} \quad (3.1)$$

where $K(\lambda)$ is a correction factor, being composed of the product of the transmissivities and/or reflectivities of all optical elements in the beam path between beam splitter and sample, and the electric-field intensity at the manganite/SrTiO₃ interface. After having set a new wavelength at the monochromator, the control software calculates a new setpoint value I_S according to equation (3.1) (note that the spectral dependences of the relevant quantities that constitute K are tabulated and accessible to the scan program). The computer-controlled translation stage, which carries the neutral density filter, is allocated to move until I_m equals I_S within a certain tolerance range.

3.2.2 X-ray photoelectron spectroscopy under additional optical illumination (X-SPS)

Photoelectron-spectroscopy-based SPV investigations are relatively rare in the literature, even though they offer several advantages compared with other SPV detection methods. These are high temporal resolution down to the ps range [Wid03] and, at least under modulated illumination, high energy resolution better than 1 meV [Tei04]. Here, the method, which was already available in the group when the present thesis started, was used as a first test to check whether a surface photovoltaic effect is measurable at all in the manganite/SrTiO₃ system.

3.2.2.1 Principle and realization

The basic principle of XPS is the creation of photoelectrons from inner core levels of atoms by the excitation of the sample surface with monochromatic x-rays. This results

in a certain kinetic-energy distribution of the emitted photoelectrons, which reflects the binding energies of the respective core levels. XPS thus provides information on the chemical composition and binding conditions of the outermost few nanometers of the sample (typically approx. 3 nm). The XP spectrum is a plot of the number of electrons counted by an energy analyzer during a certain period of time against the kinetic or binding energy of the electrons. For more details on photoelectron spectroscopy, see chapter 4, where XPS is the *main* topic.

In an SPV measurement, the sample is *additionally* illuminated by near-ultraviolet (UV) or visible (VIS) photons from the illumination setup (figure 3.5) during XPS data acquisition. Provided that the UV/VIS photons reach the interface of interest and that there is a space charge region at this interface, an SPV will be created. This results in a shift of the XP spectrum along the energy axis by the amount of the SPV.

Here, part of the LSMO XP spectrum was recorded, namely the oxygen 1s core level peak, in the dark as well as under illumination at various wavelengths to determine the light-induced energy shift of the peak. The monochromator exit slit was fully open (4 mm in width), which corresponds to a spectral width of approximately 20 nm, and the experiment was performed in the wavelength range between 280 and 780 nm at intervals of 10 nm. The power of the incident light at the sample surface was 10 mW at 450 nm, with the spot area being $5 \times 10 \text{ mm}^2$.

3.2.2.2 Results

The left diagram of figure 3.6 shows the O 1s core level line of the LSMO/STO sample in the dark and under continuous illumination at 385 nm. This wavelength corresponds to a photon energy of 3.2 eV and activates electrons across the indirect band gap E_g in STO. The predicted shift along the energy axis is clearly visible. The sign is in agreement with the downward band bending in the STO substrate (figure 3.4). The left part of figure 3.6 depicts the O 1s peak shift, as compared to the O 1s line measured in the dark, as a function of wavelength in the spectral range between 280 and 780 nm. In the super-bandgap range, this surface photovoltage spectrum corresponds to the absorption characteristics of the STO substrate with peaks at 385 nm and 330 nm, which can be attributed to the indirect and the first direct bandgap [Yac73]. In the sub-bandgap range, we observe a continuous decrease of the SPV towards lower photon energies. Since the measurement was limited in spectral resolution (10 nm), this part of the spectrum cannot be used to determine possible slope changes. The relation between SPV and illumination intensity turned out to be logarithmic (figure 3.7), as expected from theory.

In principle, the spectral resolution could be improved by using a more monochro-

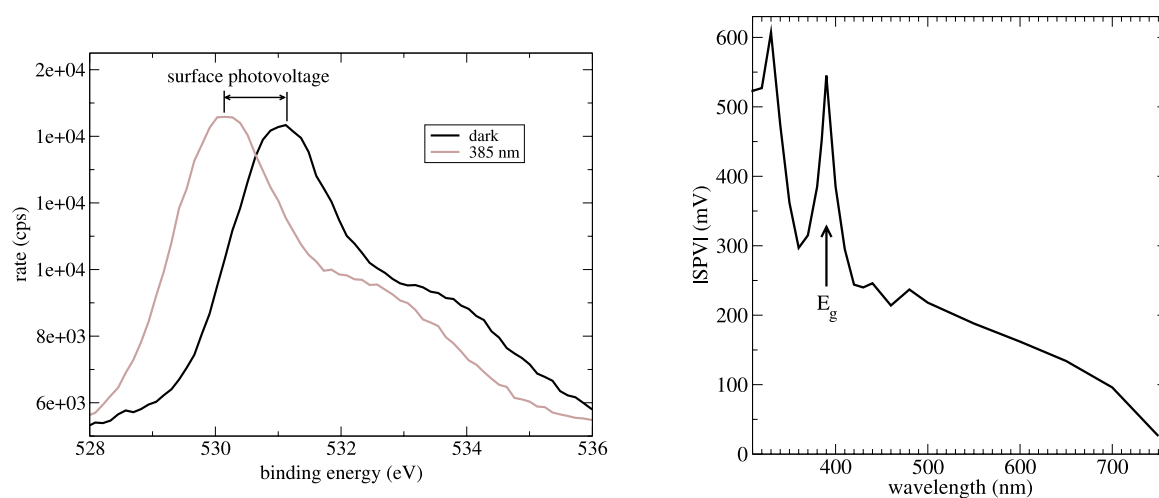


Figure 3.6: (Left) XPS O 1s core level signal of LSMO in the dark and under continuous UV illumination with a light power of 10 mW at 385 nm. The shift along the energy axis corresponds to the surface photovoltage created at the LSMO/STO interface. (Right) Spectral dependence of the SPV as detected by X-SPS under continuous illumination.

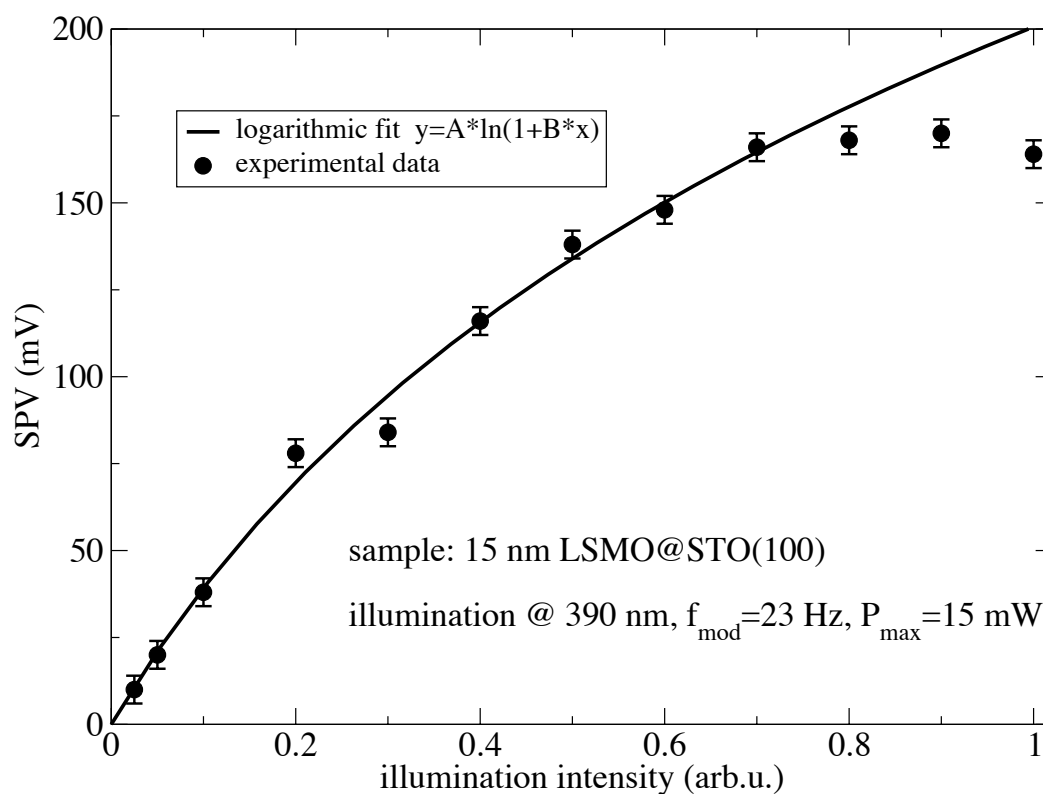


Figure 3.7: Surface photovoltage as a function of illumination intensity, as determined from the light-induced O 1s core level shifts by XPS. The expected logarithmic behavior is observable until saturation is reached. Note that these data were acquired under chopped illumination.

matic incident photon beam. This would result in a lower excitation intensity and thus a lower SPV. Under continuous illumination, the method is capable of resolving SPV values down to 10 mV. To achieve a better SPV resolution, one would have to work with modulated excitation and phase-sensitive detection [Tei04]. However, the observable SPV dramatically decreases under chopped excitation because of the slow response of STO.

Another fundamental problem of the XPS-based method is that the photons of the x-ray source themselves generate a SPV, as e.g. reported in [Hec90]. The effect becomes more pronounced, the larger the gap and thus the SCHOTTKY barrier of the material under investigation is. For conventional semiconductors, such as Si or Ge, the effect does not disturb SPV measurements. In the case of STO, however, a mixture of SPV contributions from the two different types of exciting photons arises, which cannot be easily deconvoluted¹⁵.

In summary, X-SPS showed that the manganite/SrTiO₃ interface is photovoltaically active, but with regard to quantitation of the results other SPV methods seemed to be more promising, as described in the next subsections.

3.2.3 Parallel-plate capacitor under modulated optical excitation (C-SPS)

This experimental approach is - from the instrumental point of view - very easy to implement. It is also referred to as *metal-insulator-semiconductor (MIS)* approach, since for the SPV measurement of a conventional semiconductor surface the setup is as follows: a semitransparent metal grid (*M*) is placed in proximity to the semiconductor surface (*S*) with a small gap of air or vacuum (*I*) in between. The result is a MIS capacitor structure, which is illuminated through the grid by a chopped photon beam. The SPV is measured as a voltage between the two capacitor terminals. In the present study this classical constellation was slightly modified as described in the next subsection.

3.2.3.1 Principle and realization

Within our experiment, the sample is also included in a parallel-plate capacitor geometry: The back plane of the STO substrate, which is covered with conductive silver paint and connected to ground, forms the rear plate; the manganite layer is contacted by a small dot of silver paint and forms the other plate, which is connected to ground via the current

¹⁵Experimentally, this mixture of x-ray- and visible-light-induced SPV contributions was found by the following test: Different output power settings of the x-ray source resulted in different SPV values at a *fixed* excitation power from the illumination setup.

input of a lock-in amplifier¹⁶. The STO substrate including the space charge region at the interface to the manganite film represents a dielectric spacer layer. When the sample, placed in a metal box for electrical shielding, is illuminated by chopped light, the oscillating SPV created at the photovoltaically active interface causes a displacement current to flow between the capacitor plates. This current, which is measured by the lock-in amplifier (referenced to the chopping frequency of 20 Hz), is proportional to the SPV. The energy of the exciting photons was varied from 1.6 eV (780 nm) to 3.0 eV (410 nm) in steps of 1 nm with a measurement window of 30 seconds. All spectral scans were performed starting from the low-energy end, proceeding from sub-bandgap towards super-bandgap excitation. By this, one avoids initially exciting the pronounced photovoltaic effect produced by super-bandgap illumination. This signal surpasses the trap-related signal by several orders of magnitude and has a very long relaxation time in the range of several minutes (see also [Mav78] and subsection 3.2.4). If initially excited, it would completely distort the sub-bandgap spectrum.

For this experiment, the width of the exit slit of the monochromator was set to 0.1 mm resulting in a spectral width of approximately 1 nm. The light power at the manganite/STO interface was 0.1 mW at 780 nm, which corresponds to a photon flux of $4 \times 10^{14} \text{ s}^{-1}$.

In contrast to the previously described X-SPS experiments, where only the LSMO sample was investigated, now, with C-XPS, a real *comparative* study of LSMO, LCMO, LCeMO (the latter two before and after an annealing procedure) was performed.

3.2.3.2 Results

Figure 3.9 shows the spectral dependence of the SPV as measured with the capacitive method for the LSMO/STO interface. The marked wavelength positions (and thus energies) at which the slope of the SPV spectrum changes were determined by considering both the original SPV-vs.-wavelength plot (figures 3.9(a),(c)) and its second derivative (figures 3.9(b),(d)). This approach is justified by the following considerations: If we assume the SPV-vs.-wavelength plot to consist of linear regions with different slopes, the first derivative will be a step function with step edges appearing at positions where the slope of the original curve changes. Then, the second derivative consists of delta peaks at those very positions. However, the second derivative of the measured SPV spectrum is very noisy and had to be smoothed to get the shape shown in figures 3.9(b),(d). Thus one has to be very careful in evaluating the peaks of the second derivative, as some of them originate from the smoothing procedure, especially at the low-energy end. However, the

¹⁶SR830 by Stanford Research.

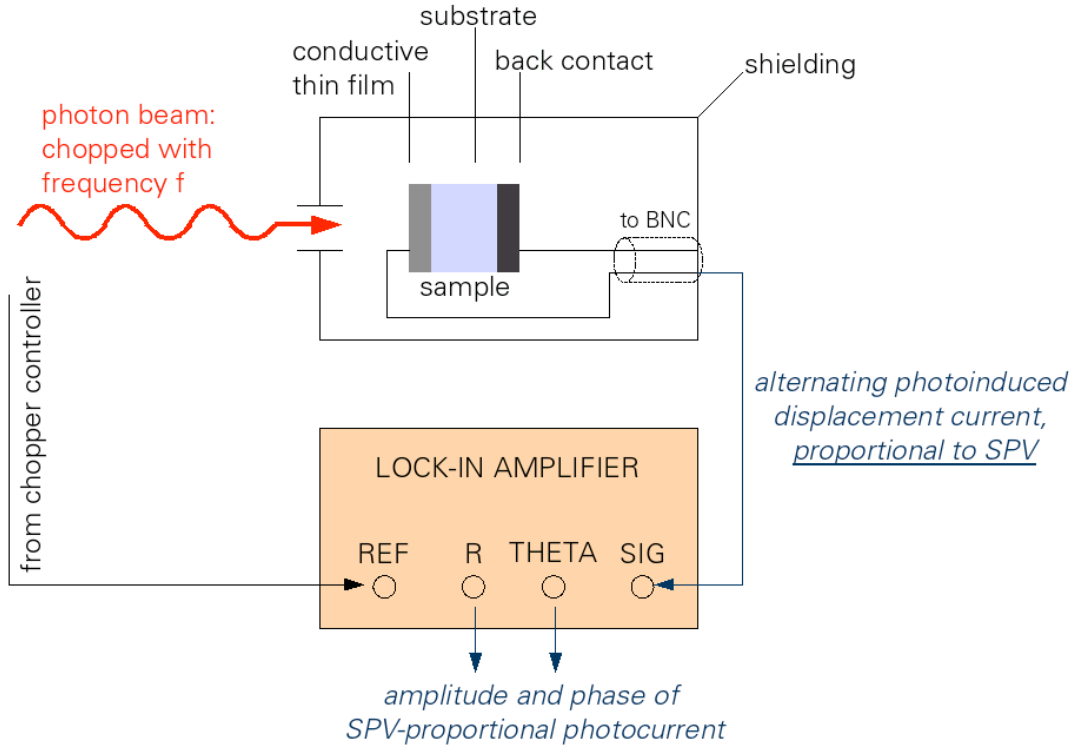


Figure 3.8: Setup for surface photovoltage measurements in parallel-plate capacitor geometry.

positions of the real slope changes can readily be derived by the comparative analysis of both the original curve and its second derivative.

The energies at which the slope of the SPV spectrum changes can be attributed to trap levels within the STO band gap. A decrease of the slope towards higher excitation energies is caused by a transition of carriers from the trap into the conduction band, followed by recombination with a hole in the valence band. This results in a decrease of the majority carrier density (holes for the case of undoped STO, see figure 3.4) and thus a decrease of the SPV signal. On the other hand, an increase of the slope can be attributed to a transition of electrons from the valence band into a trap, which increases the number of free carriers (holes) in the valence band.

The same analysis was made for the SPV spectra of the LCMO/STO and the LCeMO/STO interfaces for the as-prepared state as well as after heating at temperatures up to 670 °C in ultrahigh vacuum. For a detailed description of the annealing procedure, which was applied within the framework of our XPS investigations of the same samples, see chapter 4 and [Bey06]. In order to prevent the inflation of the main text by too many graphics, the SPV spectra of the LCMO and LCeMO films including their second derivatives and the trap level assignments were transferred to appendix B.1. Finally, all results are listed in table 3.1. In the following, we discuss the origin of the 17 detected

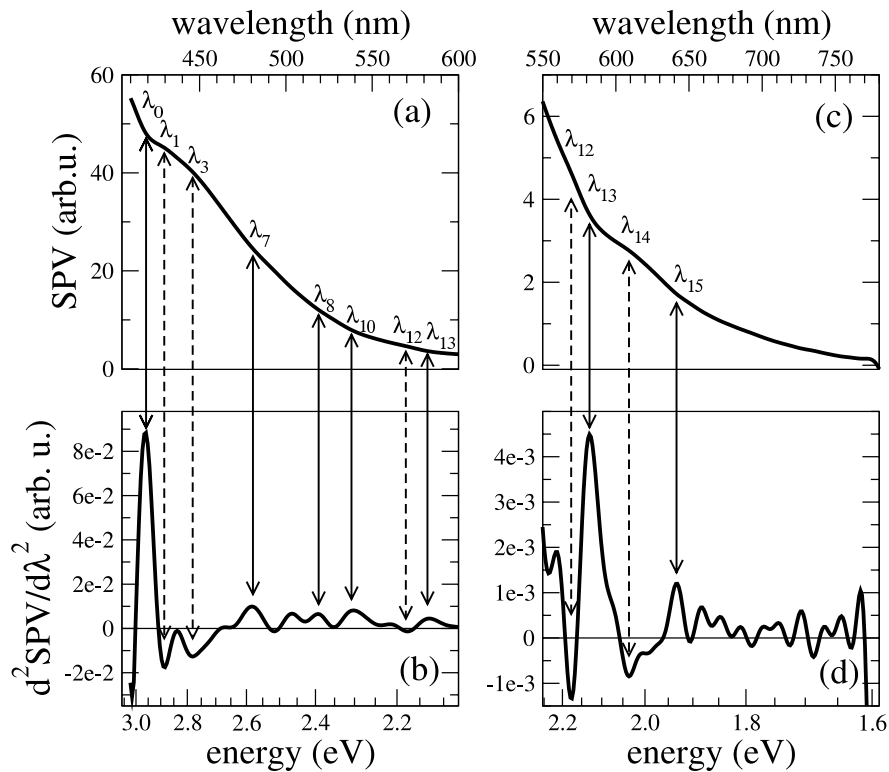


Figure 3.9: Spectral dependence of the SPV at the LSMO/STO interface as measured by C-SPS, plotted in the ranges 410-600 nm [(a), (b)] and 550-780 nm [(c), (d)]. The vertical arrows indicate slope changes which can be attributed to various interface states. For a clearer determination of the position of the slope changes, the second derivative [(b), (d)] was also considered. Solid and dashed arrows indicate positive and negative slope changes, respectively (positive and negative peaks in the 2nd derivative). The arrow indices correspond to the indexing in table 3.1. The oscillations of the 2nd derivative at the low-energy end are artificially induced by the smoothing procedure and originate from noise, so no further trap positions can be identified in this region. Note that the numbers at the SPV axis refer to the measured amplitude of the displacement current in pA. The corresponding spectra for LCMO/STO and LCeMO/STO can be found in appendix B.1.

trap levels in detail.

First, it is noted that there is clear evidence for a number of trap levels being related to the STO substrate: Level (0) can be attributed to the excitation across the STO band gap, as it is a well known phenomenon that the band gap appears smeared-out in SPV spectra. Levels (7) and (10) are probably caused by STO surface states (already present before deposition of the manganite film), which can show a distribution between 2.3 and 2.6 eV depending on the history of the sample according to the UPS measurements of [Hen78]. Also levels (12) and (13) appear in all samples and thus might also be attributed to the substrate; however, we find no correlation to levels reported in the literature. So, it is also possible that those levels are related to the manganite film without being specific

Trap level	Type of Transition	LSMO	LCMO	LCMO annealed	LCeMO	LCeMO annealed	Classification
(0) $E_V + 2.95$ eV	+	x	x	x	x	x	absorption of the indirect band gap of STO
(1) $E_C - 2.90$ eV	-	x			x		LSMO/LCeMO-specific
(2) $E_V + 2.85$ eV	+		x			x	LCMO/LCeMO(ann.) only
(3) $E_C - 2.80$ eV	-	x					LSMO-specific
(4) $E_V + 2.75$ eV	+		x				LCMO-specific
(5) $E_C - 2.70$ eV	-				x		LCeMO-specific
(6) $E_V + 2.65$ eV	+		x				LCMO-specific
(7) $E_V + 2.60$ eV	+	x	(x)	(x)	x	x	STO surface state?
(8) $E_V + 2.40$ eV	+		x				LCMO-specific
(9) $E_C - 2.35$ eV	-	x					LSMO-specific
(10) $E_V + 2.30$ eV	+	x	x	x	x	x	STO surface state [Hen78]
(11) $E_V + 2.25$ eV	+				x		LCeMO-specific
(12) $E_C - 2.20$ eV	-	x	x	(x)	x	x	STO-related?
(13) $E_V + 2.10$ eV	+	x	x	x	x	x	STO-related?
(14) $E_C - 2.00$ eV	-	x	x	x	x	x	STO absorption
(15) $E_V + 1.95$ eV	+	x					LSMO-specific
(16) $E_V + 1.75$ eV	+	(x)	x	(x)	x	x	STO vacancies [Wol73]

Table 3.1: Interface trap levels of the manganite/STO interfaces as extracted from the SPV spectra acquired with the capacitive method. The transitions can either mean the depopulation (-) or the population (+) of an interface trap level. The symbol "x" indicates that the level is observable, "(x)" means that the identification is uncertain. The levels (0)-(16) are discussed in detail in the text. E_v and E_c denote the upper valence band edge and the lower conduction band edge, respectively. Levels that appear as positive slope changes in the SPV spectrum are referred to E_v , since these traps become populated by excitation from the valence band. Similarly, levels corresponding to negative slope changes become depopulated by excitation to the conduction band and are therefore referred to E_c .

to its chemical composition. Level (14) is, with certainty, substrate-related, as it can be seen in the optical transmission spectra of both the samples as well as the pure substrate. Finally, level (15) is related to STO oxygen vacancies [Wol73]. Here, we have to point out one fundamental problem: Due to the high work function of undoped STO (approx. 5.7 eV, see also section 2.1), also the back contact is expected to constitute a SCHOTTKY contact. This means that we cannot totally exclude SPV contributions from the space charge region of the STO back. However, the light intensity reaching the rear surface is much weaker than at the interface of interest. Second, we find trap levels which only occur for one distinct manganite type: (3), (9), (15) in LSMO; (4), (6), (8) in LCMO, and (5) and (11) in LCeMO. Those levels disappear after annealing (except for LSMO, for which no annealing experiment was performed). Level (1) is observed for both LSMO and LCeMO. Last, there is level (2), which is observed in as-prepared LCMO and annealed LCeMO. It is very likely that this level is also present in LCeMO before annealing but overlaps with SPV contributions from levels at lower energies that are present before the annealing procedure, as discussed above.

The statements derived from table 3.1 are reflected in figure 3.10 in a more illustrative way. The most striking fact is that, for the LCMO/STO and the LCeMO/STO interface, the annealing dramatically changes the surface photovoltage spectra. Especially at lower excitation energies, the surface photovoltage is decisively smaller in the annealed cases, most probably caused by a lower density of interface states. Close to 3 eV excitation energy, the spectra of the annealed and as-prepared samples are similar in the LCMO/STO case; in the LCeMO/STO case the SPV is even higher for the annealed sample above 2.95 eV. This might be due to a competitive process, such as the decrease of the SPV by trap level (5) in the unannealed sample, which suppresses the SPV increase towards the super-bandgap range. Comparing the three unannealed samples, we conclude that the LCMO/STO curve is clearly different from the two others, whereas the LSMO/STO and the LCeMO/STO curves are similar in their shape, but with the LCeMO/STO sample exhibiting a higher SPV in the high-energy range of the spectrum.

As shown in table 3.1, the different behaviors of the three interfaces compared are also reflected by the fact that the number of individual states is specific to each interface. Only one interface state can be attributed to LCeMO/STO but three to LSMO/STO and LCMO/STO, respectively.

We close the discussion with some summarizing but also critical remarks:

- The key result of this C-SPS study is the map of gap states, as shown in table 3.1. Those levels were classified with respect to their possible origin and to the band with which they exchange carriers. The spectra of the different manganite films

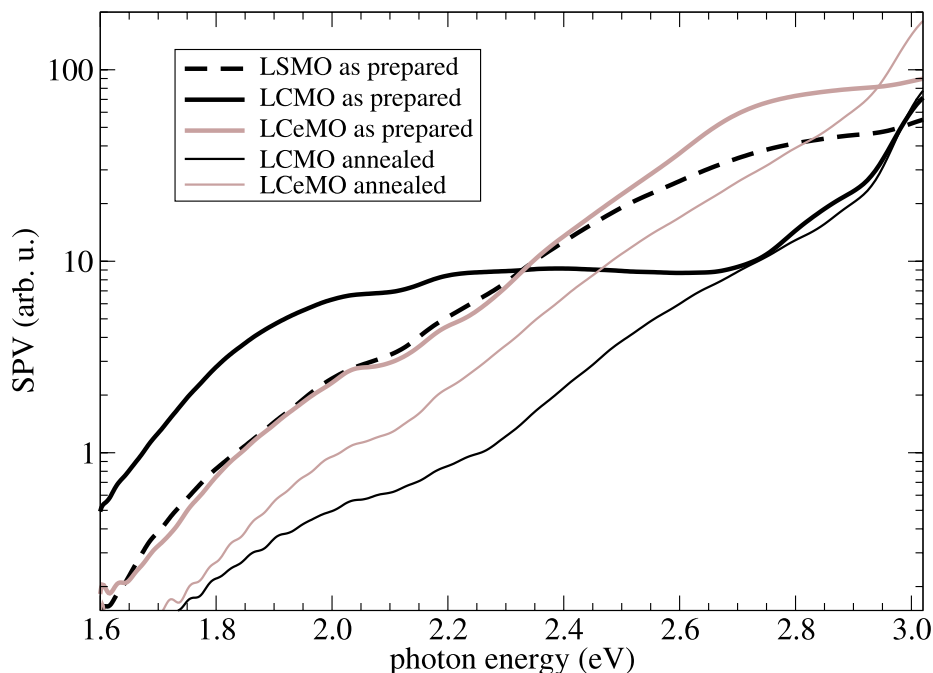


Figure 3.10: Spectral dependence of the SPV at the LSMO/STO, LCMO/STO, and LCeMO/STO interfaces, as measured by C-SPS. The LCMO/STO interface exhibits more trap levels than observed for LSMO/STO and LCeMO/STO. Annealing clearly reduces the number and density of interface trap states. Note that some distinct spectral features occur in all five curves, which suggests that they originate from the STO substrate. Also note that the SPV axis is displayed in logarithmic units.

show clear differences, which proves that the method is capable of serving as a tool for interface quality analysis.

- The question whether those levels appearing in all spectra can all be attributed to the surface of the SrTiO_3 substrate, cannot be answered within the C-SPS approach. SrTiO_3 shows very long photorelaxation times and thus belongs to the group of materials for which the KELVIN probe method, which does not need chopped illumination but can be operated under continuous illumination, is exclusively recommended for SPV measurements [Kro99]. The following subsection describes the development of such a KELVIN probe and its application for the SPV spectroscopy of the pure SrTiO_3 surface and finally answers the above question.
- It must be admitted that in many cases the determination of the *exact* energy position of a trap level is not possible. This is not a problem specific to the material systems investigated here, but a common problem of SPV spectroscopy of slowly relaxing materials. For example II-IV semiconductors such as CdS or CdSe, which were intensively studied during the early years of SPV spectroscopy, also often

showed *unsharp* slope changes. To overcome this problem, full SPV *transients* for each wavelength with sufficient dark periods in between would have to be recorded. It is clear that such a measurement scenario needs a high level of automation and is extremely time consuming.

- A last critical annotation concerns our description of the basic measurement principle of the capacitive SPV detection method. Our measurement setup corresponds to the classical MIS setup only as long as the SrTiO₃ is really dielectric. However, SrTiO₃ shows, as independent own measurements and literature data indicate, photoconductivity, to some extent even under sub-bandgap illumination. Thus, strictly speaking, we do not measure a pure displacement current but rather a photocurrent in the capacitor structure. This could be seen from the fact that also under *continuous* rather than chopped illumination a current was observed. On the other hand this does not contradict the fact that the measured signal is sensitive to the interface electronic structure.

3.2.4 The optical Kelvin probe (K-SPS)

Dating back to a work of LORD KELVIN in 1898 [Kel98], the capacitive probe, later called KELVIN probe, is one of the oldest techniques to measure surface potentials and hence work functions in a contactless manner. Concerning surface photovoltage studies, this method is, according to [Kro99], the preferred one for high-resistive and slowly relaxing samples. Within the present work it was thus straightforward to study the SrTiO₃ surface by SPV spectroscopy with a KELVIN probe (called as K-SPS in the following).

Below, the physical principle behind the technique is explained in detail first. Afterwards, the design of the KELVIN probe that was developed within the thesis especially for optical applications, such as SPV spectroscopy, is described. Finally, the SPV spectrum of the surface of an undoped SrTiO₃ single crystal is discussed in general and in connection with the C-SPS results on the manganite/SrTiO₃ heterostructures that were presented in the previous section.

3.2.4.1 Principle

In order to understand the operation principle of a capacitive probe, we first imagine the simple case of two parallel metal plates made of different materials and consequently having different work functions [figure 3.11(a)]. We also remember that (i) the work function is the energetic difference between the FERMI level and the vacuum level and that (ii) those two plates represent nothing else but a parallel-plate capacitor. If we now

electrically connect the two plates together (by a wire for example), the FERMI levels will be equilibrated, which means that, in terms of an energy band scheme, a potential drop in the vacuum level is generated [figure 3.11(b)]. This potential drop is referred to as *contact potential difference (CPD)* and is equal to the difference of the work functions of the two metals. For a complete understanding we may add that the equilibration of the FERMI levels is reached by a current of electrons from the metal with the lower work function to the metal with the higher work function. This finally results in the charging of the capacitor and, as a consequence of the potential drop, an electrical field in the gap between the metal plates.

The key idea of LORD KELVIN was to *nullify* the CPD by biasing one plate with an external voltage of the same magnitude as the CPD but of opposite sign [figure 3.11(c)]. In other words, the external bias voltage should be adjusted such that the capacitor gets discharged.

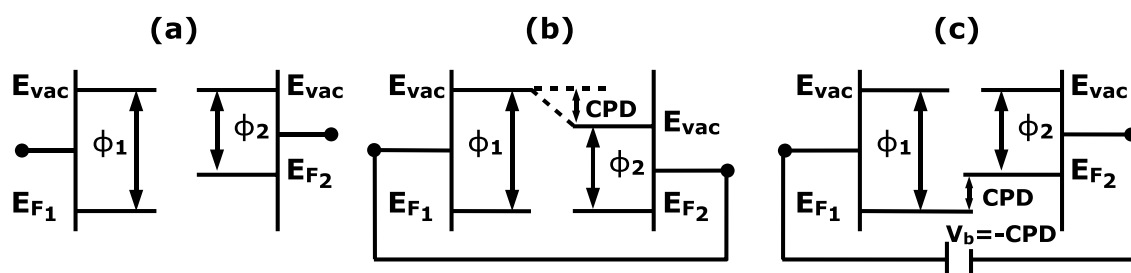


Figure 3.11: Energy level diagrams of two different metals with work functions ϕ_1 and ϕ_2 : In case (a) both metals, which are assumed to be plates and form a capacitor, are isolated. If they are connected, as in part (b), the FERMI levels E_{F_1} and E_{F_2} align with the consequence that a potential drop, the so-called contact potential difference (CPD), in the local vacuum level E_{vac} is generated. The vacuum level is flattened by a bias voltage V_b opposite to the CPD, as shown in part (c).

How can this idea be transferred to a practical measurement method, i.e., how can we detect *that* the capacitor is in the discharged state? The solution to this problem was first proposed by ZISMAN [Zis32] and, still being the basis of modern KELVIN probes, consists of a periodical vibration of one of the two capacitor plates perpendicularly to the surface of the other plate¹⁷. Typically, one plate is made of a material of known work function (also called reference electrode) and the other one is formed by the material under investigation, with the first being vibrated and the latter remaining fixed. For a further understanding of the method, we have to review the basic equations describing the parallel-plate capacitor.

¹⁷In modern KELVIN probes the vibration is either performed by piezoelectric excitation (e.g. [Mal72, Dix73, Bes76, Ger87, Ger89, Had95, Sch97]) or by electromagnetic excitation (voice coil, see e.g. [Höl74, Har84, Bai89, Sur96]). Apart from that, within the development of scanning probe microscopy, the method of KELVIN probe force microscopy (KPFM) has spread. There, one plate is replaced by a tip on a cantilever, which makes work function measurements with high spatial resolution possible [Zer05].

If the general relation between capacitance C , stored charge Q , and voltage drop U

$$C = \frac{Q}{U} \quad (3.2)$$

is combined with the equation

$$C = \epsilon\epsilon_0 \frac{A}{d} \quad , \quad (3.3)$$

which is valid only for the parallel-plate geometry with A being the plate area, d the distance between the two plates, ϵ_0 the permittivity of vacuum, and ϵ the dielectric constant of the dielectric between the two plates, we get the following relation for the charge Q :

$$Q = \epsilon\epsilon_0 \frac{AU}{d} \quad . \quad (3.4)$$

If the distance d is changed periodically, for instance in a sinusoidal way:

$$d = d_0 + d_1 \sin(\omega t) \quad , \quad (3.5)$$

the charge Q becomes:

$$Q = \epsilon\epsilon_0 \frac{AU}{d_0 + d_1 \sin(\omega t)} \quad . \quad (3.6)$$

To keep the voltage U , which is the sum of the external voltage U_{ext} and the contact potential difference U_{CPD} , constant while the distance d changes over time, a certain amount of charge dQ must be transferred between the plates. Thus we expect the following alternating (but not purely sinusoidal) current I to flow:

$$I = \frac{dQ}{dt} = -\frac{\epsilon\epsilon_0 AU d_1 \omega \cos(\omega t)}{[d_0 + d_1 \sin(\omega t)]^2} \quad . \quad (3.7)$$

From this relation we can learn the following: Being aware of the fact that the voltage U is, in a real KELVIN probe experiment, the sum of the CPD (between reference electrode and unknown sample surface) and the (nullifying) bias voltage, we realize that establishing a feedback loop that measures the current I and adjusts the external bias voltage U_{ext} in such a way that I becomes zero is an appropriate method to reach the goal of the discharged capacitor where $U_{ext} = -U_{CPD}$.

We close this theoretical discussion of the KELVIN probe technique with some further comments:

- In the experiment not the total current is typically measured but rather the amplitude of its first or second harmonic (by a lock-in amplifier). Expanding the denominator of equation (3.7) into a power series and performing several rearrange-

ments, one ends up with the following terms for the first and second harmonic I_ω and $I_{2\omega}$ of I :

$$I_\omega = -\epsilon\epsilon_0 AU\omega \frac{d_1}{d_0^2} \cos(\omega t) \sum_{n=0}^{\infty} \left(\frac{1}{2} \frac{d_1}{d_0}\right)^{2n} \frac{(2n+1)!}{n!(n+1)!} \quad (3.8)$$

$$I_{2\omega} = 2\epsilon\epsilon_0 AU\omega \frac{d_1}{d_0^2} \sin(2\omega t) \sum_{n=0}^{\infty} \left(\frac{1}{2} \frac{d_1}{d_0}\right)^{2n+1} \frac{(2n+2)!}{n!(n+2)!} \quad ; \quad (3.9)$$

for the whole calculation see appendix B.2.1. Both harmonics are proportional to U and thus can be used as the input to an integrating controller, which is the essential part of the above-mentioned feedback loop. Using the second harmonic as the input to the control loop offers the advantage that the circuit becomes less sensitive to parasitic pick-up of signals that originate from the vibration excitation source (e.g., from a shaker piezo). Such incoupling can heavily disturb an experiment if the first harmonic is used. On the other hand, in most experimental cases the first harmonic provides the higher signal amplitude compared with the second harmonic.

- Putting in realistic numbers into equations (3.7), (3.8), and (3.9) shows that the current I is very small, typically in the pico- or even femtoampere range (see appendix B.2.2). This makes the current measurement vulnerable to several sources of noise and error signals. Careful coaxial wiring, shielding, and current-to-voltage conversion as close to the probe as possible are thus essential.
- Measurements of the *absolute* value of the work function are complicated, since for that purpose the work function of the reference electrode has to be known exactly, which can be practically achieved only in ultrahigh vacuum. Furthermore stray capacitance is a serious problem for exact work function measurements. Theoretical descriptions and correction algorithms have been proposed: [Sur70, Had95].
- Fortunately, surface photovoltage measurements are *differential* measurements, so that various error sources do not play any role. Since the SPV is the difference of the work functions of a material in the dark and under illumination, it is also equal to the CPD difference between the two cases (provided that the probe does not show any photovoltaic activity, which is certainly true for a pure metal).

3.2.4.2 Realization

Within the thesis a home-built KELVIN probe setup for operation in air was planned, constructed, and finally used. The main demands to the setup were the following:

- easy optical access to the sample surface, since SPV measurements would be the main application of the setup,
- high stability and therefore suitability for long-term operation, since the acquisition of SPV spectra or transients takes several hours,
- inexpensive.

The whole *mechanical* construction is placed in a grounded metal box, which serves for both electrical shielding and stray light protection. The box has one entrance slit for coupling light from the illumination setup onto the sample surface, and is mounted on two posts that fit in commercial post holders, which allows easy height adjustment. The probe and sample holders are attached to the base plate of the box (figure 3.12). The sample holder consists of two parts: (i) a linear translation stage for sample approach towards the probe and (ii) an insulating polyvinylchloride block, to which the sample is glued by conductive silver paste (at the same time this makes the electrical back contact). The probe holder is a more sophisticated construction: A circular piezoelectric multimorph disk with a center hole¹⁸ is clamped inside a metal housing in order to prevent cross coupling of the piezo excitation voltage. The piezo disk carries an aluminum hollow cylinder, whose outer diameter is slightly tapered. The probe, which consists of a round quartz window¹⁹ with a semitransparent metal layer evaporated onto it, is glued to the narrow end of the cylinder. The metal layer consists of a 2-nm-thick chromium film and a 8-nm-thick gold film, which serves as the inert reference electrode. In the experiment the sample thus can be illuminated *through* the probe. Furthermore, the whole unit carrying the piezo and the probe can be tilted around two orthogonal axes by micrometer screws to achieve a parallel alignment of the probe and the sample surfaces²⁰.

¹⁸Piezoelectric disk bender with center bore, model CBM 100/50-10/120M, by Piezomechanik GmbH. The maximal center displacement is 250 μm at an applied voltage of 100 V. The resonance frequency is 3 kHz.

¹⁹UV window, model 45463, by Edmund Optics (5 mm diameter, 1 mm thickness).

²⁰For the alignment procedure, a HeNe laser beam hits the sample surface at near-normal incidence. The reflections from both the probe and the sample are monitored on a screen at a large distance. As long as the two surfaces are not parallel, several reflection spots are visible. By adjusting the two micrometer screws of the probe mount, the spots can be superimposed on each other and consequently made to interfere. As soon as interference is observed, one can be certain that the probe and the sample are aligned parallel.

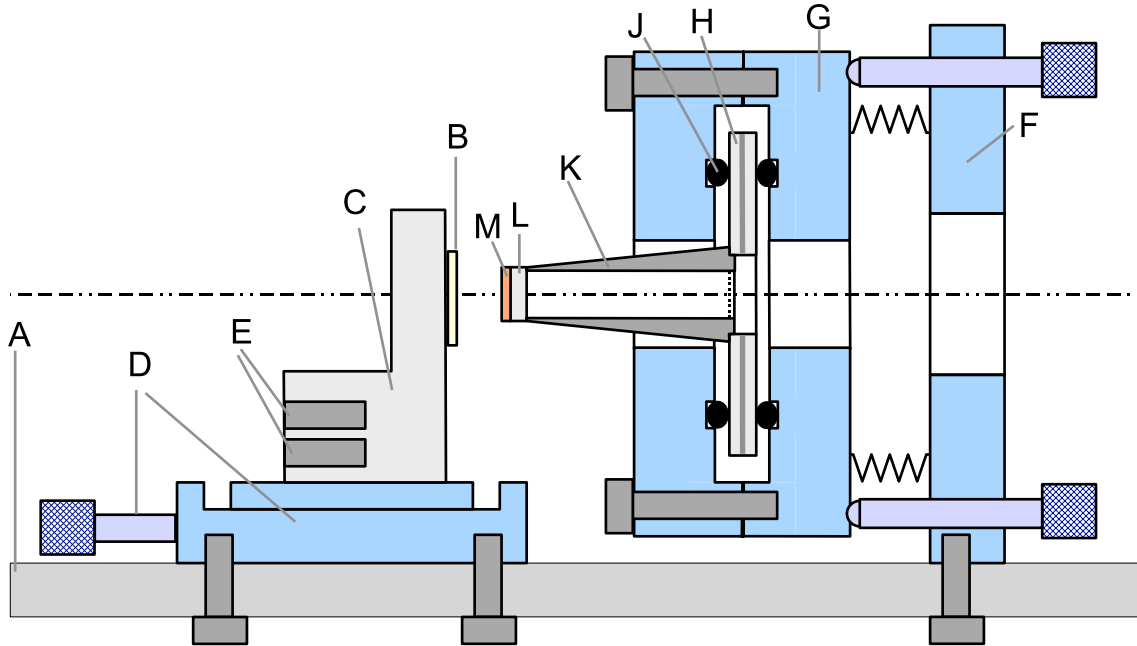


Figure 3.12: Mechanical parts of the KELVIN probe: (A) base plate; (B) sample fixed on a (C) block with several (E) bores for optional heating cartridges and temperature sensors; (D) translation stage for sample movement; parts (F) and (G) represent the probe mount, with (F) being fixed and (G) tiltable in two directions; (H) piezoelectric multimorph being clamped between (J) rubber rings within the metallic housing (G) for efficient decoupling of the piezo excitation signal from the probe current; (K) hollow cylinder glued to the piezo, carrying the (L) quartz window with the (M) metal film that serves as the probe. Note that the sketch, which is mainly a cross section, is not to scale. In a true cross section only one of the two probe adjustment screws would be visible since they are placed at diagonal corners of part (F).

The *electrical* signal flow can be described as follows: For piezo excitation the internal sine generator of a lock-in amplifier²¹ delivers a voltage with an rms amplitude of 1 V and a frequency of 175 Hz, which is amplified by a home-built high-voltage amplifier (gain=10) and fed to the inner contact of the piezo disk. The current I generated in the vibrating capacitor structure (see section 3.2.4.1) is sent from the probe to a home-built current-to-voltage converter (preamplifier) having a transimpedance of 100 M Ω . The output voltage of the preamplifier is fed into the lock-in amplifier, which extracts the in-phase signal amplitude ("X") of the first harmonic (denoted by I_ω in section 3.2.4.1). This "X signal" is fed back to the sample back contact via a home-built integrator ("I controller") in order to nullify the current I . The integrator output voltage then equals $-U_{CPD}$. This so-called KELVIN signal is recorded by the control computer after analog-to-digital conversion by a multifunction data acquisition board. Figure 3.13 depicts the main features of the electrical configuration of the KELVIN probe, while the complete signal flow diagram of the experiment can be found in appendix B.3.

²¹SR830 by Stanford Research, the same model as used in C-SPS.

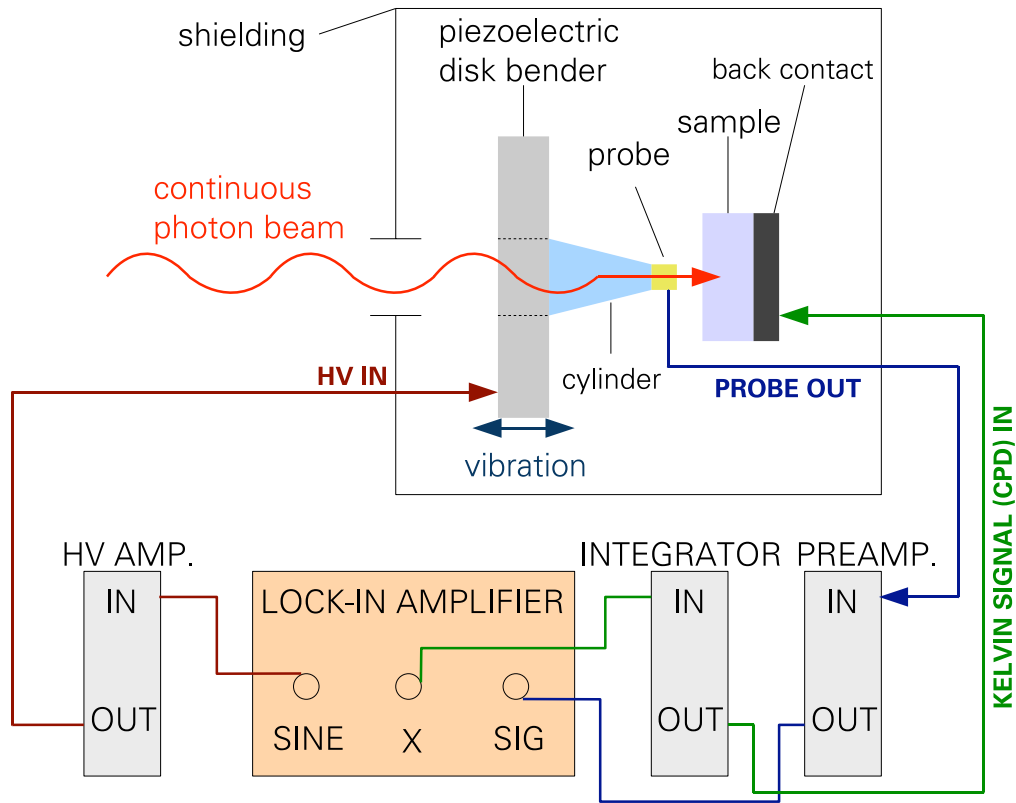


Figure 3.13: Overview of the electric circuitry for KELVIN probe measurements: The piezoelectric disk bender is excited by a sinusoidal high voltage, while the first harmonic of the preamplified probe current is analyzed by a lock-in amplifier. The in-phase part of this first harmonic serves as input signal for the integrating controller, whose output is fed back to the sample back contact in order to nullify the probe current. This voltage then corresponds to the opposite of the contact potential difference between probe and sample surface. A more complete signal flow diagram can be found in appendix B.3. For SPV studies the photons from the illumination setup are coupled through the probe onto the sample.

Before continuing with the report on SPV measurements performed with this instrument, we list some further comments and details on the construction and operation of the setup:

- The typical probe-to-sample spacing (d_0) was around $100 \mu\text{m}$, whereas the oscillation amplitude (d_1) was $25 \mu\text{m}$. For the piezoelectric multimorph used here, this displacement could be realized by a relatively low excitation voltage of approximately 10 V, which is favorable in terms of as little disturbance of the probe current measurement as possible. Another advantage of the large elongation of the piezo disk is that it can be operated off resonance. Resonant operation typically suffers from long-term stability problems, which need further sophisticated electronic circuitry to be overcome [Dix73, Sch97]. In our case the excitation is stable over several days.

- The time constants of the lock-in amplifier and of the integrator were set to 30 ms and 1 ms, respectively.
- The polyvinylchloride sample holder can be replaced by a heatable copper sample holder for temperature-dependent SPV measurements, especially SPV-DLTS (deep level transient spectroscopy) [Läg99]. This option was not used within the framework of the present investigations, but is ready for operation for later users. The additional electronic components necessary for temperature control are also included in the complete signal flow diagram in appendix B.3.
- The surface photovoltage *spectrum* of the pure SrTiO₃ surface was acquired with the same illumination and wavelength scan parameters as described for the C-SPS method in section 3.2.3.1 with a few changes: First, the illumination is now continuous and not modulated; second, the illuminated area corresponds not to the whole sample area but only to the probe area; and third, the spectral transmission of the semitransparent probe is additionally accounted for by the photon flux control procedure.

3.2.4.3 Results

Figure 3.14 shows the SPV spectrum of a pure undoped SrTiO₃ sample as it is assumed to be before the deposition of a manganite film. Slope changes are found at five spectral positions. As those positions appear sharper than in C-SPS, it was not necessary to use the second derivative as an additional indicator for the slope change positions. Table 3.2 summarizes the energies of the trap states, their possible origins, and their relation to trap states found with C-SPS (table 3.1).

Let us discuss the five detected energy levels in detail: Level (0) is clearly related to excitation across the band gap. As already observed in C-SPS, the SPV rises already below the very gap energy (3.2 eV), which is a common phenomenon in SPV experiments. Levels (3) and (4) coincide with former levels (14) and (16) found in the C-SPS analysis, which there were assumed to stem from the SrTiO₃ substrate.

However, not all levels from C-SPS that were tentatively assigned to the SrTiO₃ surface can be directly found in the K-SPS analysis of the pure SrTiO₃ surface. One possible reason is that those levels may have been induced by the manganite film independently of the type of the doping ion and thus appear in each of the spectra.

On the other hand, the K-SPS analysis reveals also two levels that are missing in the C-SPS spectra, namely levels (1) and (2). Level (1), located 2.45 eV below the conduction band, can be assigned to oxygen vacancies (see section 2.1.4, esp. the comments on

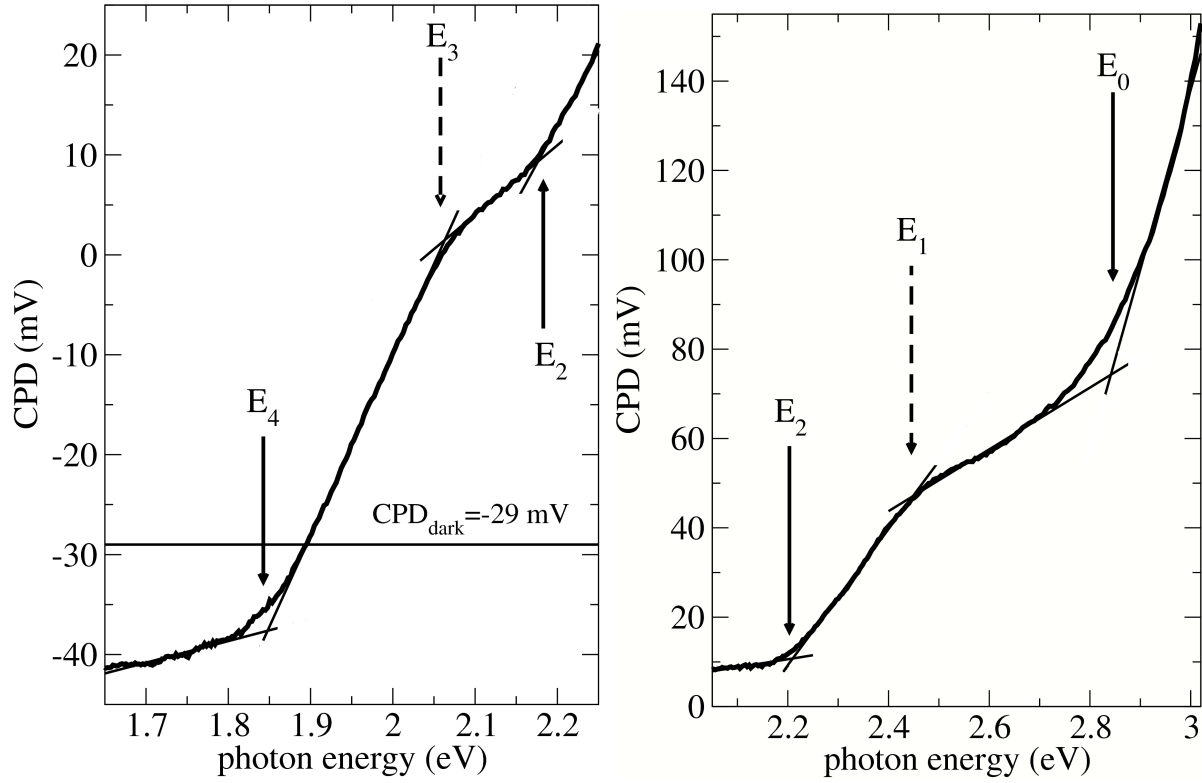


Figure 3.14: SPV spectrum of the pure undoped SrTiO₃ surface acquired with the KELVIN probe under continuous illumination. For better visibility, the spectrum was divided into two (overlapping) parts. Points of slope change are identified with the crossings of straight lines fitted to sections of the spectrum having constant slopes. Solid and dashed arrows indicate positive and negative slope changes, respectively. Five different trap states were detected, for further details see table 3.2.

Trap level	Type of Transition	Corresponding Level from C-SPS	Classification
(0) $E_v + 2.85$ eV	+	(0)	absorption across the indirect gap
(1) $E_c - 2.45$ eV	-	not present	oxygen vacancies
(2) $E_v + 2.20$ eV	+	(13) (?)	surface state (?)
(3) $E_c - 2.05$ eV	-	(14)	bulk absorption
(4) $E_v + 1.85$ eV	+	(16)	surface vacancies

Table 3.2: Trap levels of a SrTiO₃ sample, as extracted from the SPV spectra acquired with the KELVIN probe. The transitions can either mean the depopulation (-) or the population (+) of a trap level. E_v and E_c denote the upper valence band edge and the lower conduction band edge, respectively. Levels that appear as positive slope changes in the SPV spectrum are referred to E_v , since these traps become populated by excitation from the valence band. Similarly, levels corresponding to negative slope changes become depopulated by excitation to the conduction band and are therefore referred to E_c . For levels (1) and (2) no corresponding levels from the C-SPS measurements can be found. Possible reasons for the discrepancy are discussed in the text.

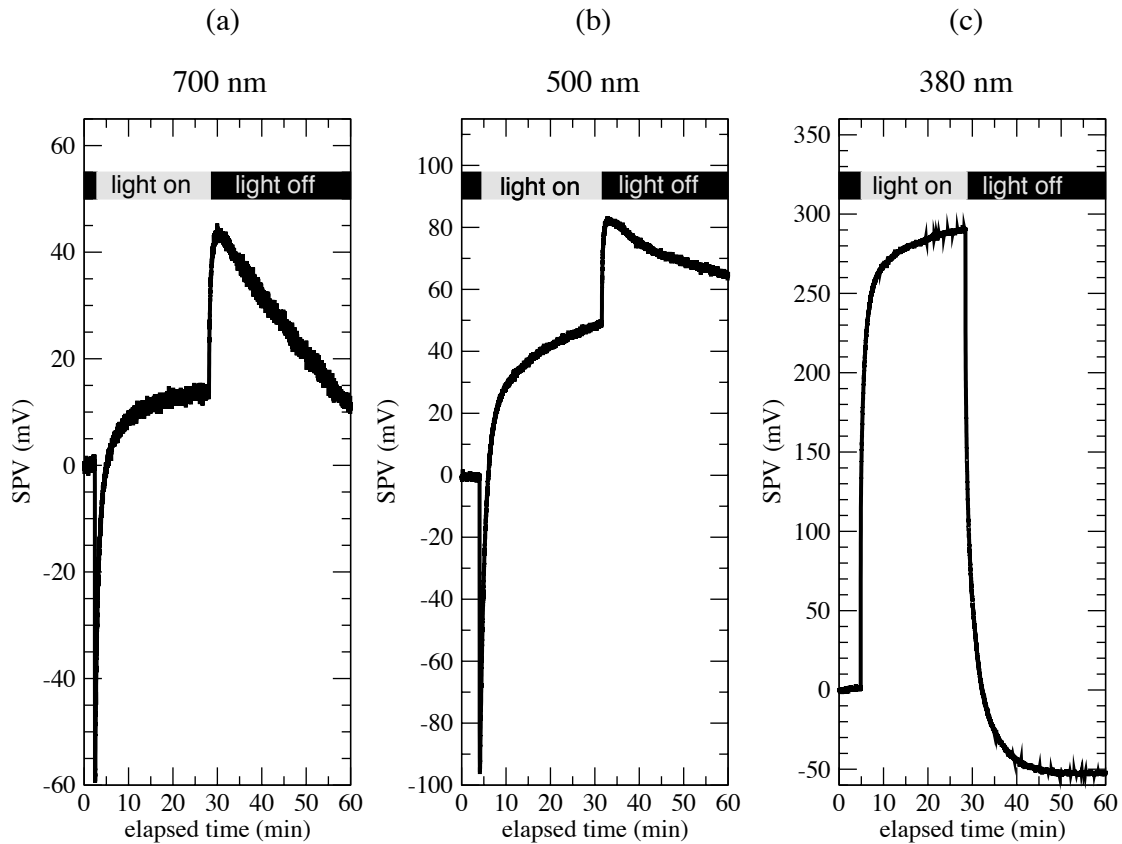


Figure 3.15: Surface photovoltage transients of SrTiO₃ for sub-bandgap illumination at 700 nm (a) and 500 nm (b) and for super-bandgap illumination at 380 nm (c). The light is switched on approximately 3 minutes after the acquisition has started and switched off after approximately 30 minutes. For the sub-bandgap cases, the transients consist of two different contributions due to at least two trap states within the band gap, with one state relaxing faster than the other. The different signs of the two contributions indicate that one of the two trap states exchanges carriers with the conduction band, while the other trap state "communicates" with the valence band. Differently from the illumination parameters for the previously described spectral SPV measurements, the illumination intensity for these transient measurements was higher: around 1 mW for the two sub-bandgap cases and around 0.5 mW for the super-bandgap case.

the "green luminescence" of SrTiO₃) and is [similar to levels (3) and (4)] a bulk effect. The question why this level, which is the result of a well-known effect in SrTiO₃, is not observed in C-SPS spectra might be answered by the fact that C-SPS uses modulated illumination. This in turn means that contributions of trap states with large time constants are suppressed. The assignment of level (2) is not that straightforward. It might correspond to the C-SPS level (13) if we take into account that the determination of the energy positions are subject to an uncertainty of around 0.1 eV.

After the discussion of the trap states that could be extracted from the K-SPS measurement of the SrTiO₃ surface, some further important considerations should be pointed out:

- If we reexamine figure 3.14, we notice that the CPD values are less than the dark value below approximately 1.9 eV but larger than the dark value above 1.9 eV. In other words, the SPV, which is the difference between the CPD values in the dark and under illumination, changes its sign. This can be understood by studying the transient behavior of the SPV, as shown in figure 3.15. There, the SPV is plotted against time, with the sample being in the dark for around the first 3 minutes until light of a fixed wavelength is switched on (and kept on) for around 30 minutes and finally switched off again. Considering the transients in the sub-bandgap range (here exemplarily shown for 700 nm and 500 nm), it is obvious that the curves contain two different SPV contributions of opposite sign with different time constants. With the knowledge about this individual shape of the sub-bandgap transients we must review the SPV spectra from figure 3.14 critically. First, the sign change of the SPV at 1.9 eV can be explained by the presence of two components in the transient. Second, the whole spectrum must be seen as kind of a convolution between real spectral changes and the shape of the transient. Thus the information content of the simple SPV spectrum appears rather limited.
- In addition, the SPV transients taken with super-bandgap excitation verify the assumption that undoped SrTiO₃ behaves as a p-type semiconductor. Transients that were taken on Nb-doped SrTiO₃, which is definitely n-type, show similar super-bandgap behavior but with the opposite sign (graphs not shown here).
- Moreover, it is noted that the super-bandgap transients for neither undoped nor Nb-doped SrTiO₃ can be fit by a single exponential curve. Thus a quantitative evaluation of the transients in order to extract time constants or activation energies is not straightforward. The same statement is, even more obviously, true for the sub-bandgap transients.
- The problem of the very slow photorelaxation that distorts the SPV spectrum, can be overcome by means of a highly automated long-term experiment in which the SPV is recorded as a function of both wavelength and time. In other words, it would be necessary to acquire full transients in the relevant wavelength range with sufficient wavelength resolution and appropriate periods of darkness between the illumination cycles.

- A second key problem, apart from the slow relaxation, is the impossibility to fabricate an ohmic back contact due to the high work function of undoped SrTiO₃. For such a case the capacitor model must be extended to include two capacitors with different dielectrics in their gaps, acting in series. Mathematically, this would imply that in equations (3.6)-(3.9) d_0 has to be substituted by $\frac{\epsilon}{\epsilon_s}d_s + d_0$ with ϵ_s and d_s being the dielectric constant and the thickness of the SrTiO₃ sample. However, in our case the SrTiO₃ capacitor changes its dielectric behavior upon illumination due to photoinduced carrier generation. Hence, also such a refined model fails, but for the determination of spectral *variations* in the SPV the method is still applicable.
- While the pure *existence* of a rectifying back contact may appear tolerable, the fact that this contact is also *illuminated* is more problematic. Thus defect-related trapping specific to this back interface, which in our case is the interface between unpolished (and thus probably even more defective) SrTiO₃ and conductive silver paste, might also become visible in the SPV spectrum. On the other hand, in C-SPS the back contact is also illuminated. Thus, within the framework of a *comparative* investigation, illuminating also the back contact is in fact a necessary prerequisite. Furthermore, as already mentioned, SPV transients of opaque Nb-doped SrTiO₃, in which case the strong absorption prevents the back contact from being illuminated, show a similar behavior without any specific differences. In particular, the same two-component structure in the sub-bandgap transients is observed.

3.3 Summary and discussion

Chapter 3 reported on the investigation of the distribution of electronic trap states at three different lanthanum manganite/SrTiO₃ interfaces (LSMO/STO, LCMO/STO, LCeMO/STO) and at the pure SrTiO₃ surface. The interfaces were studied by three different implementations of the surface photovoltage spectroscopy (SPS) technique: x-ray photoelectron spectroscopy under additional optical excitation (X-SPS), the capacitive detection of the surface photovoltage (C-SPS), and the KELVIN probe technique under illumination (K-SPS). The SPS technique was chosen for three reasons:

1. It is a contactless and thus nondestructive method.
2. Classical electrical semiconductor characterization methods fail for high-resistance samples such as SrTiO₃.

3. Systematic studies of complex-oxide interfaces with this method seem to be rare so far.

Let us first comparatively evaluate the three different *implementations* of SPS: In the present work, X-SPS served for a first test of the photovoltaic response of the LSMO/STO interface. For in-depth studies this method is not suitable, because the photons both from the x-ray source and from the illumination setup contribute to the SPV signal. Consequently, real sub-bandgap SPV studies are not possible. With C-SPS the distribution of gap states at the three different manganite/SrTiO₃ interfaces could be analyzed. The experiment is easy to implement, but suffers from the drawback that one can only work with modulated optical excitation, which means that SPV contributions from slowly relaxing electronic states are inevitably suppressed and might be lost in the spectrum. Furthermore, a photocurrent rather than the true SPV value is measured. Those problems were partially overcome in the KELVIN probe SPS experiment (K-SPS), which was, within the present thesis, used to examine the electronic structure of the SrTiO₃ surface before film deposition. This technique needs more sophisticated construction work but is advantageous in that it provides absolute SPV values and allows the monitoring of slow states, as it can be operated under continuous illumination.

Second, we discuss the results on the different *material systems* under study: A variety of electronic states localized within the band gap of the SrTiO₃ substrate were found for all three manganite/SrTiO₃ interfaces. Part of the states could be definitely assigned to the SrTiO₃ substrate, either to its surface or to its bulk. Other states are clearly specific to the individual manganite compound, with the LCMO spectrum being the most distinct one. It exhibits one trap state producing a comparatively high SPV signal. It was also shown that annealing dramatically reduces the sub-bandgap SPV, which can be interpreted in terms of a reduction in the number and density of interface states. However, also the modified optical properties of the substrate resulting from annealing might be a reason for the lower SPV signal.

For a further establishment of the SPS method for the interface analysis of complex oxides, the author would like to make two important recommendations: First, a comparative study of a broader set of slightly differently prepared manganite samples is absolutely necessary in order to collect more experience in the interpretation of the SPV spectra. Especially, it would be extremely useful to have a *real reference substrate*, i.e., a substrate which is subjected to the same temperatures and oxygen partial pressures as the PLD-grown film during its preparation. Second, the long-term acquisition of the SPV as a function of both wavelength and time by means of the K-SPS technique appears to be the most promising approach for obtaining a maximum of information on the – without

doubt – rich but also very complex dynamics of the photoresponse behavior of the system. However this would need also a maximum of measurement time and is thus not useful as a *quick check* of interface quality.

Finally, the SPV studies reported in this work can be seen as preliminary investigations that have established the experimental preconditions and collected experiences for more extended future studies of oxidic interfaces by surface photovoltage spectroscopy and possibly by other photo-assisted techniques, e.g. photoconductivity investigations, or by locally resolved SPV studies with KELVIN probe force microscopy. The latter method appears to be very promising within the context of exploring possible intrinsic phase separation phenomena in the manganites.

4 Photoelectron spectroscopy of lanthanum manganite thin-film surfaces

This chapter reports on a systematic photoelectron spectroscopy study of the manganese valence and doping type of a hole-doped $\text{La}_{0.7}\text{Ca}_{0.3}\text{MnO}_3$ (LCMO) thin film and a nominally electron-doped $\text{La}_{0.7}\text{Ce}_{0.3}\text{MnO}_3$ (LCeMO) thin film under reversible variation of the oxygen content. This investigation was performed as a clarifying contribution to the ongoing debate whether electron doping of LaMnO_3 is possible at all. It is shown that through exact tuning of the oxygen content the electron-doped state can indeed be achieved. The as-prepared state of LCeMO is characterized by overoxygenation and shows the behavior of a hole-doped compound. The chapter starts with a short general introduction to the technique of photoelectron spectroscopy followed by a description of the setup used in this work.

4.1 Fundamentals

Since *photoelectron spectroscopy* (PES), also referred to as *photoemission spectroscopy*, is a widely used technique for analyzing the electronic structure of solids (especially surfaces) and many review books and articles on the topic exist, only the most important facts are summarized below. The text is based on several comprehensive publications: [Vic97, Lüt98, Bri03, Hüf05].

4.1.1 The principle of photoelectron spectroscopy

4.1.1.1 The photoelectric effect and its physical information content

The basic physical principle behind all photoemission experiments is known as *photoelectric effect*: When a surface of a solid is illuminated by photons of sufficiently high energy $h\nu$, it will emit electrons, so-called *photoelectrons*. These electrons are released from either a core level or the valence band by complete energy transfer from the incident photons¹. The kinetic energy E_{kin} of the photoelectron bears information on the binding energy

¹It has to be noted that after the actual photoemission process the atom might reorganize. An electron can relax from a higher energy state to the vacant core hole. The excess energy which then accumulates can be transferred to an outer electron, which is also ejected (AUGER electron), or to a photon (x-ray fluorescence).

E_B (referred to the FERMI level) of the respective core level according to the following relation:

$$E_B = h\nu - E_{kin} - \phi_s \quad , \quad (4.1)$$

where ϕ_s is the work function of the sample material, i.e., the energetic difference between the FERMI level and the vacuum level. In a realistic photoemission experiment one obtains photoelectrons with a certain *distribution* of kinetic energies and, after conversion according to equation (4.1), of binding energies. In other words, a *photoelectron spectrum* is a plot of the number of counted electrons versus the electron energy. Discrete peaks reflect core level binding energies, which are specific to each chemical element. The exact core level binding energy for a certain element additionally slightly varies according to the valence state, the binding conditions, exchange interactions, screening, or some other effects, because, strictly speaking, photoemission is a complicated many-body process. Thus, after careful spectral evaluation of photoemission data with respect to peak positions and spectral features not only a simple chemical analysis may be performed but a refined picture of the electronic structure of the solid can be gained. The discrete peaks are furthermore overlaid by the signals of inelastically scattered electrons, the so-called *inelastic background*, which has to be subtracted before any spectrum is interpreted² (see also figure 4.5).

Another source of information is the *angular* distribution of the emitted electrons, which allows the reconstruction of the bulk and surface electronic band structure due to considerations on momentum conservation and is known as *angle-resolved photoelectron spectroscopy* (ARPES). Moreover, depth profiling of the chemical composition is possible. The experiments within the present thesis were performed at a fixed electron collection angle; thus we refrain from further treating ARPES here.

Another important point to be mentioned is that, due to the limited inelastic mean free path (IMFP) of electrons in solids, the information depth of PES is limited. For inorganic solids as investigated here, the detected photoelectrons stem from the approximately outermost 3 nm of the sample. Thus, PES is a surface-sensitive technique and one has to be cautious in generalizing the results with respect to the bulk.

²There are several background correction algorithms available, among them the simple linear correction or the more refined algorithms according to SHIRLEY [Shi72], which is mainly used in this work, and TOUGAARD [Tou96].

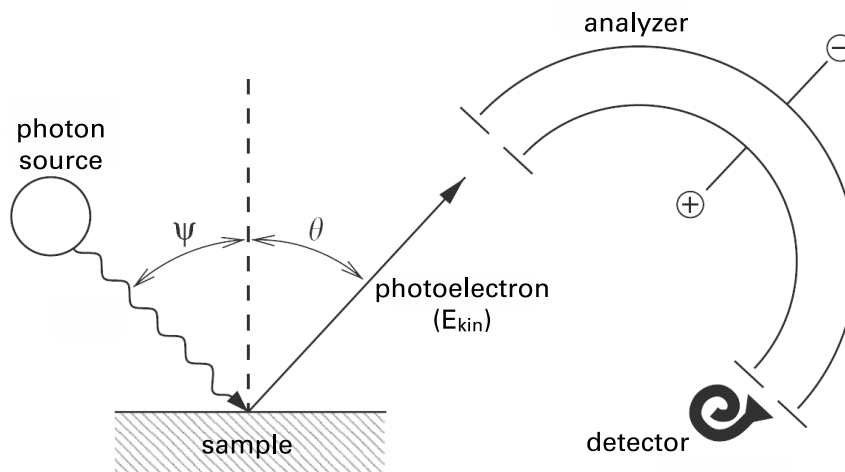


Figure 4.1: Basic setup for a photoelectron spectroscopy experiment: Photons from a source hit the surface of the sample under investigation. The kinetic energy of the emitted photoelectrons is determined by an energy analyzer combined with an electron detector. (Reproduced after [Hüf05].)

4.1.1.2 Setup

To realize a photoemission experiment, we need, besides the sample under investigation, a photon source on the one hand and an analyzer system (in the following also called the spectrometer) that detects the number and energy of the emitted photoelectrons on the other hand (figure 4.1). Furthermore a PES experiment requires ultrahigh vacuum (UHV) conditions to ensure clean sample surfaces, since contaminations would strongly diminish the rate of electrons emitted by the underlying sample and the spectrum would become dominated by electrons stemming from the contamination layer.

According to the type of excitation light source used one divides the field of PES into *ultraviolet photoelectron spectroscopy* (UPS) and *x-ray photoelectron spectroscopy* (XPS), where the first technique is sensitive to the valence band structure and the latter is applied to excite and analyze core levels.

Laboratory sources for UPS are differentially pumped gas discharge lamps, which are in most cases operated with helium (photon energy of the He I line: 21.22 eV). For XPS x-ray tubes are used. Their emission lines are defined by the characteristic x-ray fluorescence lines of the anode material. The most popular materials are aluminum and magnesium. The strongest emission lines are Al $K\alpha_{1,2}$ and Mg $K\alpha_{1,2}$ with x-ray photon energies of 1486.6 eV and 1253.6 eV, respectively³. For a table of other line sources and

³One has to be aware of the fact that without an x-ray monochromator also weaker emission lines are present, which are also capable of generating photoelectrons and lead to additional peaks in the spectrum (x-ray satellites). This fact has to be considered for the assignment and interpretation of spectral features.

their characteristic energies as well as technical drawings of gas discharge lamps and x-ray tubes see e.g. [Lüt98]. The modern alternative to those classical sources is synchrotron radiation, which yields a continuous spectrum of photon energies.

The analyzer system typically consists of three elements: the collection lens system, the energy analyzer, and the detector. The most common energy analyzer today is the electrostatic hemispherical analyzer operated at a constant pass energy. It consists of two concentric hemispheres, between which a certain potential ΔV is applied. An electron whose kinetic energy equals a certain pass energy E_{pass} , which is defined by ΔV , is able to traverse the analyzer along a circular orbit in the middle between the two hemispheres to finally reach the detector. To count *only* electrons of a kinetic energy E_1 , the voltages at the lens system are adjusted such that electrons with the energy E_1 are retarded to the pass energy E_{pass} . The other task of the lens system is, of course, to focus the photoelectrons to the entrance slit of the hemispheres. One can show mathematically that the hemispheres deflect and guide only electrons with the *correct* energy, namely E_{pass} , to the exit slit of the hemispheres. There the electrons hit a secondary-electron multiplier and the resulting electron pulses are transformed to electric standard pulses, which are finally counted. One may ask now how an energy scan, in other words, the variation of E_1 , becomes possible. For that purpose a control voltage (typically delivered by the data acquisition computer via a digital-to-analog converter) is amplified and converted to the suitable potentials at the lens system and the hemispheres by a voltage divider. For an in-depth discussion of resolution issues, alternative analyzer architectures, and operation modes see e.g. [Bri03].

To be complete, we itemize the individual components of the PES system used within this thesis, as follows:

- x-ray source: Leybold RQ 63-10, equipped with a Mg anode, not monochromatized, operated at a voltage of 11 kV and an emission current of 14 mA;
- UV source: Fisons UVL-HI, operated with He;
- hemispherical energy analyzer: Leybold EA 10, operated at constant pass energy, transmission function varies with $1/E_{kin}$;
- ultrahigh-vacuum chamber, base pressure 10^{-10} mbar;
- data acquisition and control: multipurpose computer board National Instruments PCI-MIO-16XE-10, home-built software based on National Instruments LabVIEW.

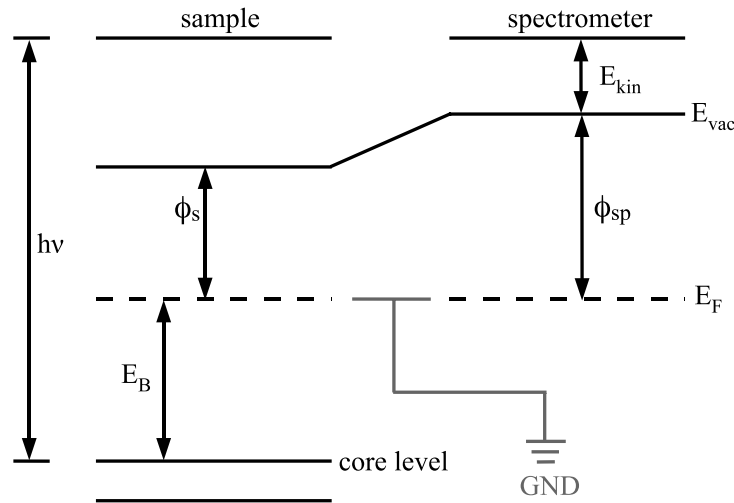


Figure 4.2: Energy level diagram for an electrically conductive sample that is grounded to the spectrometer. The FERMI levels E_F are aligned, which leads to the creation of a contact potential between sample and spectrometer. The binding energy E_B is referred to E_F . It can easily be seen that the value of E_B is defined by the values of the incident photon energy $h\nu$, the measured kinetic energy E_{kin} , and the work function of the spectrometer ϕ_{sp} , but is independent of the sample work function ϕ_s . The spectrometer work function has to be determined within a calibration measurement, see text.

4.1.2 Calibration

As indicated above [equation (4.1)], binding energies in PES are calculated from the measured kinetic energies of the photoelectrons. It is common practice to refer all binding energies to the FERMI level. For exact measurements the spectrometer has to be calibrated. To understand the deeper meaning of the calibration procedure, we must modify equation (4.1). The reason is that in a realistic PES experiment, the sample (if sufficiently conductive⁴) and the spectrometer are electrically connected to each other. In other words, their FERMI levels are at the same energy level (figure 4.2). Thus not the work function of the sample but of the spectrometer appears in equation (4.1) for true experimental conditions. Consequently, calibration means the determination of ϕ_{sp} . For that purpose the XP or UP spectrum of a clean surface of an elemental (noble) metal is measured. For UPS calibration the FERMI edge is determined. It defines the zero position of the binding energy scale (figure 4.3). For XPS calibration the binding energy scale is defined by some of the most intense core level lines in the spectrum of the calibration sample (figure 4.4).

In the present work, a Au(110) single crystal was cleaned by repeated cycles of Ar⁺ sputtering and heating and subsequently used for calibration (see figures 4.3, 4.4).

⁴Photoemission of insulating samples is much more problematic, because the samples get charged over time, which leads to an artificial shift of the spectrum along the energy axis. The problem can be overcome by active charge compensation by flooding the sample with low-energy electrons.

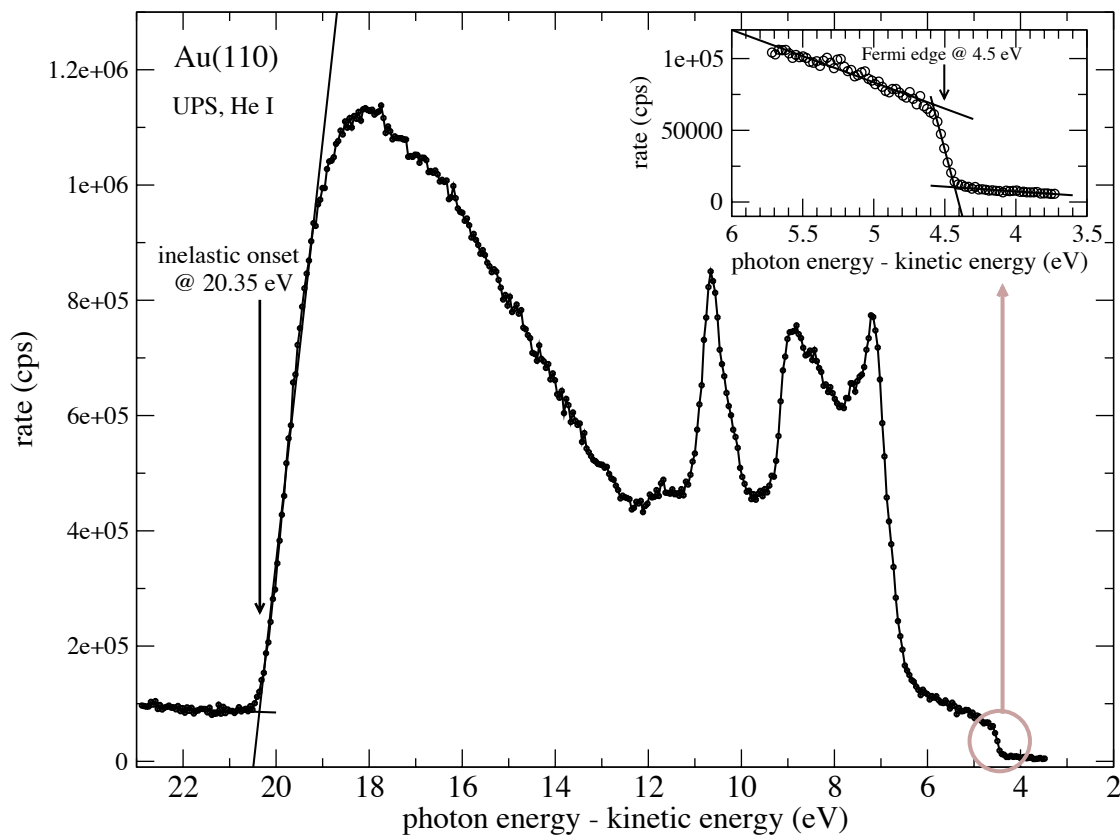


Figure 4.3: Reference ultraviolet photoelectron spectrum of a freshly cleaned Au(110) surface, acquired under He I excitation ($h\nu = 21.22$ eV) for the sake of calibration of the spectrometer. The inset shows the FERMI edge, which defines the zero position of the binding energy scale and thus the work function of the spectrometer (here: $\phi_{sp} = 4.5$ eV). In general, the UP spectrum reflects the density of valence states of the material under investigation. The width of the spectrum, i.e. the energy difference between the FERMI level and the onset on the high-binding-energy side (inelastic onset), additionally bears information on the work function of the sample (here: 5.37 eV). The analyzer pass energy was set to 2 eV.

4.1.3 Quantification

As discussed previously, an XP spectrum contains peaks that can be associated with the presence of various elements. But also the area below those peaks contains information: it can be associated with the amount of each element present. The evaluation of the absolute percentage of a certain element is difficult, because the peak area has to be corrected for several instrumental factors. Some of them are unknown in most cases. It is easier to determine the atomic *ratios* between two elements, since the unknown factors are eliminated then. Nevertheless the peak areas of elements *A* and *B* cannot simply be divided by each other. The reason lies in the fact that (i) the transmission of the analyzer is not constant over the whole kinetic-energy range, (ii) the photoionization cross sections

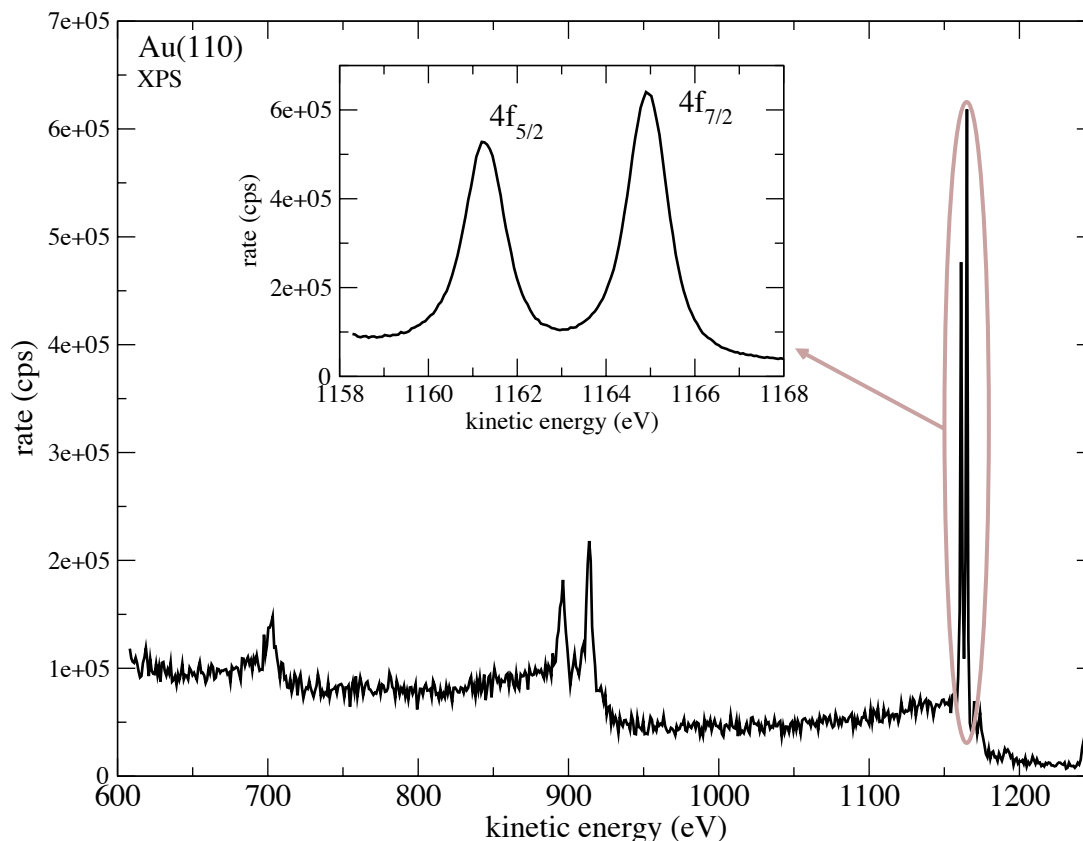


Figure 4.4: Reference x-ray photoelectron spectrum of a freshly cleaned Au(110) surface acquired under excitation by the Mg $K\alpha_{1,2}$ line ($h\nu = 1253.6$ eV) and with a pass energy of 30 eV. The energy axis reflects the raw data, i.e., the kinetic energy. To convert the kinetic energies correctly into binding energies, a high-resolution scan of the strongest core level signal, the Au $4f$ doublet, was taken (see inset). After peak fitting (for details on line shapes and other fitting parameters, see [Bri03, Vic97]), the peak positions, which are known and tabulated for elemental metals such as Au, define the spectrometer work function according to $E_B = h\nu - E_{kin} - \phi_{sp}$.

for different elements are not equal, and (iii) different orbital symmetries imply different escape probabilities. Those effects are subsumed in empirically derived *atomic sensitivity factors* (ASFs), which have been tabulated for several analyzer architectures. For the correct formula to obtain atomic ratios, see equation (4.2) in the following section.

4.2 Deducing the manganese valence in hole- and electron-doped lanthanum manganite thin films

Here, we employ UPS and mainly XPS to comparatively study epitaxial LCMO and LCeMO thin films with regard to their Mn valence and the closely related doping type. A compact version of the results has been published in [Bey06].

4.2.1 Motivation and state of the scientific discussion

Concerning the physics of lanthanum manganites, the majority of the reported research activities have so far been dedicated to hole-doped manganites in which part of the trivalent La ions of the parent compound LaMnO_3 have been replaced by *divalent* cations such as Sr^{2+} , Ca^{2+} , Ba^{2+} , Pb^{2+} , etc. Formally, this results in the chemical composition $(\text{La}_{1-x}^{3+}\text{A}_x^{2+})(\text{Mn}_{1-x}^{3+}\text{Mn}_x^{4+})\text{O}_3$. To preserve charge neutrality, part of the Mn ions are driven into the 4+ state which leads to an effective hole doping, where the conduction mechanism is based on electron hopping between the Mn^{3+} and Mn^{4+} ions via an oxygen ion, known as double exchange (see again section 2.2).

In analogy, from the aspect of possible manganite-based electronic devices, it is logical to ask whether a partial substitution of the La ions by *tetravalent* cations such as Ce or, so far less studied, Sn [Li99, Guo00, Gao03], Te [Tan03a, Tan03b, Yan04c, Yan05b], Zr [Roy01], or Th [Jos02] would lead to an electron-doped compound. Straightforward, one then expects the nominal composition $(\text{La}_{1-x}^{3+}\text{A}_x^{4+})(\text{Mn}_{1-x}^{3+}\text{Mn}_x^{2+})\text{O}_3$, where part of the Mn ions have been driven to the Mn^{2+} state. However, as the Mn^{2+} ion has a large ionic radius and the tetravalent ions have, compared with La^{3+} , a small radius, the question was raised whether such a crystal can be chemically stable at all [Jos02]. Nevertheless, the hope has been that the physics (including the double exchange and the strong electron-lattice coupling) of those new compounds would be similar to that of hole-doped manganites. Thus, also the tetravalent-ion-doped manganites are expected to show all the unusual physical properties, including the CMR effect. Band structure calculations [Min01] supported the argument that a mixed $\text{Mn}^{2+/3+}$ state could be possible.

Several groups [Man97, Geb99, Lee01] succeeded in synthesizing Ce-doped manganites via a solid-state reaction route and reported evidence for metal-insulator and ferromagnetic-paramagnetic phase transitions, as well as for a CMR effect. On the other hand, the new manganites often suffered from overoxygenation [Man97], and their properties turned out to be much more sensitive to the oxygen content and thus to the preparation conditions [Cha04, Yan04a] than those of their hole-doped relatives. Even worse, accurate

x-ray diffraction analyses showed that the compounds always included an unreacted CeO_2 (or SnO_2 etc.) impurity phase or were generally a multiphase compound of self-doped $\text{La}_{1-x}\text{MnO}_3$, CeO_2 , and Mn_3O_4 [Jos02], or an even more complex mixture [Can00]. GANGULY et al. [Gan00] generally questioned the possibility of Ce doping of LaMnO_3 and argued that the observed CMR effect and the metallic conductivity originated from a La-deficient $\text{La}_{0.7}\text{MnO}_3$ phase, motivated by work of PHILIP et al. [Phi99] who gave evidence of hole rather than electron doping from thermopower measurements. Other researchers suggested that mixtures of $\text{Ce}^{3+/4+}$ and $\text{Mn}^{2+/3+/4+}$ would be possible [Phi99, Gay04], demonstrated the existence of Mn^{2+} ions in hole-doped $\text{La}_{0.7}\text{Sr}_{0.3}\text{MnO}_3$ [Jon05], or generally questioned the well established $\text{Mn}^{3+/4+}$ picture [Hun97].

At least the problem of phase separation seemed to be solved when RAYCHAUDHURI et al. [Ray99] and MITRA et al. [Mit01a, Mit01b] succeeded in preparing single-phase epitaxial LCeMO *thin films* by pulsed-laser deposition, which opened the way to lanthanum-manganite-based *pn* junctions [Mit01c, Cho05] or tunneling magnetoresistance (TMR) structures [Mit03b].

In order to either directly or indirectly prove the expected electron doping, numerous more or less elaborate experimental approaches have been followed so far, among them HALL measurements [Gao03, Ray03, Yan04b], co-doping with divalent ions combined with resistance measurements [Ray99], thermopower measurements [Phi99, Yan05b], X-ray absorption spectroscopy (XAS) [Mit03a, Han04b, Han04a], X-ray photoemission spectroscopy (XPS) [Gao03, Tan03a, Han04b, Han04a], or X-ray absorption near-edge-structure (XANES) spectroscopy [Aso04, Lin04].

Up to the present, all those studies have almost alternately brought indications for either hole or electron doping in tetravalent-ion-doped manganites, in bulk samples as well as in epitaxial thin films. It is an aggravating fact that an impurity-free x-ray diffraction pattern does not necessarily mean that the compound shows *n*-type conduction [Yan04b]. Obviously, the question whether LaMnO_3 accepts electron doping has to be answered for each sample individually.

4.2.2 Experimental approach of the present work

In this work, the application of x-ray diffraction to ensure single-phase composition (as a necessary but not sufficient constraint) followed by an extensive XPS analysis, which provides information *both* on the valence states of the Mn and tetravalent ions *and* on the chemical composition of the outermost 3 nm of the films, is proposed. Additionally, the XPS analysis gives information on the oxygen content and on possible surface segregation.

LCeMO and LCMO epitaxial thin films⁵, as described in section 2.3 with respect to their preparation, morphology, and XRD analysis, were comparatively studied. It is demonstrated how the analysis of the XPS peak areas and of the exchange splitting⁶ of the Mn 3s core level signal, which is a definite indicator for the Mn valence [Zha84, Gal02, Nel00] and has so far only sporadically been applied to the problem of electron- and hole-doped manganites [Kow00, Tan03b, Jon03], makes possible a clear analysis of the oxygen content and a quantitative determination of the Mn valence. It is shown that the oxygen content can be varied by heating in ultrahigh vacuum or in an oxygen atmosphere and that this allows us to *tune* the Mn valence and consequently the doping type in a *reversible* way.

Prior to each XPS session, special attention was paid to the surface cleaning of the samples. Several reports [Cho99a, Cho99b, Dul00, Jon03] suggest a heating procedure at 450 °C or 500 °C in UHV. To the experience made during the present work, this does not completely remove carbon contaminants; the carbon 1s core level peak was still observable in the XP spectra after such a treatment. This fact is not astonishing, since lanthanum manganite surfaces act as catalysts [Lia93, Dec99, Pon00, Zha02], which demonstrates their high chemical reactivity. Therefore cycles of repeated heating at 470 °C for at least 2 hours at an oxygen pressure of 10⁻⁶ mbar were employed. Heating in an oxygen atmosphere is a common method for the UHV preparation of reactive surfaces such as platinum, as it oxidizes the carbon on the surface to CO₂, which subsequently more easily desorbs from the surface. In the case of lanthanum manganites as well as other metal oxides, the oxygen plays another important role: it prevents oxygen diffusion out of the samples [Dör00]. After each cleaning procedure, it was checked that the C 1s signal had disappeared. Typically, the freshly prepared surfaces remained clean for at least four hours.

After an obligatory survey scan (see figure 4.5 for LCeMO), the core level peaks with the highest intensities, i.e. La 3d, O 1s, Mn 2p, and Ca 2p or Ce 3d for LCMO or LCeMO, respectively, were acquired with an energy resolution of 2 eV, which corresponds to an analyzer pass energy of 70 eV, with a step width of 0.2 eV, and a measurement time of 10 seconds per step. The Mn 3s line, which is much weaker than the Mn 2p line,

⁵Since LCMO and LCeMO are considered as *twin* compounds due to their similar transition temperatures, it is somehow a natural choice to compare *those* two compounds.

⁶It is clearly beyond the scope of this work to explain all sorts of possible spectral features in PES. Thus we only focus on those which are relevant to the interpretation of the LCMO and LCeMO spectra, first of all the *multiplet splitting*, which is also referred to as *exchange splitting* or *electrostatic splitting*. In the case of the Mn 3s signal the photoelectrons from the 3s shell have either spin up or spin down. When leaving the atom they interact with the unpaired 3d electrons, which results in two different final kinetic energies according to the previous spin state. This quite simple model can be additionally complicated by further relaxation and configuration interaction processes, see e.g. [Bri03].

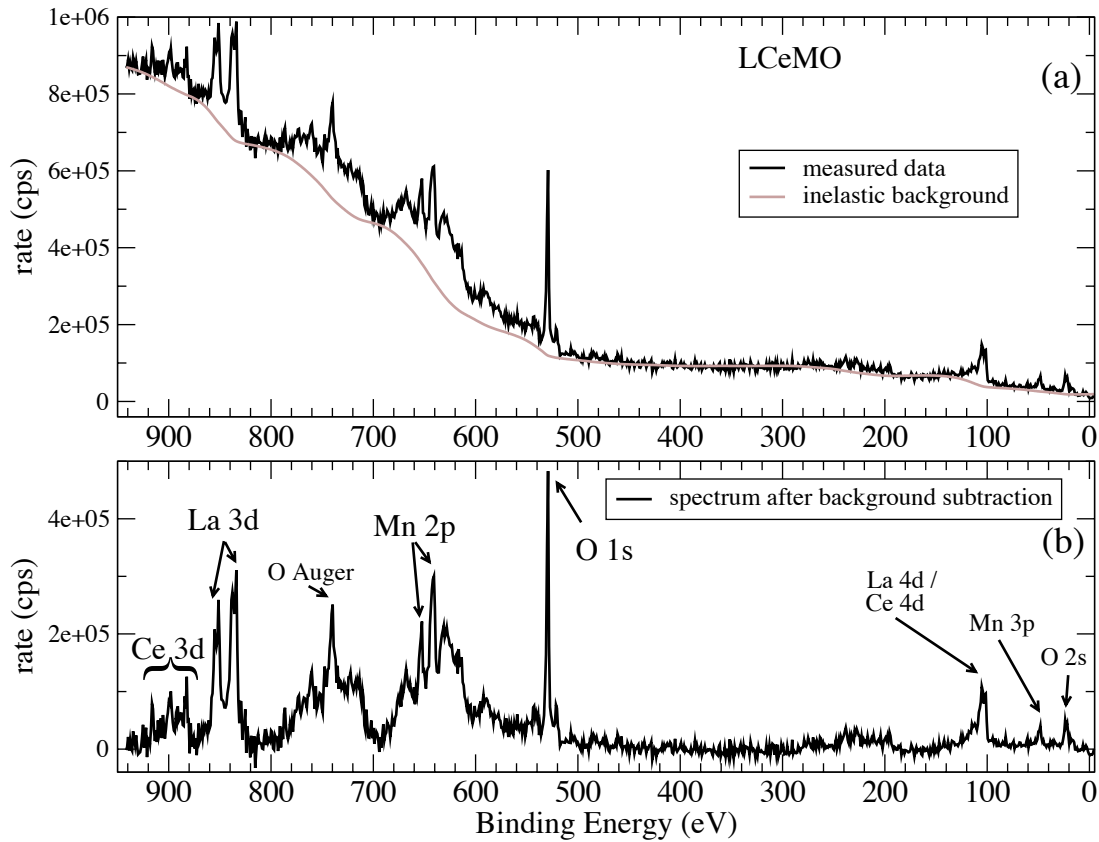


Figure 4.5: XPS survey scan of the cleaned LCeMO thin film, acquired with a pass energy of 100 eV. Part (a) shows the raw data after binding-energy conversion and the inelastic background as calculated with the TOUGAARD algorithm. Part (b) depicts the background-corrected signal with the assignments of the main features. It is obvious that the interpretation of a spectrum of a quaternary compound, such as LCeMO, taken with the radiation of a nonmonochromatic laboratory source, is much more of a challenge than that of a metal spectrum as shown before.

was scanned with a higher pass energy of the analyzer of 100 eV, which resulted in a slightly worse energy resolution of 2.5 eV. The measurement window was enlarged to 60 seconds per scan step to improve the signal-to-noise ratio. Unfortunately, the smaller peak of the Mn 3s doublet is located within the direct neighborhood of the Mg $K\alpha_{3,4}$ satellites of the La 4d signal (see figure 4.6). Consequently, the whole La 4d region of the spectrum had to be measured additionally in order to deconvolute the several contributions and to find the correct level for the correction of the inelastic background. For the evaluation of the XPS data, the SHIRLEY background correction [Shi72] and the peak fitting software XPSPEAK 4.1 [Kwo00] were used. The integral peak areas of the most intensive peaks were employed to calculate the concentration ratios between the

elements of each compound within the XPS probing depth according to the relation:

$$\frac{c_A}{c_B} = \frac{I_A s_B}{I_B s_A} \quad . \quad (4.2)$$

Here, c_A and c_B are the concentrations of atoms of types A and B, I_A and I_B denote the XPS peak areas after background correction, and s_A and s_B are the empirically derived atomic sensitivity factors for an energy analyzer whose transmission function varies with the inverse of the electron kinetic energy, taken from [Bri83].

On the basis of the measured Mn 3s level splitting ΔE_{3s} , the Mn valence v_{Mn} was calculated by employing the following linear equation:

$$v_{Mn} = 9.67 - 1.27 \Delta E_{3s}/\text{eV} \quad , \quad (4.3)$$

which was obtained by averaging the results of [Gal02] and [Zha84], where the linear relationship between v_{Mn} and ΔE_{3s} is derived for the valence range between +2 and +4 from XPS investigations of different bulk mixed-valent manganites and of binary Mn oxides, respectively. For comparison, the Mn valence was also calculated from the film stoichiometries as extracted from the peak area analysis.

The XP spectra were acquired after seven different sample treatment steps (see table 4.1) in order to compare the Mn valences for various stoichiometries, especially several degrees of oxygen deficiency. Step *a* denotes the pure cleaning procedure. Steps *b-f* contain a cleaning procedure in an oxygen atmosphere followed by a deoxygenation procedure without oxygen supply at different heating temperatures and variable durations. Step *g* was applied in order to reoxidize the manganite films to restore the state that had been reached after step *a*. The temperatures are approximate values, since the sample temperature was measured by an optical pyrometer⁷ without exact knowledge of the emissivity of the manganite films. The emissivity was set to 0.8, which is a typical value for metal oxides [Lid01]. The base pressure in the preparation chamber was 10^{-9} mbar.

Two additional test procedures were performed after steps *a* and *f* for both samples. First, the O 1s peak was acquired at four values of the intensity of the X-ray source differing by a factor of up to 3.5, to make sure that no spectral shift occurs when the total photoelectron current is changed. This proves that the films provide enough conductivity to prevent any charging that could cause artificial line shifts. Second, an ultraviolet photoelectron spectrum (UPS) was taken to monitor the change of the work function of the films.

⁷Impac, IGA 100

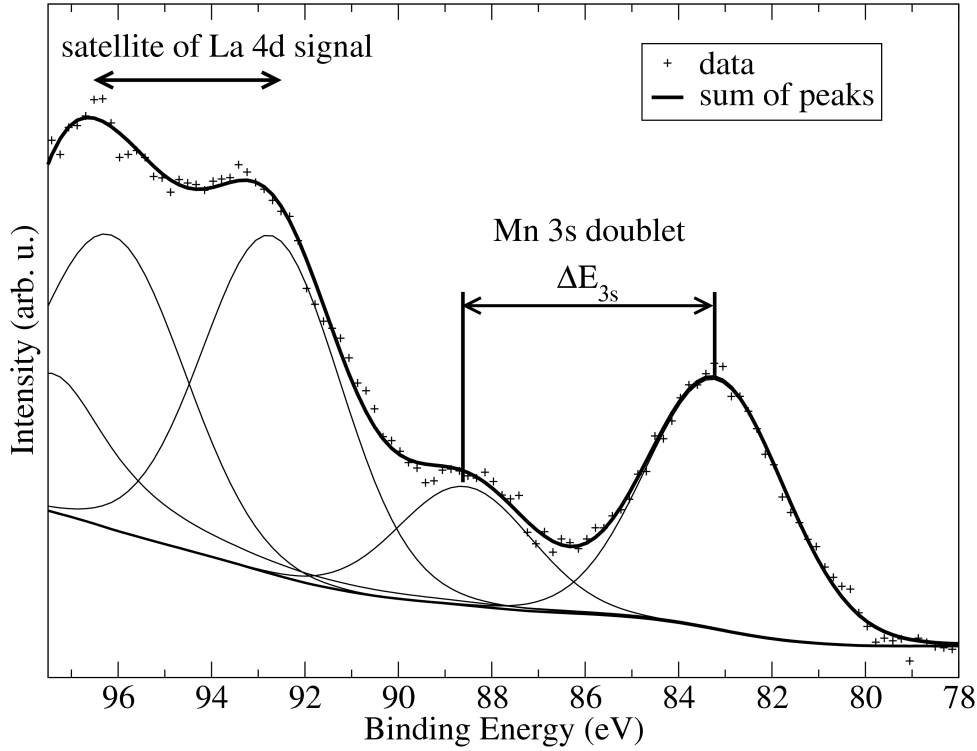


Figure 4.6: Mn 3s core level signal and La 4d satellite signal for the LCeMO thin film on SrTiO₃(100) with corresponding peak fits and SHIRLEY background. The La 4d satellite is fit by a four-peak structure (the fourth peak is outside the binding energy range shown) as suggested in [How78], where the multicomponent structure of the 4d orbital of La³⁺ is explained in detail.

4.2.3 Results and discussion

4.2.3.1 XPS peak areas and stoichiometry

The atomic ratios between the elements were estimated from the integral peak areas of the La 3d, Ce 3d, Ca 2p, O 1s, and Mn 2p core level signals on the basis of equation (4.2). The nominal compositions of the LCMO and the LCeMO films resulting from this procedure

index	sample treatment
<i>a</i>	470 °C, 2h, 10 ⁻⁶ mbar O ₂
<i>b</i>	470 °C, 2h, 10 ⁻⁶ mbar O ₂ / 470 °C, 1h, UHV
<i>c</i>	470 °C, 1h, 10 ⁻⁶ mbar O ₂ / 520 °C, 2h, UHV
<i>d</i>	470 °C, 1h, 10 ⁻⁶ mbar O ₂ / 570 °C, 2h, UHV
<i>e</i>	470 °C, 1h, 10 ⁻⁶ mbar O ₂ / 620 °C, 2h, UHV
<i>f</i>	470 °C, 1h, 10 ⁻⁶ mbar O ₂ / 670 °C, 2h, UHV
<i>g</i>	470 °C, 3h, 10 ⁻⁶ mbar O ₂ (reoxidation)

Table 4.1: Description of the seven different surface treatment steps applied to the LCMO and LCeMO thin films. Note that the original as-cleaned state of the films was reestablished by heating in an oxygen atmosphere *before* each new deoxygenation step.

are listed in table 4.2. The normalization to manganese is arbitrary. Note that the compositions of table 4.2 are valid provided that the depth probed by XPS is smaller than the film thickness, which is well fulfilled in our case, and under the assumption of homogeneous films. Furthermore, the values are subject to an estimated error of at least 10%, which is mainly caused by the uncertainty of the Mn $2p$ peak area and the error of the inelastic background correction [Tou96]. The Mn $2p$ doublet is surrounded by several broad Ce, Mn, and La AUGER lines (Ce $M_5N_{45}N_{45}$ at 594 eV, Mn $L_3M_{45}M_{45}$ at 620 eV, La $M_5N_{45}N_{45}$ at 632 eV, Mn $L_3M_{23}M_{45}$ at 670 eV) [Mui79]⁸. Consequently, it is difficult to exactly isolate the pure Mn $2p$ peak area. That is the reason why the apparent Mn excess should not be overvalued. Further systematic errors occur due to the uncertainty of the atomic sensitivity factors of La, Ce, and Mn. This manifests a fundamental problem, as the atomic sensitivity factors for rare-earth and transition metal elements vary strongly for different valence and binding conditions [Bri83]. We come back to this point later when discussing the formal Mn valences.

Nevertheless, for both film surfaces investigated here, there is a clear indication of oxygen loss from step *a* towards step *e*. The development between steps *b* and *d* is dominated by stoichiometry fluctuations without any clear tendency. After step *g* a considerable oxygen reuptake is observed. Here, the stoichiometries of both film surfaces agree even better with the stoichiometries of the PLD targets than after step *a*. Considering the La:O ratio, there is an oxygen excess after steps *a-d* and again after step *g* for LCeMO and after all treatment steps for LCMO. Examining the La:Ce ratio in LCeMO, we observe a Ce excess after the treatment steps *a-f*, whereas the correct ratio is found after step *g*, to within the error margin. As for the La:Ca ratio in LCMO, we find an excess of Ca after steps *e-g*. This points to Ca segregation to the surface [Zha98, Cho99a, Cho99b], which is supported by the analysis of the O:Ca ratio, which also shows Ca excess (except for step *g*). It must be taken into account that the results of table 4.2 are only valid within the XPS probing depth. A typical value for the inelastic mean free path of electrons in inorganic compounds at a kinetic energy of 1000 eV is 2 nm [Bri03], which means that 78% of the signal comes from the outermost 3 nm of the film.

In the following, we focus on the different core level signals in detail, which will also clarify the reasons for the strongly changed stoichiometry of the LCeMO film after step *f*.

⁸Note that the usage of Al instead of Mg as the anode material of the x-ray source would eliminate the problem of the overlapping AUGER lines but would also cause a La $4d$ satellite in the neighborhood of the Mn $3s$ signal at an even more awkward position.

index	LCMO	LCeMO
<i>a</i>	La _{0.32} Ca _{0.20} MnO _{2.31}	La _{0.41} Ce _{0.21} MnO _{2.73}
<i>b</i>	La _{0.31} Ca _{0.22} MnO _{2.30}	La _{0.39} Ce _{0.19} MnO _{2.32}
<i>c</i>	La _{0.33} Ca _{0.21} MnO _{1.88}	La _{0.39} Ce _{0.20} MnO _{2.35}
<i>d</i>	La _{0.34} Ca _{0.22} MnO _{2.14}	La _{0.50} Ce _{0.19} MnO _{2.43}
<i>e</i>	La _{0.35} Ca _{0.20} MnO _{1.77}	La _{0.43} Ce _{0.14} MnO _{1.80}
<i>f</i>	La _{0.45} Ca _{0.25} MnO _{2.01}	La _{0.75} Ce _{0.27} MnO _{3.00}
<i>g</i>	La _{0.48} Ca _{0.32} MnO _{3.03}	La _{0.54} Ce _{0.21} MnO _{2.96}
	La _{0.70} Ca _{0.30} MnO _{3.00}	La _{0.70} Ce _{0.30} MnO _{3.00}

Table 4.2: Chemical compositions of the LCMO and LCeMO films after seven different treatment steps. For comparison, the nominal stoichiometry (as expected from the PLD targets) has been added in the last line. Note that the values refer only to the outermost few nanometers of the film and that the errors are estimated to be greater than 10%. Note also that for the film as a whole a change of the concentrations of the metal ions is not expected.

4.2.3.2 O 1s core level signal

Figure 4.7 presents the development of the O 1s signal for both investigated films after the first six steps of treatment as listed in table 4.1. Several tendencies can be observed: With increasing heating temperature and thus progressive oxygen loss, the O 1s signal moves towards higher binding energies and the peak height decreases slightly.

The correct interpretation of the manganite O 1s peak seems to be difficult, as the literature contains many contradictory statements. Some groups [Lia93, Dec01] (however, those statements are for La_{1-x}Sr_xMnO₃) suggest three contributions to the O 1s signal and attribute them to the binding to each of the three other elements of the compound. According to this interpretation, the Mn-O component is located at about 529 eV and the La-O component at about 531 eV. This would be consistent with the O 1s signals of the present work, but a third component at a higher binding energy, which could be attributed to Ca-O or Ce-O (analogously to Sr-O) cannot be found in our data. The peak can be well fit by two but not three lines.

Other groups [Cho99a, Cho99b, Pon00, Zha02] observe a two-peak structure, with a component attributed to lattice oxygen at lower binding energies and a component attributed to surface- or defect-related oxygen at higher binding energies. This interpretation is more consistent with the observations of the present work. Then, an increase of the lattice-to-surface oxygen ratio with increasing heating temperature can be stated. Unaffected by those controversial details, the O 1s peak is a more direct and thus more reliable indicator for the control of oxygen loss than the element ratios obtained from the peak area analysis.

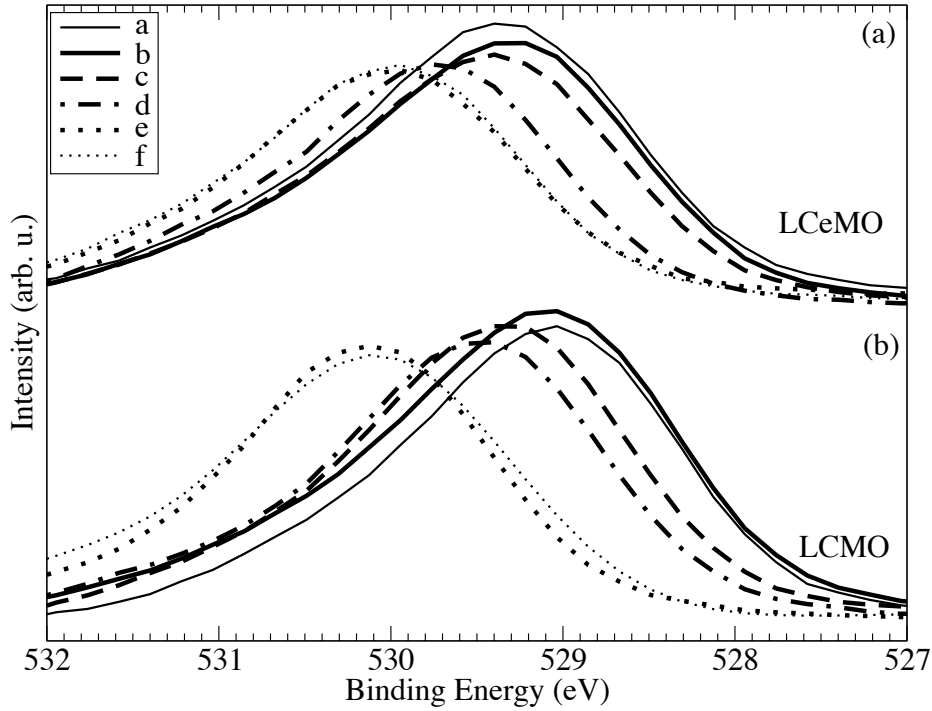


Figure 4.7: O $1s$ core level signals after background subtraction for LCeMO (a) and LCMO (b). The legend refers to the treatment procedures of table 4.1. For the reason of visual clarity, the peaks corresponding to the reoxidized state (step g), which are almost congruent with the respective peaks after step a , are not shown in the diagram.

4.2.3.3 Ce $3d$ and Ca $2p$ core level signals

The interpretation of Ce $3d$ spectra of Ce compounds has been the subject of a number of experimental and theoretical studies [Gun83, Fug83, Wui84, Sch85, Col98, Mul98, Pei01, Tol03]. In general, the Ce $3d$ spectrum exhibits a spin-orbit splitting of 18.6 eV, which could be verified for the LCeMO film in the present work. Furthermore, both spin-orbit components show a multiplet splitting⁹ into either two components for the pure Ce³⁺ state, as in Ce₂O₃, (denoted as v_0, v', u_0, u') or three components ($v, v'', v''', u, u'', u'''$) for the pure Ce⁴⁺ state, as in CeO₂. Consequently, for an arbitrary mixed-valence state, each of the two spin-orbit components must be fit by five peaks (see for example [Zha04] and references therein). The percentages of Ce³⁺ and Ce⁴⁺ can then be determined by evaluating the peak areas attributed to the two different oxidation states. Figure 4.8 depicts the Ce $3d$ signals for the cleaned LCeMO surface (step a) and after heating at 620 °C (step e). The cleaned film shows, as expected, a typical Ce⁴⁺ spectrum; only the

⁹In general, multiplet splitting does not only occur in s shells as discussed before but also in p or d shells, where it is more complex due to the different orbital symmetries. The multiplet splitting of the Ce $3d$ signal is caused by $3d-4f$ interactions and can be utilized as a valence indicator.

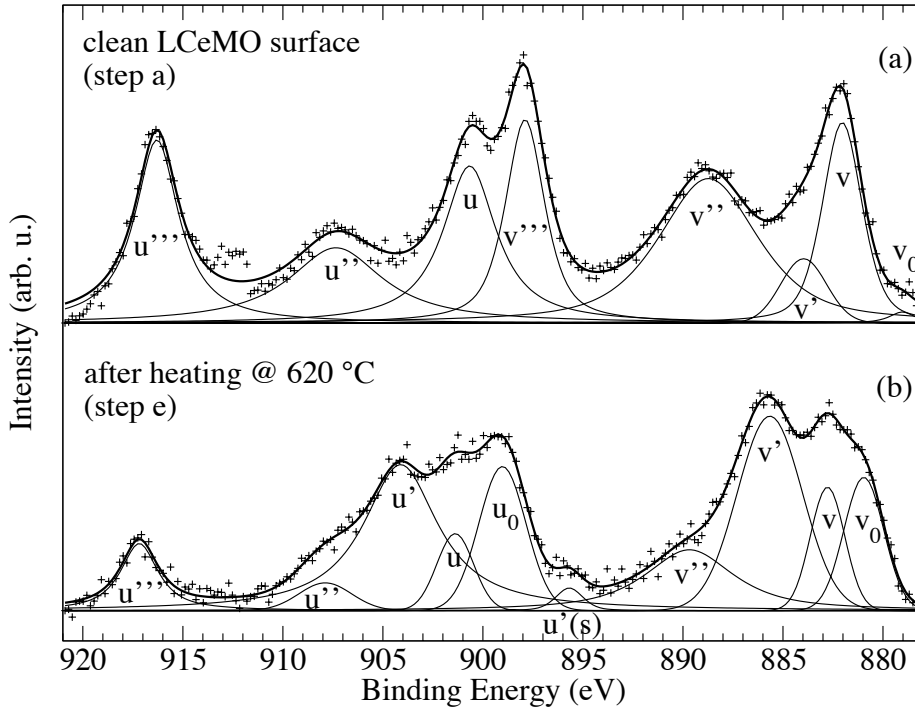


Figure 4.8: (a) Ce 3d signals for the clean LCeMO surface (after step *a* in table 4.1) and (b) after heating at 620 °C (step *e* in Table 4.1) after background subtraction. In accordance with the change of the Ce valence, the spectra have a clearly different shape. In curve (b) $u'(s)$ denotes the $K\alpha_3$ satellite of u' .

two strongest Ce^{3+} peaks can be discerned. The Ce^{3+} concentration is about 4%. A slight rise in the Ce^{3+} percentage to values around 10% occurs after steps *b-d*. The treatment steps *e* and *f* dramatically change the Ce valence towards the Ce^{3+} state, resulting in Ce^{3+} percentages of more than 50% for both cases. Figure 4.8(b) demonstrates the significantly different Ce 3d spectrum after treatment step *e*. It is interesting to note that also the O 1s peak shift is most dramatic after step *e* for LCeMO as well as for LCMO (see figure 4.7). The Ce valence change turns out to be reversible by reoxidation: The Ce^{3+} percentage shrank to 6% after step *g*.

In LCMO, the Ca 2p signal is shifted by 0.3 eV towards higher binding energies after step *c* and by 1.0 eV after step *e* and moves back to the original position after step *g*.

In summary, an increased oxygen diffusion above approximately 600 °C can be assumed for both films.

4.2.3.4 La 3d core level signal

The shape of the La 3d peaks is the same for LCMO and LCeMO and is similar to the shape found in the spectrum of La_2O_3 [Mui79]. The spin-orbit splitting is, as for La_2O_3 ,

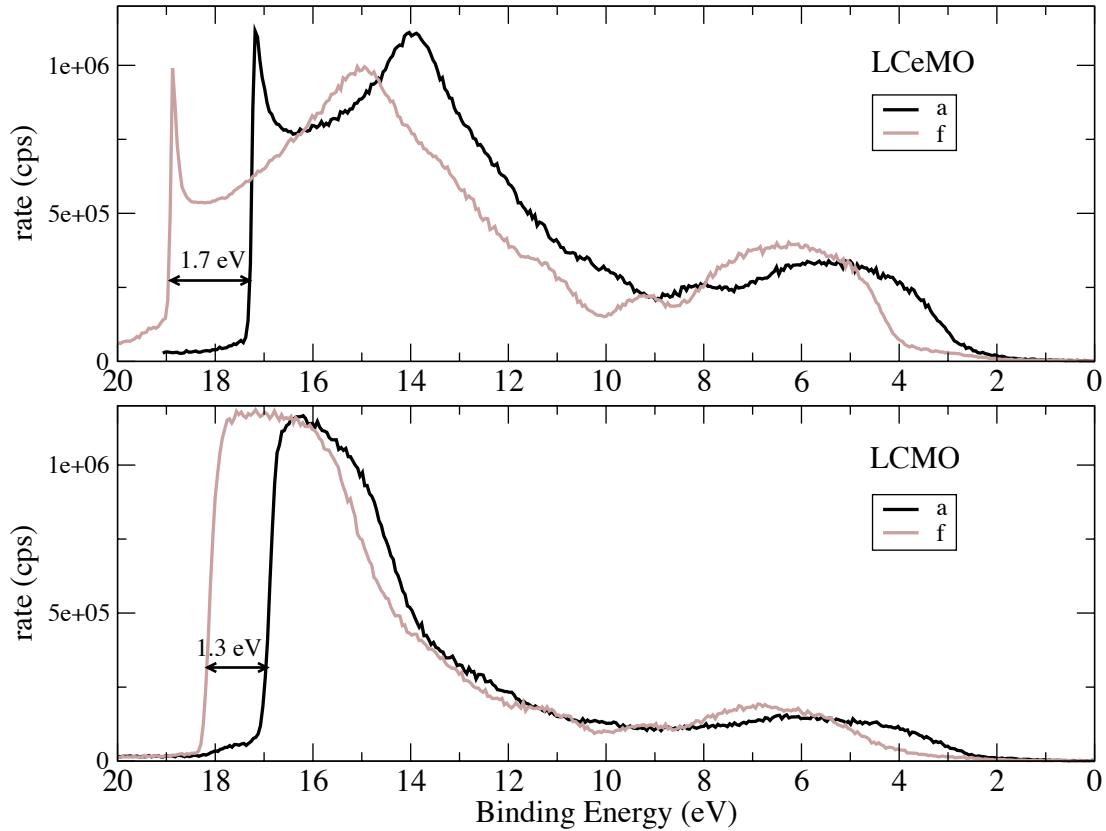


Figure 4.9: Ultraviolet photoelectron spectra of LCeMO and LCMO in the as-cleaned (after step *a*) and highly deoxygenated (after step *f*) state, respectively. The He I line ($h\nu = 21.22$ eV) served as excitation source, the analyzer pass energy was 2 eV. There is a clear tendency towards a broadening of the spectra by deoxygenation in both cases. Assuming a simple semiconductor band scheme, this broadening is equivalent to a decrease of the work function, which corresponds to a change from *p*- to *n*-type conduction. The sharp peaks on the high-binding-energy side of the LCeMO spectra are due to detector saturation. The problem was overcome by defocusing of the UV source before the LCMO spectra were taken.

16.8 eV for both samples and after all treatment steps (figure 4.10). However, the La *3d* binding energy shifts in a steplike manner after step *d* for LCeMO (one step earlier than the dramatic change in the Ce valence) and after step *e* for LCMO (figure 4.11). In both cases the binding energy moves closer to the La_2O_3 value [Mui79]. The steplike shift of the binding energy is larger for LCMO, as well as the corresponding O *1s* shift is larger in that case. Furthermore, we note that for the clean surfaces the La *3d* binding energies differ by 0.3 eV between LCMO and LCeMO; a similar difference is observed for the O *1s* lines. Altogether, the behavior of the La *3d* peak supports the assumption of an enhanced oxygen loss in both films after step *e*; for LCeMO the process might begin already with step *d*. For both samples, the La *3d* peak moves back to the position observed after steps *a* and *b* after the reoxidation procedure of step *g*.

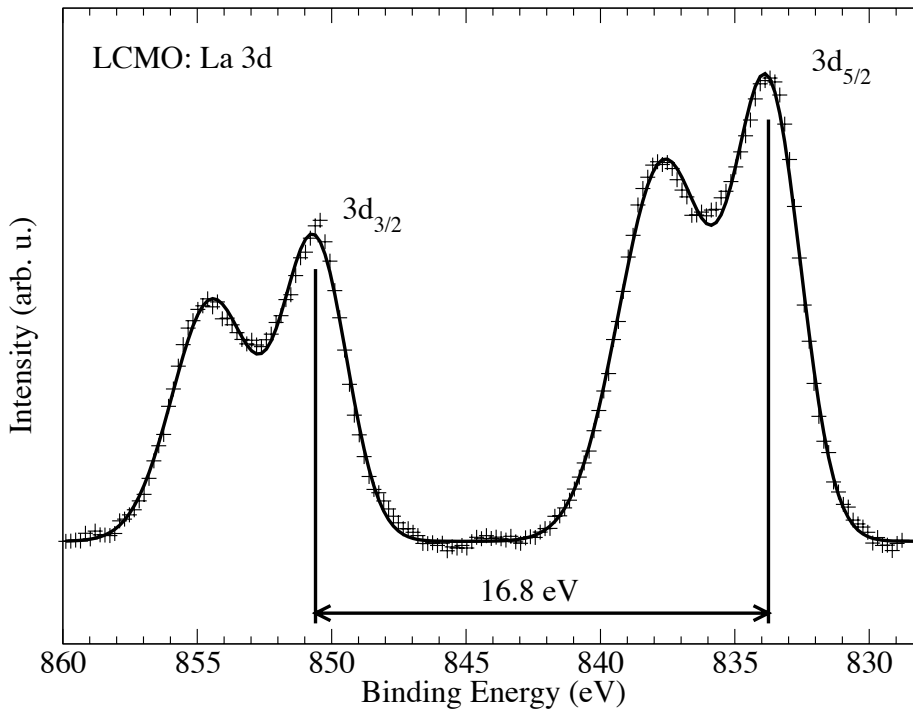


Figure 4.10: La 3d signal of the cleaned LCMO surface after subtraction of the background and the Mg $K\alpha_{3,4}$ satellites.

We note that there is a common trend of the O 1s, Ce 3d, Ca 2p, and La 3d lines: With progressive deoxygenation, they all move to higher binding energies. Apart from the fact that the shifts of the various core level lines may reflect changes in the individual binding conditions, their overall tendency towards higher binding energies is consistent with the Fermi level moving up in energy. This is confirmed by the UPS measurements, which show that the work function decreases between treatment steps *a* and *f* by 1.7 eV for LCeMO and 1.3 eV for LCMO (see figure 4.9). Such a behavior is in fact expected in a simple semiconductor band model if a transition from *p* to *n* doping takes place. Hence, we may interpret these observations as a first hint that deoxygenation indeed changes the doping type. Much stronger evidence for this is provided by the analysis of the Mn valence described in the following sections.

4.2.3.5 Mn 2p core level signal

To explore the Mn valence, the Mn core level signals should naturally provide the most relevant information. For a good introduction into the complex problem of manganese XPS core level signals, see for example [Nel00]. First, we consider the Mn 2p doublet, inspired by an XPS investigation of GAO et al. [Gao03]. There, the Mn 2p doublet of

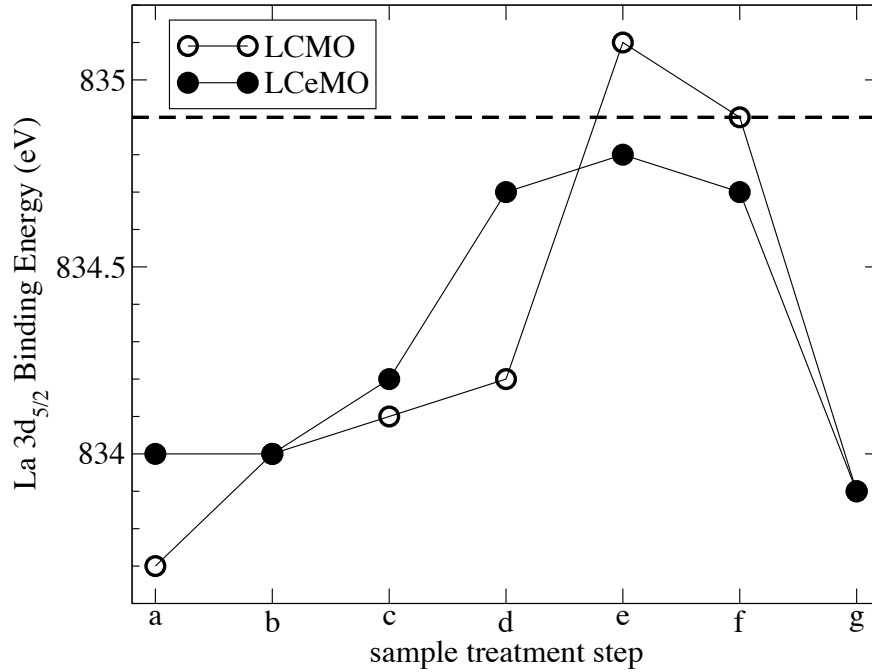


Figure 4.11: Development of the La $3d_{5/2}$ binding energy after the different heating steps b - f and the reoxidation step g (see also table 4.1 again). The dashed line indicates the value for La_2O_3 [Mui79].

$\text{La}_{0.9}\text{Sn}_{0.1}\text{MnO}_3$ exhibited a shift by 0.8 eV towards lower binding energies compared to the Mn $2p$ doublet of $\text{La}_{0.9}\text{Ca}_{0.1}\text{MnO}_3$, which was interpreted as evidence for a mixed $\text{Mn}^{2+/3+}$ state in $\text{La}_{0.9}\text{Sn}_{0.1}\text{MnO}_3$. However, another group [Kan01] observed the same Mn $2p$ binding energy both for LaMnO_3 compounds doped with divalent as well as tetravalent ions and questioned the suitability of the Mn $2p$ signal for investigations of the Mn valence.

Here, we see little or no energetic shift of the Mn $2p$ doublet, but we observe the formation of shake-up satellites¹⁰, especially after step f , which are offset from the main peaks of the Mn $2p$ doublet by approximately 5 eV towards higher binding energies. In agreement with all peak changes described before, the reoxidation drives the Mn $2p$ signal back to the shape which was observed after step a .

Figure 4.12 exemplarily shows the effect for the LCeMO film. For LCMO we find the satellite formation to be the same. This behavior is typical for Mn^{2+} systems such as MnO [Oku75, Hu81, Zha84]. Thus, it is clear that deoxygenation by heating in UHV

¹⁰Apart from the multiplet splitting discussed before, *shake-up satellites* are another spectral feature being important for the present manganite spectra. Shake-up satellite lines appear at the low-kinetic-energy side of the main peak, especially in systems with unpaired electrons in the $3d$ or $4f$ shell, and have their origin in an energy loss of the photoelectron due to an electronically excited state of the valence electrons. This excitation in turn has its origin in the perturbation of the valence electron system, since it sees the photoemission process as a change of the nuclear charge.

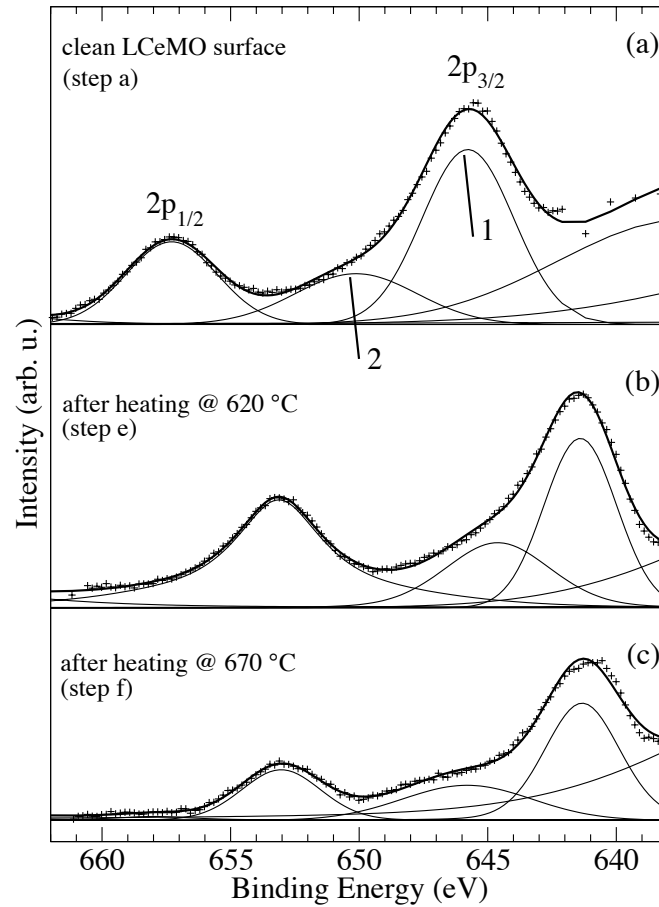


Figure 4.12: Mn $2p$ doublet of the LCeMO film after the treatment steps *a* and *f*. The Mn $2p_{3/2}$ component is fit by two peaks (labeled 1 and 2), with peak 2 corresponding to the shake-up satellite in curve (b). The Mn $2p_{1/2}$ component is fit by only one peak as the corresponding shake-up satellite is too weak to be visible. The overlapping peaks on the low-binding-energy side originate from AUGER lines, as discussed in the text.

drives the LCeMO *and* the LCMO film from the original $\text{Mn}^{3+/4+}$ state towards a mixed $\text{Mn}^{2+/3+}$ state. The analysis of the Mn $3s$ signal will show this in a more pronounced and quantitative manner.

In summary, the development of the Mn $2p$ doublet provides clear evidence for the presence of Mn^{2+} ions and thus the formation of an electron-doped state in both films. In the case of LCeMO we have to keep in mind that the Ce valence changes simultaneously towards the Ce^{3+} state (see figure 4.8). This might indicate a phase separation process (which, however, is reversible as can be seen after step *g*). This assumption is supported by the strongly changed stoichiometry (see table 4.2) after step *f* for LCeMO. According to the chemical formula given there, the formal Mn valence is higher after step *f* than after step *e*, but the Mn $2p$ signal after step *f* suggests a Mn valence closer to $2+$ than after

step *e*. On the other hand, the changed stoichiometry is only of limited significance, since the stoichiometry determination, in the LCeMO case, is based on three uncertain atomic sensitivity factors, namely those of La, Ce, and Mn. As the Mn and Ce valences change during the deoxygenation procedure, it is likely that also the atomic sensitivity factors change, which then produces a strongly but artificially changed stoichiometry. This is indeed observed after step *f* (table 4.2).

As a general result, we conclude that the Mn $2p$ signal can be used to get first qualitative information on the Mn valence of manganites: A lowering of the Mn valence is unambiguously visible by the formation of shake-up satellites at 5 eV from the main peaks.

4.2.3.6 Mn $3s$ exchange splitting

The value of the Mn $3s$ exchange splitting ΔE_{3s} was used to determine the Mn valence in a more quantitative way than is possible by means of the Mn $2p$ signal. As described in the literature [Zha84, Gal02], there is a linear relation between the Mn valence and the Mn $3s$ exchange splitting energy [equation (4.3)]. Figure 4.13 depicts the raw data of the Mn $3s$ doublet for LCeMO after the treatment steps *a* and *f*. One can clearly see that the exchange splitting has increased after step *f*. Because of the overlapping La $4d$ satellite and the rather low signal-to-noise ratio,¹¹ a quantitative evaluation is only possible by a fitting procedure as discussed in conjunction with figure 4.6. From the ΔE_{3s} values thus found, we calculated the Mn valences by means of equation (4.2) for both films after the different treatment steps. The result is shown in figure 4.14. The data give clear evidence that, without heat treatment in UHV, i.e., after step *a*, the LCeMO film is *not* in the mixed Mn^{2+/3+} state expected from the chemical formula of the compound. Instead, the Mn valence is similar in LCeMO and LCMO, close to the value expected for the nominal composition of the LCMO film. Figure 4.14 clearly shows that the oxygen out-diffusion induced by heating in UHV (steps *b-f*) lowers the Mn valence significantly in both cases down to values approaching +2. Finally, the reoxidation step *g* drives both films back to a state fairly close to the initial one. From the latter fact, it can be assumed that heating in an oxygen atmosphere, which constitutes the first part of *each* treatment step (see table 4.1), always essentially restores the state as reached after step *a*.

The error of the Mn valence is mainly caused by the error of the Mn $3s$ splitting value, which is assumed to be 0.2 eV for all data points. This value was derived from the peak fitting procedure, in which slight variations of the fit parameter constraints and of the background resulted in this uncertainty. The error bars thus mainly characterize

¹¹The stronger peak of the Mn $3s$ doublet is roughly 40 times lower in height than the O $1s$ peak, and is superimposed on a background that is 3.7 times higher than the peak itself.

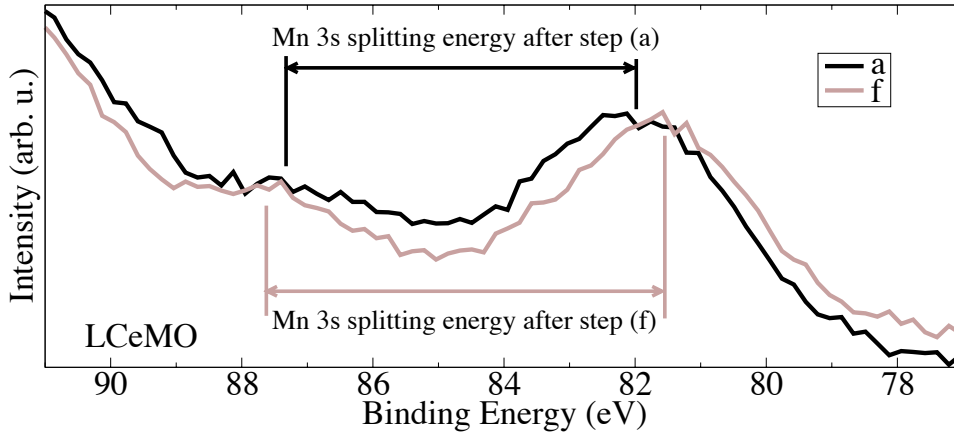


Figure 4.13: Mn 3s signals of the LCeMO film for the as-cleaned state (step *a*) and the heavily deoxygenated state (step *f*). The increase of the splitting energy is qualitatively visible, a quantitative analysis inevitably needs a fitting procedure due to the weakness of the signal and the neighboring strong La 4*d* satellite, as shown in figure 4.6.

the possible influence of systematic errors caused by the interfering La 4*d* satellite. Note that the change of ΔE_{3s} with heating temperature is expected to be less affected by such a systematic error than the absolute values.

As a check of consistency, another approach is chosen in figure 4.15. There, the Mn valences are derived from the stoichiometries of table 4.2 under the assumption of charge neutrality. Despite the uncertainty of the stoichiometries, the formal Mn valences derived from them exhibit a clear correlation with the Mn 3*s* energy splitting. The data points of the present work are depicted along with the data available in the literature [the same data that provided equation (4.3)]. Within the error bars we find a good agreement. While GALAKHOV et al. [Gal02] studied a wide variety of bulk manganese compounds having different formal Mn valences, we find the same linear relationship for one and the same manganite thin film when tuning its oxygen content.

For LCMO, the data demonstrates a clear increase of the Mn 3*s* exchange splitting with the decrease in Mn valence caused by the progressive rise in temperature. The correlation with the progression in heating temperature is not so clear for points *c* and *d*, which may be attributed to the large error of the formal Mn valence.

For LCeMO the same general tendency can be seen if we consider the points *a* and *e*. There are again fluctuations for the points between *a* and *e*. While in figure 4.14 point *f* for LCeMO fits well to the overall tendency set up by the other data points, this point shows a conspicuous deviation with regard to the formal Mn valence (figure 4.15). This can again be explained by the artificially changed stoichiometry, as discussed in detail in the previous section. As expected from the behavior of all other XPS signals, the

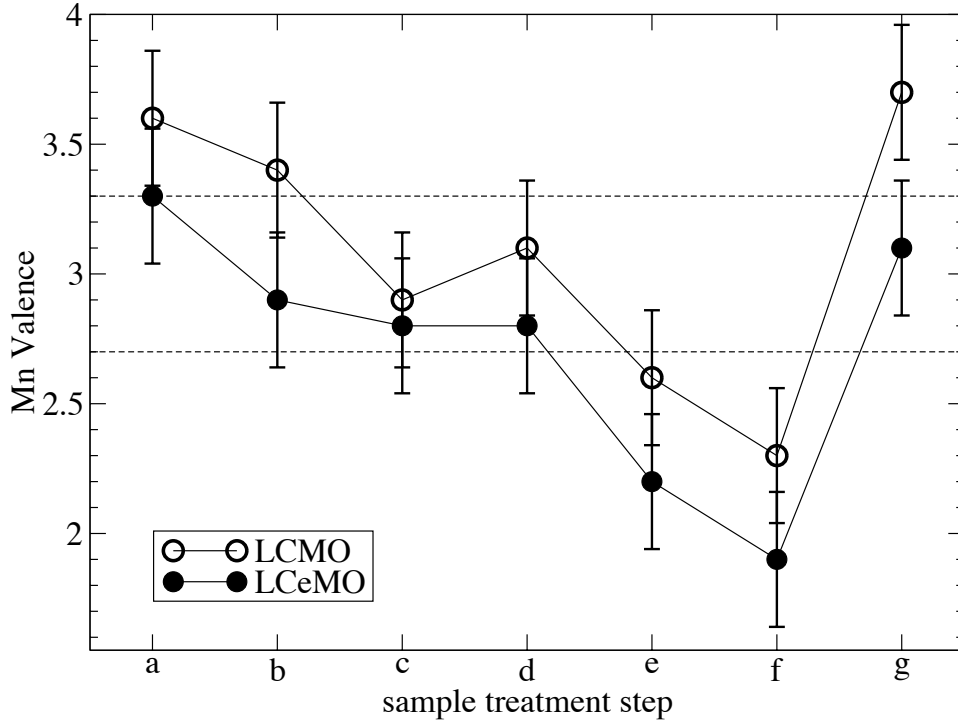


Figure 4.14: Mn valences of the LCMO and LCeMO film as derived from equation (4.3) after the different heat treatment steps of table 4.1. The horizontal dashed lines indicate the nominal Mn valences: 3.3 for LCMO and 2.7 for LCeMO. Thus one can conclude that the LCMO film has a Mn valence very close to its nominal value already in the as-cleaned state, while the LCeMO film is overoxygenated in the as-cleaned state and reaches its nominal Mn valence only after deoxygenation, especially after step *d*.

reoxidation of the films (point *g*) is accompanied by a decrease in the Mn 3s splitting and an increase of the formal Mn valence. The original state (*a*) is recovered within the error bars.

In figure 4.15 the error of the Mn 3s splitting energy is assumed to be 0.2 eV, as explained above. Here, the more pronounced error is that of the formal Mn valence, as this uncertainty results from the error of the peak areas. This error is even roughly doubled if one additionally takes the following errors of the atomic sensitivity factors into consideration: $s_{La} = s_{Ce} = 10 \pm 1$, $s_{Mn} = 2.6 \pm 0.1$; the remaining atomic sensitivity factors were assumed to have negligible errors.

In summary, the evaluation of the Mn 3s splitting gives clear evidence that it is possible to prepare a mixed Mn^{2+/3+} state and, consequently, electron doping in the outermost few nanometers of divalent- and tetravalent-ion-doped lanthanum manganite thin films by decreasing their oxygen content.

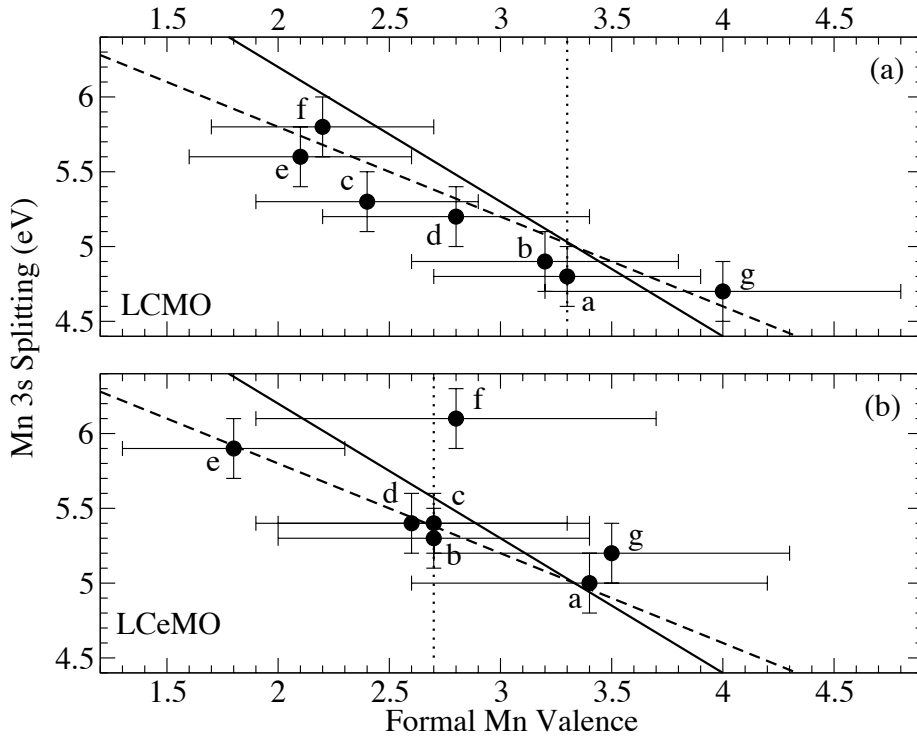


Figure 4.15: Plot of the Mn 3s exchange splitting energy versus the formal Mn valence, which was calculated by employing the stoichiometries from table 4.2, the corresponding Ce valences as determined from the Ce 3d signal, and fixed valences for the remaining elements (La^{3+} , Ca^{2+} , O^{2-}). Solid line: linear fit to the experimental data of GALAKHOV et al. [Gal02] for different mixed-valent manganite bulk samples; dashed line: linear fit to the experimental data of ZHAO et al. [Zha84] for manganese oxides; vertical dotted lines: formal Mn valences for stoichiometric $\text{La}_{0.7}\text{Ca}_{0.3}\text{MnO}_3$ and $\text{La}_{0.7}\text{Ce}_{0.3}\text{MnO}_3$, respectively. The data points are indexed according to the sample treatment steps of table 4.1. From point *a* to *f* the oxygen content is successively reduced; point *g* represents the reoxidized state.

4.2.4 Summary and outlook

This part of the thesis treated the Mn valence states of $\text{La}_{0.7}\text{Ca}_{0.3}\text{MnO}_3$ and $\text{La}_{0.7}\text{Ce}_{0.3}\text{MnO}_3$ epitaxial thin films by x-ray and ultraviolet photoelectron spectroscopy for as-cleaned surfaces as well as for different deoxygenation states. The shape of the Mn 2p doublet and the value of the Mn 3s exchange splitting turned out to be valuable indicators of the Mn valence. Both compounds were found to be in a mixed $\text{Mn}^{3+/4+}$ state after a surface cleaning procedure in an O_2 atmosphere and before any deoxygenation treatment. Heating in ultrahigh vacuum resulted in oxygen loss, which in both cases was accompanied by the transition towards a lower Mn valence between +2 and +3. For LCeMO not only the Mn valence changed, but also the Ce valence was driven from the 4+ state towards the 3+ state. The changes in the Mn and Ce valences could be reversed by heating in an oxygen atmosphere, which resulted in the reoxidation of the films. Finally, the investi-

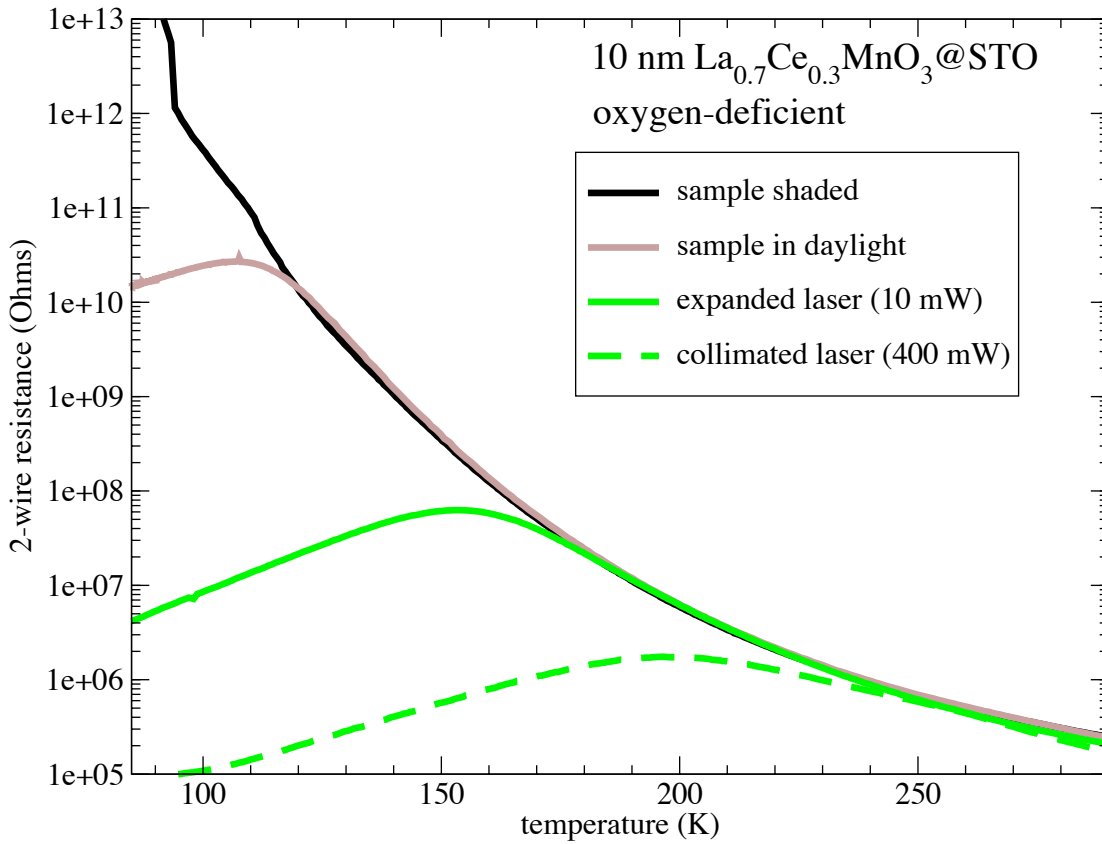


Figure 4.16: Photoconductivity of an oxygen-deficient LCeMO film. In the dark no MIT is observable in the available temperature range. Already the exposure to daylight recovers the MIT and reduces the low-temperature resistivity by several orders of magnitude. Illumination with photons from an Ar^+ laser at a wavelength of 514 nm induces an even more dramatic resistivity drop and the shift of the transition temperature to higher temperatures. At 100 K the resistivity drop reached by the available laser power is around seven orders of magnitude, which is higher than the values reported for hole-doped manganites in a few studies so far (e.g. [Gil00, Cau01, Mos04] and references therein).

gation shows that even a standard XPS experiment using nonmonochromatized x-rays is capable of determining the Mn valence state of manganite films very clearly. Therefore, the method provides an inexpensive characterization tool which can give valuable support in the process of optimizing the preparation of such films.

In general, heating in ultrahigh vacuum turned out to be a suitable method for tuning the Mn valence of lanthanum manganite thin films between a mixed $3+/4+$ state and mixed $2+/3+$ state and thus for preparing electron-doped manganite films. XPS allows monitoring the two coupled processes: the change of the oxygen content and the Mn valence change.

Ongoing investigations focus on the following open questions:

- whether the electron-doped state in LCeMO, which was prepared by heating in an ultrahigh vacuum, remains stable in air,
- whether this state is phase separated or not, and
- how the transition temperatures change after the different deoxygenation steps.

Concerning the last question, latest temperature-dependent resistivity investigations showed that a deoxygenated and thus electron-doped LCeMO film does not show a metal-insulator transition (MIT) any longer down to 77 K. The resistivity rises with decreasing temperature over the whole temperature range. Recent publications of other groups confirm this observation [Yan05a, Wan06b, Wan06a]. Astonishingly, the MIT could be recovered by illuminating the film (figure 4.16). The observed effect motivates further systematic photoconductivity studies of LCeMO with different oxygen contents, which are in progress but beyond the scope of the thesis.

5 Summary and outlook of the thesis

This concluding chapter summarizes, in a condensed form, the objectives, questions addressed, and results of the present Ph.D. thesis, and finally gives an outlook on promising further investigations.

- The thesis was dedicated to the study of the electronic properties of doped lanthanum manganite ($\text{La}_{0.7}\text{Sr}_{0.3}\text{MnO}_3$, $\text{La}_{0.7}\text{Ca}_{0.3}\text{MnO}_3$, $\text{La}_{0.7}\text{Ce}_{0.3}\text{MnO}_3$) thin films on strontium titanate (SrTiO_3), especially at the film surfaces and at the film/substrate interfaces.
- To realize those investigations, two quite different photon-based spectroscopy techniques were employed, namely:
 - x-ray and ultraviolet photoelectron spectroscopy (XPS/UPS) for studying the free surfaces, and
 - three different experimental realizations of surface photovoltage spectroscopy (SPS) for the interface investigations (but also for comparative surface studies).

While for the first technique commercial standard laboratory equipment was used, for the SPS investigations extensive instrumental developments had to be carried out first.

- Concerning the manganite film surfaces the following questions were addressed:
 - Does the substitution of La^{3+} in LaMnO_3 by a tetravalent doping ion such as Ce^{4+} create an electron-doped manganite (in contrast to the well-known hole-doped case by divalent-cation substitution)?
 - How sensitive is the degree of electron doping to the variation of the oxygen content, and can it be tuned in a defined and reversible way?
 - To what extent can the type of doping, or, in other words, the manganese valence state, be reliably determined by means of photoelectron spectroscopy?
- Concerning the manganite/strontium titanate interfaces the following questions were in the focus:

- Can this oxidic heterostructure be characterized by exploiting surface photovoltage phenomena, and which method is the most suitable one?
 - What does the energetic distribution of electronic interface defect states within the band gap of the substrate look like, if the system is modeled as a SCHOTTKY contact?
 - Can the detected defect states be classified according to their origin, i.e., are they specific to the film, or are they substrate related?
 - How straightforward is the interpretation of the data and does it allow an unambiguous evaluation of the interface quality?
- The photoelectron spectroscopy investigation, which was comparatively performed on nominally electron-doped $\text{La}_{0.7}\text{Ce}_{0.3}\text{MnO}_3$ and hole-doped $\text{La}_{0.7}\text{Ca}_{0.3}\text{MnO}_3$, lead to the following results:
 - The analysis of the Mn valence from the Mn 3s exchange splitting energy combined with the evaluation of the Mn 2p signal and the film stoichiometry, as derived from the peak areas of the strongest signals from each element, turned out to be a valuable indicator of the doping type.
 - As-prepared $\text{La}_{0.7}\text{Ce}_{0.3}\text{MnO}_3$ showed hole doping, but an electron-doped state could be prepared by defined deoxygenation through heating in ultrahigh vacuum.
 - The Mn valence and, equivalently, the degree of electron doping can be reversibly tuned by cycles of heating in either ultrahigh vacuum (deoxygenation, Mn valence decreases, film becomes more electron-doped) or in an oxygen atmosphere (reoxidation, Mn valence increases, film becomes more hole-doped). This tunability was observed not only for the nominally electron-doped $\text{La}_{0.7}\text{Ce}_{0.3}\text{MnO}_3$ film but also for the hole-doped $\text{La}_{0.7}\text{Ca}_{0.3}\text{MnO}_3$ reference film.
 - Unexpectedly, the deoxygenation of the $\text{La}_{0.7}\text{Ce}_{0.3}\text{MnO}_3$ film resulted not only in a decrease of the Mn valence, but also the Ce valence shifted from 4+ to 3+. Whether this process indicates a phase separation process remains unclear to date. However, the fact that it is also reversible by oxygenation might contradict the phase separation scenario.
 - As recent investigations have demonstrated, the $\text{La}_{0.7}\text{Ce}_{0.3}\text{MnO}_3$ films which show electron doping after deoxygenation are highly resistive and do not show the metal-insulator-transition (MIT) any longer. However, the MIT can be

recovered by illumination with visible light. Furthermore, this illumination-induced resistance drop is as large as seven orders of magnitude and is thus comparable to the colossal magnetoresistance effect. A systematic study of how the carrier concentration may be manipulated by light in hole- and electron-doped manganites is in progress now.

- The results of the surface photovoltage study of the manganite/SrTiO₃ interface must be seen as a continuous interplay between instrumental/methodological development and acquisition of knowledge on the sample system:
 - Three different surface photovoltage detection methods were checked with respect to their suitability for the manganite/SrTiO₃ interface: (i) x-ray photoelectron spectroscopy under additional optical excitation (X-SPS), (ii) capacitive SPV detection based on a parallel-plate capacitor geometry under modulated illumination (C-SPS), and (iii) the SPV measurement by a KELVIN probe (K-SPS). While the first method turned out to be less suitable due to cross coupling of x-ray-induced effects, the latter two provided detailed surface photovoltage spectra across the SrTiO₃ band gap. For K-SPS, a home-built KELVIN probe, optimized for optical applications and long-term measurements, was developed within the thesis.
 - By means of C-SPS a comparative surface photovoltage spectroscopy study of the interfaces between strontium titanate on the one side and La_{0.7}Sr_{0.3}MnO₃, La_{0.7}Ca_{0.3}MnO₃, or La_{0.7}Ce_{0.3}MnO₃ on the other side was accomplished. A map of defect states within the substrate band gap was worked out and a classification of the different states was proposed. It was shown that annealing dramatically decreases the number and density of interface states. For a definite evaluation of the interface quality by C-SPS the investigation of a much broader set of samples with systematically varied growth conditions is recommended.
 - For comparison, the pure SrTiO₃ surface without any film was analyzed by K-SPS. The wavelength-resolved SPV spectra obtained with K-SPS partially verify those trap states from C-SPS that were assumed to stem from the substrate. Time-resolved SPV measurements with the KELVIN probe (SPV transients) show that in the sub-bandgap range different trap states with very different time constants contribute to the surface photovoltage. Consequently, only the SPV as a function of both wavelength and time can provide the full information on the rich trap state dynamics.

- Now that the instrumental preconditions are available, long-term wavelength-*and* time-resolved SPV studies with K-SPS on other widely discussed (ferroic) oxidic heterostructures, such as PZT/SrTiO₃:Nb, are now in progress.
- In summary, photons were shown to be versatile, nondestructive probes of the electronic structure of several oxidic interfaces. Depending on the type of their interaction with the interface of interest, the response of the system to the probe photons may be very complex, which makes the interpretation of the experimental data a puzzling challenge.

Bibliography

- [Ahn03] AHN C H, TRISCONE J M, MANNHART J. Electric field effect in correlated oxide systems. *Nature* **424**, (2003) 1015–1018. 2
- [Amb66] AMBLER E, COLWELL J, HOSLER W, SCHOOLEY J. Magnetization and Critical Fields of Superconducting SrTiO₃. *Phys. Rev.* **148**(1), (1966) 280–286. 2.1.2
- [And55] ANDERSON P W, HASAGEWA H. Considerations on Double Exchange. *Phys. Rev.* **100**, (1955) 675–681. 2.2.1
- [Aso04] ASOKAN K, JAN J C, RAO K V R, CHIOU J W, TSAI H M, MOOKERJEE S, PONG W F, TSAI M H, KUMAR R, HUSAIN S, SRIVASTAVA J P. Electron- and hole-doping effects on the electronic structure of manganite studied by x-ray absorption spectroscopy. *J. Phys.: Condens. Matter* **16**, (2004) 3791–3799. 4.2.1
- [Att06] ATTFIELD J P. Charge ordering in transition metal oxides. *Solid State Sciences* **8**, (2006) 861–867. 4
- [Auc98] AUCIELLO O, SCOTT J F, RAMESH R. The physics of ferroelectric memories. *Physics Today* **51**(7), (1998) 22–27. 2
- [Bae66] BAER W. Free-Carrier Absorption in Reduced SrTiO₃. *Phys. Rev.* **144**(2), (1966) 734–738. 2.1.4
- [Bai89] BAIKIE I D, VAN DER WERF K O, OERBEKKE H, BROEZE J, VAN SILFHOUT A. Automatic kelvin probe compatible with ultrahigh vacuum. *Rev. Sci. Instrum.* **60**, (1989) 930–934. 17
- [Bal71] BALESTRA C L, LAGOWSKI J, GATOS H C. Determination of surface state energy positions by surface photovoltage spectrometry: CdS. *Surf. Sci.* **26**, (1971) 317–320. 3.1.1.2
- [Bäu78] BÄUERLE D, BRAUN W, SAILE V, SPRÜSSEL G, KOCH E F. Vacuum Ultraviolet Reflectivity and Band Structure of SrTiO₃ and BaTiO₃. *Z. Phys. B* **29**, (1978) 179–184. 2.1.4
- [Bed77] BEDNORZ J G, SCHEEL H J. Flame-fusion growth of SrTiO₃. *J. Cryst. Growth* **41**, (1977) 5–12. 10

- [Bed86] BEDNORZ J G, MÜLLER K A. Possible high T_c superconductivity in the Ba-La-Cu-O system. *Z. Phys. B* **64**, (1986) 189–163. 3
- [Bes76] BESOCKE K, BERGER S. Piezoelectric driven Kelvin probe for contact potential difference studies. *Rev. Sci. Instrum.* **47**, (1976) 840–842. 17
- [Bey06] BEYREUTHER E, GRAFSTRÖM S, ENG L M, THIELE C, DÖRR K. XPS investigation of Mn valence in lanthanum manganite thin films under variation of oxygen content. *Phys. Rev. B* **73**, (2006) 155425. 3.2.3.2, 4.2
- [Bha00] BHALLA A S, GUO R, ROY R. The perovskite structure - a review of its role in ceramic science and technology. *Mater. Res. Innovat.* **4**, (2000) 3–26. 2.2
- [Blo94] BLOM P W M, WOLF R M, CILLESSEN J F M, KRIJN M P C M. Ferroelectric Schottky Diode. *Phys. Rev. Lett.* **73**, (1994) 2107–2110. 3.1.2.3
- [Boe03] BOERASU I, PINTILIE L, PEREIRA M, VASILEVSKIY M I, GOMES M J M. Competition between ferroelectric and semiconductor properties in $\text{Pb}(\text{Zr}_{0.65}\text{Ti}_{0.35})\text{O}_3$ thin films deposited by sol-gel. *J. Appl. Phys.* **93**, (2003) 4776–4783. 3.1.2.2
- [Boe04] BOERASU I, PEREIRA M, GOMES M J M, WATTS B, LECCABUE F, VILARINHO P M. Structural and photoelectrical properties of Nb-doped PZT thin films deposited by pulsed laser ablation. *J. Eur. Ceram. Soc.* **24**, (2004) 1633–1636. 3.1.2.2
- [Bri82] BRILLSON L J. The structure and properties of metal-semiconductor contacts. *Surf. Sci. Rep.* **2**, (1982) 123–326. 3.1.1.1
- [Bri83] BRIGGS D, SEAH M P, eds. *Practical Surface Analysis by Auger and X-ray Photoelectron Spectroscopy*. Wiley, New York, 1983. 4.2.2, 4.2.3.1
- [Bri03] BRIGGS D, GRANT J T, eds. *Surface Analysis by Auger and X-ray Photoelectron Spectroscopy*. IM Publications and SurfaceSpectra Limited, Chichester, 2003. 4.1, 4.1.1.2, 4.4, 6, 4.2.3.1
- [Bro83] BRONSTEIN I N, SEMENDJAJEW K A. *Taschenbuch der Mathematik*. B. G. Teubner Verlagsgesellschaft, Leipzig, 1983. B.2.1
- [Can00] CANEIRO A, MORALES L, PRADO F, LAMAS D G, SACHEZ R D, SERQUIS A. Comment on "Magnetoresistance and phase composition of La-Sn-Mn-O systems". *Phys. Rev. B* **62**(10), (2000) 6825–6826. 4.2.1

- [Cap70] CAPIZZI M, FROVA A. Optical Gap of Strontium Titanate (Deviation from Urbach Tail Behavior). *Phys. Rev. Lett.* **25**(18), (1970) 1298–1302. 2.1.4
- [Car65] CARDONA M. Optical Properties and Band Structure of SrTiO₃ and BaTiO₃. *Phys. Rev.* **140**(2A), (1965) A651–A655. 2.1.4
- [Car67] CARNES J, GOODMAN A. Evaporated Metallic Contacts to Conducting Strontium Titanate Single Crystals. *Journal of Applied Physics* **38**(8), (1967) 3091–3096. 3.1.2.1
- [Cas02a] CASTELL M. Scanning tunneling microscopy of reconstructions on the SrTiO₃(001) surface. *Surf. Sci.* **505**, (2002) 1–13. 2.1.3
- [Cas02b] CASTELL M R. Nanostructures on the SrTiO₃(001) surface studied by STM. *Surf. Sci.* **516**, (2002) 33–42. 2.1.3
- [Cau01] CAURO R, GILABERT A, CONTOUR J P, LYONNET R, MEDICI M G, GRENET J C, LEIGHTON C, SCHULLER I K. Persistent and transient photoconductivity in oxygen-deficient La_{2/3}Sr_{1/3}MnO_{3-δ} thin films. *Phys. Rev. B* **63**, (2001) 174423s. 4.16
- [Cha04] CHANG W J, HSIEH C C, JUANG J Y, WU K H, UEN T M, GOU Y S, HSU C H, LIN J Y. Effects of compressive epitaxial strain on the magnetotransport properties of single-phase electron-doped La_{0.7}Ce_{0.3}MnO₃. *J. Appl. Phys.* **96**(8), (2004) 4357–4361. 4.2.1
- [Cho99a] CHOI J, DULLI H, LIOU S H, DOWBEN P A, LANGELL M A. The Influence of Surface Terminal Layer and Surface Defects on the Electronic Structure of CMR Perovskites: La_{0.65}A_{0.35}MnO₃ (A = Ca, Sr, Ba). *phys. stat. sol. (b)* **214**, (1999) 45–57. 4.2.2, 4.2.3.1, 4.2.3.2
- [Cho99b] CHOI J, ZHANG J, LIOU S H, DOWBEN P A, PLUMMER E W. Surfaces of the perovskite manganites La_{1-x}Ca_xMnO₃. *Phys. Rev. B* **59**(20), (1999) 13453–13459. 4.2.2, 4.2.3.1, 4.2.3.2
- [Cho05] CHOU H, HONG Z Y, SUN S J, JUANG J Y, CHANG W J. Strong anisotropic magnetoresistance and magnetic interaction in La_{0.7}Ce_{0.3}MnO₃/La_{0.7}Ca_{0.3}MnO₃. *J. Appl. Phys.* **97**, (2005) 10A308. 4.2.1
- [Coe99] COEY J M D, VIRET M, VON MOLNÁR S. Mixed-valence manganites. *Adv. Phys.* **48**(2), (1999) 167–293. 1, 2.2, 2.4, 2.2.4

- [Coe04] COEY M. Charge-ordering in oxides. *Nature* **430**, (2004) 155–156. 1, 4
- [Coh68] COHEN M, BLUNT R. Optical Properties of SrTiO₃ in the Region of the Absorption Edge. *Phys. Rev.* **168**(3), (1968) 929–933. 2.1.4
- [Col98] COLDEA M, NEUMANN M, LÜTKEHOFF S, MÄHL S, COLDEA R. Spin and valence fluctuations in CeMn₄Al₈ and CeMn₆Al₆. *J. Alloys Compd.* **278**, (1998) 72–79. 4.2.3.3
- [Cra99] CRANDLES D A, NICHOLAS B, DREHER C, HOMES C C, MCCONNELL A W, CLAYMAN B P, GONG W H, GREEDAN J E. Optical properties of highly reduced SrTiO_{3-x}. *Phys. Rev. B* **59**(20), (1999) 12842–12846. 11
- [Dag01] DAGOTTO E. Colossal magnetoresistant materials: The key role of phase separation. *Phys. Rep.* **344**, (2001) 1–153. 2
- [Dag05] DAGOTTO E. Complexity in Strongly Correlated Electronic Systems. *Science* **309**, (2005) 257–262. 1
- [Dav99] DAVIES P K. Cation ordering in complex oxides. *Curr. Opin. Solid State Mater. Sci.* **4**, (1999) 467–471. 2
- [Dec99] DECORSE P, CABOCHE G, DUFOUR L C. A comparative study of the surface and bulk properties of lanthanum-strontium-manganese oxides La_{1-x}Sr_xMnO_{3±δ} as a function of Sr-content, oxygen potential and temperature. *Sol. State Ion.* **117**, (1999) 161–169. 4.2.2
- [Dec01] DECORSE P, QUENNEVILLE E, POULIN S, MEUNIER M, YELON A, MORIN F. Chemical and structural characterization of La_{0.5}Sr_{0.5}MnO₃ thin films prepared by pulsed-laser deposition. *J. Vac. Sci. Technol. A* **19**(3), (2001) 910–915. 4.2.3.2
- [Ded93] DEDYK A I, LOOS G D, PAVLOVSKAYA M V, TER-MARTIROSYAN L T. Estimate of the position of the Fermi level in strontium titanate. *Phys. Solid State* **35**(11), (1993) 1564–1566. 2.1.5, 3.4, 4
- [Del05] DELIMOVA L A, GREKHOV I V, MASHOVETS D V, TYAGINOV S E, SHIN S, KOO J M, KIM S P, PARK Y. Transient-current measurement of the trap charge density at interfaces of a thin-film metal/ferroelectric/metal structure. *Appl. Phys. Lett.* **87**, (2005) 192101. 3.1.2.3

- [Dem04] DEMKOV A A, FONSECA L R C, TOMFOHR J, SANKEY O F. The band alignment problem at the Si-high-k dielectric interface. *Mat. Res. Soc. Symp. Proc.* **786**, (2004) E5.6.1–E5.6.6. 3.1.2.1
- [Dix73] DIX M J, WOOD R, SLATER D H. An integrated, high vacuum, beam modulation device. *J. Phys. E: Sci. Instrum.* **6**, (1973) 1099–1100. 17, 3.2.4.2
- [Dör00] DÖRR K, DE TERESA J M, MÜLLER K H, ECKERT D, WALTER T, VLAKHOV E, NENKOV K, SCHULTZ L. Preparation and properties of epitaxial $\text{La}_{0.7}\text{Ca}_{0.3}\text{MnO}_{3-\delta}$ films with reduced carrier density. *J. Phys.: Condens. Matter* **12**, (2000) 7099–7109. 4.2.2
- [Dör06] DÖRR K. Ferromagnetic manganites: spin-polarized conduction versus competing interactions. *J. Phys. D: Appl. Phys.* **39**, (2006) R125–R150. 2.2, 2.2.3, 2.4, 2.2.4
- [Dul00] DULLI H, DOWBEN P A, LIOU S H, PLUMMER E W. Surface segregation and restructuring of colossal-magnetoresistent manganese perovskites $\text{La}_{0.65}\text{Sr}_{0.35}\text{MnO}_3$. *Phys. Rev. B* **62**(22), (2000) R14629–R14632. 4.2.2
- [Edw02] EDWARDS D. Ferromagnetism and electron-phonon coupling in the manganites. *Adv. Phys.* **51**(5), (2002) 1259–1318. 2.2, 2.2.4
- [Eer06] EERENSTEIN W, MATHUR N D, SCOTT J F. Multiferroic and magnetoelectric materials. *Nature* **442**, (2006) 759–765. 2, 2
- [Fau71] FAUGHNAN B W. Photochromism in Transition-Metal-Doped SrTiO_3 . *Phys. Rev. B* **4**(10), (1971) 3623–3636. 2.1.2
- [Fre64] FREDERIKSE H P R, THURBER W R, HOSLER W R. Electronic Transport in Strontium Titanate. *Phys. Rev.* **134**(2A), (1964) A442–A445. 2.1.5
- [Fry03] FRYE A, FRENCH R H, BONNELL D A. Optical properties and electronic structure of oxidized and reduced single-crystal strontium titanate. *Z. Metallkd.* **94**, (2003) 226–232. 2.1.4
- [Fug83] FUGGLE J C, HILLENBRECHT F U, ZOLNIEREK Z, LÄSSER R, FREIBURG C, GUNNARSSON O, SCHÖNHAMMER K. Electronic structure of Ce and its intermetallic compounds. *Phys. Rev. B* **27**(12), (1983) 7330–7341. 4.2.3.3

- [Fuj03] FUJISAWA H, SUGATA M, SHIMIZU M, NIU H. Characterization of MOCVD-TiO₂ and ZrO₂ Insulating Layers in MIFS Structures by DLTS and ICTS Methods. *J. Kor. Phys. Soc.* **42**, (2003) S1354–S1356. 3.1.2.3
- [Fuj05] FUJII T, KAWASAKI M, SAWA A, AKOH H, KAWAZOE Y, TOKURA Y. Hysteretic current-voltage characteristics and resistance switching at an epitaxial oxide Schottky junction SrRuO₃/SrTi_{0.99}Nb_{0.01}O₃. *Appl. Phys. Lett.* **86**, (2005) 012107. 3.1.2.3
- [Gaj07] GAJEK M, BIBES M, FUSIL S, BOUZEHOUE K, FONTCUBERTA J, BARTHELEMY A, FERT A. Tunnel junctions with multiferroic barriers. *Nature Materials* **6**, (2007) 296–302. 2.2.3
- [Gal02] GALAKHOV V R, DEMETER M, BARTKOWSKI S, NEUMANN M, OVECHKINA N A, KURMAEV E Z, LOBACHEVSKAYA N I, MUKOVSKII Y M, MITCHELL J, EDERER D. Mn 3s exchange splitting in mixed-valence manganites. *Phys. Rev. B* **65**, (2002) 113102. 4.2.2, 4.2.2, 4.2.3.6, 4.2.3.6, 4.15
- [Gan59] GANDY H W. Optical Transmission of Heat-Treated Strontium Titanate. *Phys. Rev.* **113**(3), (1959) 795–800. 2.1.4
- [Gan00] GANGULY R, GOPALAKRISHNAN I K, YAKHMI J V. Does the LaMnO₃ phase accept Ce-doping? *J. Phys.: Condens. Matter* **12**, (2000) L719–L722. 4.2.1
- [Gao03] GAO J, DAI S Y, LI T K. Electronic states of epitaxial thin films of La_{0.9}Sn_{0.1}MnO₃ and La_{0.9}Ca_{0.1}MnO₃. *Phys. Rev. B* **67**, (2003) 153403. 4.2.1, 4.2.3.5
- [Gat73] GATOS H, LAGOWSKI J. Surface Photovoltage Spectroscopy - A New Approach to the Study of High-Gap Semiconductor Surfaces. *J. Vac. Sci. Technol.* **10**(1), (1973) 130–135. 3.1.1
- [Gay04] GAYONE J E, ABBATE M, ALEJANDRO G, LAMAS D G, TOVAR M, ZAMPIERI G. Ce valence in La_{0.47}Ce_{0.20}Ca_{0.33}MnO₃. *J. Alloys Compd.* **369**, (2004) 252–255. 4.2.1
- [Geb99] GEBHARDT J R, ROY S, ALI N. Colossal magnetoresistance in Ce doped manganese oxides. *J. Appl. Phys.* **85**(8), (1999) 5390–5392. 4.2.1
- [Gen60] DE GENNES P G. Effects of Double Exchange in Magnetic Crystals. *Phys. Rev.* **118**, (1960) 141–154. 2.2.1

- [Ger87] GERMANOVA K, HARDALOV C, STRASHILOV V, GEORGIEV B. An improved apparatus for surface photovoltage studies with a bimorphous piezoelectric Kelvin probe. *J. Phys. E: Sci. Instrum.* **20**, (1987) 273–276. 17
- [Ger89] GERMANOVA K, NIKOLOV L, HARDALOV C. Highly sensitive automated setup for measuring surface photovoltage spectra. *Rev. Sci. Instrum.* **60**, (1989) 746–748. 17
- [Gil00] GILABERT A, CAURO R, MEDICI M G, GRENET J C, WANG H S, HU Y F, LI Q. Photoconductivity in manganites. *J. Supercond.* **13**, (2000) 285–290. 4.16
- [Gol87] GOLDSCHMIDT D, TULLER H L. Fundamental absorption edge of SrTiO₃ at high temperatures. *Phys. Rev. B* **35**, (1987) 4360–4364. 2.1.4
- [Gor04] GOR'KOV L P, KRESIN V Z. Mixed-valence manganites: fundamentals and main properties. *Phys. Rep.* **400**, (2004) 149–208. 2.2, 2.2.4
- [Gun83] GUNNARSSON O, SCHÖNHAMMER K. Electron spectroscopies for Ce compounds in the impurity model. *Phys. Rev. B* **28**(8), (1983) 4315–4341. 4.2.3.3
- [Guo00] GUO X, DAI S, ZHOU Y, CHEN Z, YANG G, LIU F, IBRAHIM K, QIAN H. Study of colossal magnetoresistance material La-Sn-Mn-O epitaxial films. *Mat. Sci. Engin. B* **76**, (2000) 18–21. 4.2.1
- [Guo03] GUO X G, CHEN X S, SUN Y L, SUN L Z, ZHOU X H, LU W. Electronic band structure of Nb doped SrTiO₃ from first principles calculation. *Phys. Lett. A* **317**, (2003) 501–506. 2.1.4
- [Had95] HADJADJ A, ROCA I CABARROCAS P, EQUER B. Analytical compensation of stray capacitance effect in Kelvin probe measurements. *Rev. Sci. Instrum.* **66**, (1995) 5272–5276. 17, 3.2.4.1
- [Hag05] HAGUE J P. Suppression of Mott-Hubbard states and metal-insulator transitions in the two-band Hubbard model. *J. Phys.: Condens. Matter* **17**, (2005) 1385–1397. 5
- [Han04a] HAN S W, LEE J D, KIM K H, MITRA C, JEONG J I, KIM K J, MIN B I, KIM J H, WI S C, KANG J S. Electronic structure of La_{0.7}Ce_{0.3}MnO₃ thin film. *phys. stat. sol. (b)* **241**(7), (2004) 1577–1580. 4.2.1

- [Han04b] HAN S W, LEE J D, KIM K H, MITRA C, JEONG J I, KIM K J, MIN B I, KIM J H, WI S C, KANG J S. Photoemission and x-ray absorption spectroscopy study of electron-doped colossal magnetoresistive manganite $\text{La}_{0.7}\text{Ce}_{0.3}\text{MnO}_3$ films. *Phys. Rev. B* **69**, (2004) 104406. 4.2.1
- [Har84] HARRIS L B, FIASSON J. Vibrating capacitor measurement of surface charge. *J. Phys. E: Sci. Instrum.* **17**, (1984) 788–792. 17
- [Hea91] HEAVENS O S. *Optical properties of thin solid films*. Dover Publications, Inc., New York, 1991. A.1
- [Hec90] HECHT M. Role of photocurrent in low-temperature photoemission studies of Schottky-barrier formation. *Phys. Rev. B* **41**(11), (1990) 7918–7921. 3.2.2.2
- [Hei02] HEIFEITS E, EGLITIS R I, KOTOMIN E A, MAIER J, BORSTEL G. First-principles calculations for SrTiO_3 surface structure. *Surf. Sci.* **513**, (2002) 211–220. 2.1.3
- [Hel93] VON HELMHOLT R, WECKER R, HOLZAPFEL B, SCHULTZ L, SAMWER K. Giant negative magnetoresistance in perovskitelike $\text{La}_{2/3}\text{Ba}_{1/3}\text{MnO}_x$ ferromagnetic films. *Phys. Rev. Lett.* **71**, (1993) 2331–2334. 2.2.1, 2.3
- [Hen78] HENRICH V, DRESSELHAUS G, ZEIGER H. Surface defects and electronic structure of SrTiO_3 surfaces. *Phys. Rev. B* **17**(12), (1978) 4908–4921. 2.1.3, 3.1.2.1, 3.2.3.2, 3.2.3.2
- [HG03] HAGHIRI-GOSNET A M, RENARD J P. CMR manganites: physics, thin films and devices. *J. Phys. D: Appl. Phys.* **36**(8), (2003) R127–R150. 2.2, 2.2.4
- [Hig00] HIGUCHI T, TSUKAMOTO T, KOBAYASHI K, ISHIWATA Y, M-FUJISAWA, YOKOYA T, YAMAGUCHI S, SHIN S. Electronic band structure in the band gap of lightly doped SrTiO_3 by high-resolution x-ray absorption spectroscopy. *Phys. Rev. B* **61**, (2000) 12860–12863. 2.1.4
- [Hil00] HILL N A. Why Are There so Few Magnetic Ferroelectrics? *J. Phys. Chem. B* **104**, (2000) 6694–6709. 2
- [Höl74] HÖLZL J, SCHRAMMEN P. A New Pendulum Device to Measure Contact Potential Differences. *Appl. Phys.* **3**, (1974) 353–357. 17

- [How78] HOWNG W Y, THORN R J. The multicomponent structure of the 4d orbital in X-ray photoelectron spectra of the Lanthanum(III) ion. *Chem. Phys. Lett.* **56**(3), (1978) 463–465. 4.6
- [Hu81] HU H K, RABALAIS J W. Chemisorption and the initial stage of oxidation on Mn. *Surf. Sci.* **107**, (1981) 376–390. 4.2.3.5
- [Hüf85] HÜFNER S. Mott Insulation in Transition Metal Compounds. *Z. Phys. B* **61**, (1985) 135–138. 16
- [Hüf05] HÜFNER S, SCHMIDT S, REINERT F. Photoelectron spectroscopy - An overview. *Nucl. Instrum. Methods Phys. Res., Sect. A* **547**, (2005) 8–23. 4.1, 4.1
- [Hun97] HUNDLEY M F, NEUMEIER J J. Thermoelectric power of $\text{La}_{1-x}\text{Ca}_x\text{MnO}_{3+\delta}$: Inadequacy of the nominal $\text{Mn}^{3+/4+}$ valence approach. *Phys. Rev. B* **55**(17), (1997) 11511–11515. 4.2.1
- [Hun06] HUNTER D, LORD K, WILLIAMS T M, ZHANG K, PRADHAN A K, SAHU D R, HUANG J L. Junction characteristics of SrTiO_3 or BaTiO_3 on p-Si (100) heterostructures. *Appl. Phys. Lett.* **89**, (2006) 092102. 3.1.2.1
- [Jin94] JIN S, TIEFEL T H, MCCORMACK M, FASTNACHT R A, RAMESH R, CHEN L H. Thousandfold Change in Resistivity in Magnetoresistive La-Ca-Mn-O Films. *Science* **264**, (1994) 413–415. 2.2.1
- [Joh58] JOHNSON E. Large-Signal Surface Photovoltage Studies with Germanium. *Phys. Rev.* **111**(1), (1958) 153–166. 3.1.1
- [Joh04] JOHNSTON K, CASTELL M R, PAXTON A T, FINNIS M W. $\text{SrTiO}_3(001)(2\times 1)$ reconstructions: First-principles calculations of surface energy and atomic structure compared with scanning tunneling microscopy images. *Phys. Rev. B* **70**, (2004) 085415. 2.1.3
- [Jon50] JONKER G H, VAN SANTEN J H. Ferromagnetic compounds of manganese with perovskite structure. *Physica* **16**, (1950) 337–349. 2.2.1
- [Jon03] DE JONG M P, DEDIU V A, TALIANI C, SALANECK W R. Electronic structure of $\text{La}_{0.7}\text{Sr}_{0.3}\text{MnO}_3$ thin films for hybrid organic/inorganic spintronics applications. *J. Appl. Phys.* **94**(11), (2003) 7292–7296. 4.2.2

- [Jon05] DE JONG M P, BERGENTI I, DEDIU V A, FAHLMANN A, MARSI M, TALIANI C. Evidence for Mn^{2+} ions at surfaces of $\text{La}_{0.7}\text{Sr}_{0.3}\text{MnO}_3$. *Phys. Rev. B* **71**, (2005) 014434. 4.2.1
- [Jos02] JOSEPH JOLY V L, JOY P A, DATE S K. Studies on the effect of substitution of tetravalent ions for La^{3+} in LaMnO_3 . *J. Magn. Magn. Mat.* **247**, (2002) 316–323. 4.2.1
- [Kah64] KAHN A H, LEYENDECKER A J. Electronic Energy Bands in Strontium Titanate. *Phys. Rev.* **135**(5A), (1964) A1321–A1325. 2.1.4, 2.1.5
- [Kan01] KANG J S, KIM Y J, OLSON C G, MIN B I. The valence state of Ce in electron-doped manganites: $\text{La}_{0.7}\text{Ce}_{0.3}\text{MnO}_3$. *J. Phys.: Condens. Matter* **13**, (2001) 3779–3789. 4.2.3.5
- [Kan05] KAN D, TERASHIMA T, KANDA R, MASUNO A, TANAKA K, CHU S, KAN H, ISHIZUMI A, KANMITSU Y, SHIMAKAWA Y, TAKANO M. Blue-light emission at room temperature from Ar^+ -irradiated SrTiO_3 . *Nature Materials* **4**, (2005) 816–819. 2.1.4
- [Kan06] KAN D, KANDA R, KANEMITSU Y, SHIMIKAWA Y, TAKANO M, TERASHIMA T, ISHIMIZU A. Blue luminescence from electron-doped SrTiO_3 . *Appl. Phys. Lett.* **88**, (2006) 191916. 2.1.4
- [Kaw94] KAWASAKI M, TAKAHASHI K, MAEDA T, TSUCHIYA R, SHINOHARA M, ISHIYAMA O, YONEZAWA T, YOSHIMOTO M, KOINUMA H. Atomic Control of the SrTiO_3 Crystal Surface. *Science* **266**, (1994) 1540–1542. 2.1.3
- [Kel98] KELVIN L. Contact Electricity of Metals. *Phil. Mag.* **46**, (1898) 82–120. 3.2.4
- [Ker84] KEROACK D, LEPINE Y, BREBNER J L. Drift mobility measurements of small-polaron transport in SrTiO_3 . *J. Phys. C: Solid State Phys.* **17**, (1984) 833–842. 2.1.5, 13
- [Kho88] KHOLKIN A L, KUCHIS E V, TREPAAKOV V A. On the charge transport mechanisms in high-resistive SrTiO_3 crystals. *Ferroelectrics* **83**, (1988) 135–139. 2.1.5
- [Kho98] KHOLKIN A, BOIARKINE O, SETTER N. Transient photocurrents in lead zirconate titanate thin films. *Appl. Phys. Lett.* **72**, (1998) 130–132. 3.1.2.2

- [Kow00] KOWALCZYK A, ŚLEBARSKI A, SZAJEK A, BASZYŃSKI J, WINIARSKI A. X-ray photoemission spectra of $\text{La}_{0.7}\text{Sr}_{0.3}\text{MnO}_3$ perovskite. *J. Magn. Magn. Mat.* **212**, (2000) 107–111. 4.2.2
- [Kro99] KRONIK L, SHAPIRA Y. Surface photovoltage phenomena: theory, experiment, and applications. *Surf. Sci. Rep.* **37**, (1999) 1–206. 4, 3.1.1, 3.2.3.2, 3.2.4
- [Kro01] KRONIK L, SHAPIRA Y. Surface photovoltage spectroscopy of semiconductor structures: at the crossroads of physics, chemistry and electrical engineering. *Surf. Interface Anal.* **31**, (2001) 954–965. 3.1.1
- [Kur69] KURTIN S, MCGILL T C, MEAD C A. Fundamental transition in the electronic nature of solids. *Phys. Rev. Lett.* **22**(26), (1969) 1433–1436. 3.1.2.1
- [Kwo00] KWOK R. XPSPEAK 4.1, 2000. <http://www.phy.cuhk.edu.hk/~surface/XPS-PEAK/>. 4.2.2
- [Lag92] LAGOWSKI J, EDELMAN P, DEXTER M, HENLEY W. Non-contact mapping of heavy metal contamination for silicon IC fabrication. *Semicond. Sci. Technol.* **7**, (1992) A182–A192. 3.1.1
- [Lag94] LAGOWSKI J. Semiconductor surface spectroscopies: the early years. *Surf. Sci.* **299/300**, (1994) 92–101. 3.1.1
- [Läg99] LÄGEL B, BAIKIE I D, PETERMANN U. A novel detection system for defects and chemical contamination in semiconductors based upon the Scanning Kelvin Probe. *Surf. Sci.* **433-435**, (1999) 622–626. 3.2.4.2
- [Lee75] LEE C, DESTRY J, BREBNER J. Optical absorption and transport in semiconducting SrTiO_3 . *Phys. Rev. B* **11**(6), (1975) 2299–2310. 11
- [Lee01] LEE B W, SEO K Y, KIM Y J, HAN H, LEE H H, HAN J C, PARK S Y, KIM C S. Phase transitions in $\text{La}_{1-x}\text{Ce}_x\text{MnO}_3$ ($x = 0.2, 0.3, 0.4$). *J. Magn. Magn. Mat.* **226-230**, (2001) 803–805. 4.2.1
- [Lee03] LEE J S, KIM Z G, PARK Y D, NORTON D P, THEODOROPOULOU N A, HEBARD A F, BUDAI J D, BOATNER L A, PEARTON S J, WILSON R G. Magnetic properties of Co and Mn-implanted BaTiO_3 , SrTiO_3 and KTaO_3 . *Solid-State Electron.* **47**, (2003) 2225–2230. 2.1.2
- [Leo86] LEONELLI R, BREBNER J L. Time-resolved spectroscopy of the visible emission band in strontium titanate. *Phys. Rev. B* **33**, (1986) 8649–8656. 2.1.4

- [Lev55] LEVIN S B, FIELD N J, PLOCK F M, MERKER L. Some Optical Properties of Strontium Titanate Crystal. *J. Opt. Soc. Am.* **45**(9), (1955) 737–739. 2.1.4
- [Li98] LI Z, ZHU J, WU C, TANG Z, KAWAZOE Y. Relaxations of TiO₂- and SrO-terminated SrTiO₃(001) surfaces. *Phys. Rev. B* **58**(12), (1998) 8075–8078. 2.1.3
- [Li99] LI Z W, MORRISH A H, JIANG J Z. Magnetoresistance and phase composition of La-Sn-Mn-O systems. *Phys. Rev. B* **60**(14), (1999) 10284–10290. 4.2.1
- [Lia93] LIANG J J, WENG H S. Catalytic Properties of La_{1-x}Sr_xBO₃ (B = Mn, Fe, Co, Ni) for Toluene Oxidation. *Ind. Eng. Chem. Res.* **32**, (1993) 2563–2573. 4.2.2, 4.2.3.2
- [Lia94] LIANG Y, BONNELL D A. Structures and chemistry of the annealed SrTiO₃(001) surface. *Surf. Sci.* **310**, (1994) 128–134. 2.1.3
- [Lid01] LIDE D R, ed. *CRC Handbook of Chemistry and Physics*. CRC Press, Boca Raton, 81 ed., 2001. 4.2.2
- [Lin53] LINZ A. Some Electrical Properties of Strontium Titanate. *Phys. Rev.* **91**(3), (1953) 753–754. 12
- [Lin04] LIN J W, CHANG W J, JUANG J Y, WEN T M, WU K H, GOU Y S, LEE J M, CHEN J M. Spectroscopic evidence of electron doping in La_{0.7}Ce_{0.3}MnO₃. *J. Magn. Magn. Mat.* **282**, (2004) 237–239. 4.2.1
- [Lüt98] LÜTH H. *Surfaces and Interfaces of Solid Materials*. Springer-Verlag, Berlin, 3rd ed., 1998. 4.1, 4.1.1.2
- [Mal72] MALTBY J R, REED C E, SCOTT C G. An improved apparatus for clean surface studies of high resistivity photoconductors. *J. Phys. E: Sci. Instrum.* **5**, (1972) 584–586. 17
- [Man97] MANDAL P, DAS S. Transport properties of Ce-doped RMnO₃ (R=La, Pr, and Nd) manganites. *Phys. Rev. B* **56**(23), (1997) 15073–15080. 4.2.1
- [Man05] MANNHART J, SCHLOM D G. Oxide - Tausendsassas für die Elektronik. *Physik Journal* **4**(6), (2005) 45–51. 2
- [Mat72] MATTHEISS L. Energy Bands for KNiF₃, SrTiO₃, KMoO₃, and KTaO₃. *Phys. Rev. B* **6**(12), (1972) 4718–4740. 2.1.4

- [Mau06] MAURICE J L, IMHOFF D, CONTOUR J P, COLLIEX C. Interfaces in {100} epitaxial heterostructures of perovskite oxides. *Phil. Mag.* **86**, (2006) 2127–2146. 3
- [Mav78] MAVROIDES J G, KOLESAR D F. Surface photovoltage experiments on SrTiO₃ electrodes. *J. Vac. Sci. Technol.* **15**(2), (1978) 538–541. 3.1.2.1, 3.2.3.1
- [Mil05] MILWARD G C, CALDERON M J, LITTLEWOOD P B. Electronically soft phases in manganites. *Nature* **433**, (2005) 607–610. 2
- [Min01] MIN B I, KWON S K, LEE B W, KANG J S. Electronic structures of electron-doped manganite: La_{0.7}Ce_{0.3}MnO₃. *J. Electron Spectrosc. Rel. Phenom.* **114-116**, (2001) 801–805. 4.2.1
- [Mit81] MITSUI T, NOMURA S. Ferroelectric and Related Substances, Oxides. In *Landolt-Börnstein*, vol. III/16a. Springer, 1981. 2.1.5
- [Mit01a] MITRA C, RAYCHAUDHURI P, DHAR S K, NIGAM A K, PINTO R. Formation of epitaxial and polycrystalline films of the electron doped system La_{1-x}Ce_xMnO₃ through pulsed laser deposition. *J. Magn. Magn. Mat.* **226-230**, (2001) 809–811. 4.2.1
- [Mit01b] MITRA C, RAYCHAUDHURI P, JOHN J, DHAR S K, NIGAM A K, PINTO R. Growth of epitaxial and polycrystalline thin films of the electron doped system La_{1-x}Ce_xMnO₃ through pulsed laser deposition. *J. Appl. Phys.* **89**(1), (2001) 524–530. 4.2.1
- [Mit01c] MITRA C, RAYCHAUDHURI P, KÖBERNIK G, DÖRR K, MÜLLER K H, SCHULTZ L, PINTO R. *p-n* diode with hole- and electron-doped lanthanum manganites. *Appl. Phys. Lett.* **79**(15), (2001) 2408–2410. 4.2.1
- [Mit03a] MITRA C, HU Z, RAYCHAUDHURI P, WIRTH S, CSISZAR S I, HSIEH H H, LIN H J, CHEN C T, TJENG L H. Direct observation of electron doping in La_{0.7}Ce_{0.3}MnO₃ using x-ray absorption spectroscopy. *Phys. Rev. B* **67**, (2003) 092404. 4.2.1
- [Mit03b] MITRA C, RAYCHAUDHURI P, DÖRR K, MÜLLER K H, SCHULTZ L, OP-PENEER P M, WIRTH S. Observation of Minority Spin Character of the New Electron Doped Manganite La_{0.7}Ce_{0.3}MnO₃ from Tunneling Magnetoresistance. *Phys. Rev. Lett.* **90**(1), (2003) 017202. 4.2.1

- [Miy01] MIYAGI T, OGAWA T, KAMEI M, WADA Y, MITSUHASHI T, YAMAZAKI A, OHTA E, SATO T. Deep Level Transient Spectroscopy Analysis of an Anatase Epitaxial Film Grown by Metal Organic Vapor Deposition. *Jpn. J. Appl. Phys.* **40**, (2001) L404–L406. 3.1.2.3
- [Moc05] MOCHIZUKI S, FUJISHIRO F, MINAMI S. Photoluminescence and reversible photo-induced spectral change of SrTiO₃. *J. Phys.: Condens. Matter* **17**, (2005) 923–948. 2.1.4
- [Mor98] MORI S, CHEN C H, CHEONG S. Pairing of charge-ordered stripes in (La,Ca)MnO₃. *Nature* **392**, (1998) 473–476. 4
- [Mor99] MOREO A, YUNOKI S, DAGOTTO E. Phase Separation Scenario for Manganese Oxides and Related Materials. *Science* **283**, (1999) 2034–2040. 2.2.4
- [Mor06] MOREO A. Complexity in transition metal oxides. *J. Phys. Chem. Solids* **67**, (2006) 32–36. 1
- [Mos04] MOSHNYAGA V, GISKE A, SAMWER K, MISHINA E, TAMURA T, NAKABAYASHI S, BELENCHUK A, SHAPOVAL O, KULYUK L. Giant negative photoconductivity in La_{0.7}Ca_{0.3}MnO₃ thin films. *J. Appl. Phys.* **95**, (2004) 7360–7362. 4.16
- [Mui79] MUILENBERG G E, ed. *Handbook of X-ray photoelectron spectroscopy*. Perkin-Elmer Corporation, Eden Prairie, Minnesota, 1979. 4.2.3.1, 4.2.3.4, 4.11
- [Mül79] MÜLLER K A, BURKARD H. SrTiO₃: An intrinsic quantum paraelectric below 4 K. *Phys. Rev. B* **19**, (1979) 3593–3602. 2.1.1
- [Mul98] MULLINS D R, OVERBURY S H, HUNTLEY D R. Electron spectroscopy of single crystal and polycrystalline cerium oxide surfaces. *Surf. Sci.* **409**, (1998) 307–319. 4.2.3.3
- [Mur04] MURAMATSU T, MURAOKA Y, HIROI Z. Photocarrier injection and the I-V characteristics of La_{0.8}Sr_{0.2}MnO₃/SrTiO₃:Nb heterojunctions. *Solid State Commun.* **132**, (2004) 351–354. 3.1.2.2
- [Nab03] NABOKIN P I, SOUBTEL D, BALBASHOW A M. Floating zone growth of high-quality SrTiO₃ single crystals. *J. Cryst. Growth* **250**, (2003) 397–404. 10

- [Nas88] NASSAU K, MILLER A E. Strontium titanate: An index to the literature on properties and the growth of single crystals. *J. Cryst. Growth* **91**, (1988) 373–381. 10
- [Nel00] NELSON A J, REYNOLDS J G, ROOS J W. Core-level satellites and outer core-level multiplet splitting in Mn model compounds. *J. Vac. Sci. Technol. A* **18**(4), (2000) 1072–1076. 4.2.2, 4.2.3.5
- [Nev72] NEVILLE R C, MEAD C A. Surface barrier energies on strontium titanate. *J. Appl. Phys.* **43**(11), (1972) 4657–4663. 3.1.2.1
- [Nev75] NEVILLE R, HOENEISEN B. Anomalous capacitance of Schottky barriers on strontium titanate. *J. Appl. Phys.* **46**(1), (1975) 350–353. 3.1.2.1
- [Nog04] NOGUERA C, FINOCCHI F, GONIAKOWSKI J. First principles studies of complex oxide surfaces and interfaces. *J. Phys.: Condens. Matter* **16**, (2004) S2509–S2537. 1
- [Nol54] NOLAND J A. Optical Absorption of Single-Crystal Strontium Titanate. *Phys. Rev.* **94**(3), (1954) 724. 2.1.4
- [O’B93] O’BRIEN M C M, CHANCEY C C. The Jahn-Teller effect: An introduction and current review. *Am J. Phys.* **61**, (1993) 688–697. 17
- [Oht02] OHTOMO A, MULLER D, GRAZUL J, HWANG H. Artificial charge-modulation in atomic-scale perovskite titanate superlattices. *Nature* **419**, (2002) 378–380. 2
- [Oht04] OHTOMO A, HWANG H. A high-mobility electron gas at the LaAlO₃/SrTiO₃ heterointerface. *Nature* **427**, (2004) 423–426. 9
- [Oka04] OKAMOTO S, MILLIS A J. Electronic reconstruction at an interface between a Mott insulator and a band insulator. *Nature* **428**, (2004) 630–633. 9
- [Oku75] OKU M, HIROKAWA K, IKEDA S. X-ray photoelectron spectroscopy of manganese-oxygen systems. *J. Electron Spectrosc. Relat. Phenom.* **7**, (1975) 465–473. 4.2.3.5
- [Opi57] OPIK U, PRYCE M H L. Studies of the Jahn-Teller Effect. I. A Survey of the Static Problem. *Proc. R. Soc. Lond. Ser. A - Math. Phys. Sci.* **238**, (1957) 425–447. 2.2.1

- [Ore00] ORENSTEIN J, MILLIS A J. Advances in the physics of high-temperature superconductivity. *Science* **288**, (2000) 468–474. 3
- [Pal91] PALIK E D, ed. *Handbook of Optical Constants of Solids*. Academic Press, San Diego, CA, 1991. A.1
- [Par06] PARUCH P, GIAMARCHI T, TYBELL T, TRISCONE J M. Nanoscale studies of domain wall motion in epitaxial ferroelectric thin films. *J. Appl. Phys.* **100**, (2006) 051608. 2
- [Pea04] PEARTON S J, HEO W H, IVILL M, NORTON D P, STEINER T. Dilute magnetic semiconducting oxides. *Semicond. Sci. Technol.* **19**, (2004) R59–R74. 2
- [Pea05] PEARTON S J, NORTON D P, FRAZIER R, HAN S Y, ABERNATHY C R, ZAVADA J M. Spintronics device concepts. *IEE Proc.-Circuits Devices Syst.* **152**(4), (2005) 312–322. 8
- [Pei01] PEISLER E J, MARSH O J, BEACH R A, MCGILL T C. Stability of cerium oxide on silicon studied by x-ray photoelectron spectroscopy. *J. Vac. Sci. Technol. B* **19**(4), (2001) 1611–1618. 4.2.3.3
- [Phi99] PHILIP J, KUTTY T R N. Effect of valence fluctuations in A sites on the transport properties of $\text{La}_{1-x}\text{R}_x\text{MnO}_3$ ($\text{R} = \text{Ce}, \text{Pr}$). *J. Phys.: Condens. Matter* **11**, (1999) 8537–8546. 4.2.1
- [Pol82] POLLERT E, KRUPICKA S, KUZMICOVA E. Structural study of $\text{Pr}_{1-x}\text{Ca}_x\text{MnO}_3$ and $\text{Y}_{1-x}\text{Ca}_x\text{MnO}_3$ perovskites. *J. Phys. Chem. Solids* **43**, (1982) 1137–1145. 2.2.1
- [Pon00] PONCE S, PEÑA M A, FIERRO J L G. Surface properties and catalytic performance in methane combustion of Sr-substituted lanthanum manganites. *Appl. Cat. B* **24**, (2000) 193–205. 4.2.2, 4.2.3.2
- [Pow76] POWELL R A, SPICER W E. Photoemission investigation of surface states on strontium titanate. *Phys. Rev. B* **13**(6), (1976) 2601–2604. 2.1.3, 3.1.2.1
- [Ram97] RAMIREZ A. Colossal magnetoresistance. *J. Phys.: Condens. Matter* **9**(39), (1997) 8171–8199. 2.2, 2.2.4, 2.5
- [Ram07] RAMESH R, SPALDIN N A. Multiferroics: progress and prospects in thin films. *Nature Materials* **6**, (2007) 21–29. 2

- [Rau02] RAUER R, BÄCKSTRÖM J, BUDELMANN D, KURFISS M, SCHILLING M, RÜBHAUSEN M, WALTER T, DÖRR K, COOPER S. Thickness dependent phase separation in $\text{La}_{0.7}\text{Ca}_{0.3}\text{MnO}_3$ films. *Appl. Phys. Lett.* **81**(20), (2002) 3777–3779. A.1
- [Rau04] RAUER R. Dielectric functions of $\text{La}_{0.7}\text{Ce}_{0.3}\text{MnO}_3$ and $\text{La}_{0.7}\text{Sr}_{0.3}\text{MnO}_3$ films. Unpublished data, 2004. A.1
- [Rau06] RAUER R, RÜBHAUSEN M, DÖRR K. Magnetic-order induced spectral-weight redistribution in $\text{La}_{0.7}(\text{Sr,Ca})_{0.3}\text{MnO}_3$. *Phys. Rev. B* **73**, (2006) 092402. 16
- [Ray99] RAYCHAUDHURI P, MUKHERJEE S, NIGAM A K, JOHN J, VAISNAV U D, PINTO R, MANDAL P. Transport and magnetic properties of laser ablated $\text{La}_{0.7}\text{Ce}_{0.3}\text{MnO}_3$ films on LaAlO_3 . *J. Appl. Phys.* **86**(10), (1999) 5718–5725. 4.2.1
- [Ray03] RAYCHAUDHURI P, MITRA C, MANN P D A, WIRTH S. Phase diagram and Hall effect of the electron doped manganite $\text{La}_{1-x}\text{Ce}_x\text{MnO}_3$. *J. Appl. Phys.* **93**(10), (2003) 8328–8330. 2.6, 4.2.1
- [Red72] REDFIELD D, BURKE W. Fundamental Absorption Edge of SrTiO_3 . *Phys. Rev. B* **6**(8), (1972) 3104–3109. 2.1.4
- [Rei84] REIHL B, BEDNORZ J G, MÜLLER K A, JUGNET Y, LANDGREN G, MORAR J F. Electronic structure of strontium titanate. *Phys. Rev. B* **30**(2), (1984) 803–806. 2.1.4
- [Ren02] RENNER C, AEPPLI G, KIM B G, SOH Y A, CHEONG S W. Atomic-scale images of charge ordering in a mixed-valence manganite. *Nature* **416**, (2002) 518–521. 4
- [Rie07] RIEDL T, GEMMING T, GRUNER W, ACKER J, WETZIG K. Determination of manganese valency in $\text{La}_{1-x}\text{Sr}_x\text{MnO}_3$ using ELNES in the (S)TEM. *Micron* **38**, (2007) 224–230. 3
- [Ros07] ROSSELLA F, GALINETTO P, SAMOGGIA G, TREPAAKOV V, JASTRABIK L. Photoconductivity and the structural phase transition in SrTiO_3 . *Solid State Commun.* **141**, (2007) 95–98. 2.1.4
- [Roy01] ROY S, ALI N. Charge transport and colossal magnetoresistance phenomenon in $\text{La}_{1-x}\text{Zr}_x\text{MnO}_3$. *J. Appl. Phys.* **89**(11), (2001) 7425–7427. 4.2.1

- [Sac03] SACHDEV S. Understanding correlated electron systems by a classification of Mott insulators. *Ann. Phys.* **303**, (2003) 226–246. 5
- [Sah00] SAHA S, SINHA T P, MOOKERJEE A. Structural and optical properties of paraelectric SrTiO₃. *J. Phys.: Condens. Matter* **12**, (2000) 3325–3336. 2.1.4
- [Sal01] SALAMON M B, JAIME M. The physics of manganites: Structure and transport. *Rev. Mod. Phys.* **73**, (2001) 583–628. 2.2, 2.2.4
- [Sat96] SATPATHY S, POPOVIC Z S, VUKAJLOVIC F R. Electronic Structure of the Perovskite Oxides: La_{1-x}Ca_xMnO₃. *Phys. Rev. Lett.* **76**, (1996) 960–963. 2.2.2
- [Saw05] SAWA A, FUJII T, KAWASAKI M, TOKURA Y. Highly rectifying Pr_{0.7}Sr_{0.3}MnO₃/SrTi_{0.9998}Nb_{0.0002}O₃ p-n junction. *Appl. Phys. Lett.* **86**, (2005) 112508. 3.1.2.3
- [Sch64] SCHOOLEY J F, HOSLER W R, COHEN M L. Superconductivity in semiconducting SrTiO₃. *Phys. Rev. Lett.* **12**, (1964) 474–475. 2.1.2
- [Sch78] SCHLÜTER M. Chemical trends in metal-semiconductor barrier heights. *Phys. Rev. B* **17**(12), (1978) 5044–5047. 3.4, 3.1.2.1
- [Sch85] SCHNEIDER W D, DELLEY B, WUILLOUD E, IMER J M, BAER Y. Electron-spectroscopic manifestations of the 4*f* states in light rare-earth solids. *Phys. Rev. B* **32**(10), (1985) 6819–6831. 4.2.3.3
- [Sch97] SCHMIDT M, NOHLEN M, BERMES G, BÖHMER M, WANDELT K. A versatile Kelvin probe for dynamic work function change measurements during gas adsorption and *in situ* film growth experiments. *Rev. Sci. Instrum.* **68**, (1997) 3866–3871. 17, 3.2.4.2
- [Sch06] SCHRODER D K. *Semiconductor Material and Device Characterization*. John Wiley & Sons, 3 ed., 2006. 3.1.1, 5
- [Sha98] SHANTHI N, SARMA D D. Electronic structure of electron doped SrTiO₃: SrTiO_{3-δ} and Sr_{1-x}La_xTiO₃. *Phys. Rev. B* **57**, (1998) 2153–2158. 2.1.4
- [Shi72] SHIRLEY D A. High-Resolution X-Ray Photoemission Spectrum of the Valence Bands of Gold. *Phys. Rev. B* **5**(12), (1972) 4709–4714. 2, 4.2.2

- [Shi00] SHIMIZU T, USUI Y, NAKAGAWA T, OKUSHI H. Crystallographic Orientation Dependence of the Schottky Properties of Au/SrTiO₃ Junctions. *J. Electroceramic*. **4**, (2000) 299–303. 3.1.2.1
- [Sih67] SIHVONEN Y. Photoluminescence, Photocurrent, and Phase-Transition Correlations in SrTiO₃. *J. Appl. Phys.* **38**(11), (1967) 4431–4435. 2.1.4
- [Slo07] SLOANE N J A. Sequence A009766. In "The On-Line Encyclopedia of Integer Sequences", 2007. <http://public.research.att.com/~njas/sequences/A009766>. B.2.1
- [Sou72] SOULES T, KELLY E, VAUGHT D, RICHARDSON J. Energy-Band Structure of SrTiO₃ from a Self-Consistent-Field Tight-Binding Calculation. *Phys. Rev. B* **6**(4), (1972) 1519–1532. 2.1.4
- [Sta75] STAEBLER D L. Oxide Optical Memories: Photochromism and Index Change. *J. Solid State Chem.* **12**, (1975) 177–185. 2.1.2
- [Sun04] SUN J, LAI C, WONG H. Photovoltaic effect in La_{0.7}Ce_{0.3}MnO_{3-δ}/SrTiO₃-Nb heterojunction and its oxygen content dependence. *Appl. Phys. Lett.* **85**(1), (2004) 37–39. 3.1.2.2
- [Sur70] SURPLICE N A, D'ARCY R J. A critique of the Kelvin method of measuring work functions. *J. Phys. E: Sci. Instrum.* **3**, (1970) 477–428. 3.2.4.1
- [Sur96] SURESH KUMAR C, SUBRAHMANYAM A, MAJHI J. Automated reed-type Kelvin probe for work function and surface photovoltage studies. *Rev. Sci. Instrum.* **67**, (1996) 805–807. 17
- [Sze81] SZE S. *Physics of Semiconductor Devices*. John Wiley & Sons, New York, 2nd ed., 1981. 2.1, 4
- [Szo99] SZOT K, SPEIER W. Surfaces of reduced and oxidized SrTiO₃ from atomic force microscopy. *Phys. Rev. B* **60**, (1999) 5909–5926. 2.1.3
- [Szo00] SZOT K, SPEIER W, BREUER U, MEYER R, SZADE J, WASER R. Formation of micro-crystals on the (100) surface of SrTiO₃ at elevated temperatures. *Surf. Sci.* **460**, (2000) 112–128. 2.1.3
- [Tan03a] TAN G T, DAI S Y, DUAN P, ZHOU Y L, LU H B, CHEN Z H. Structural, electric and magnetic properties of the electron-doped manganese oxide: La_{1-x}Te_xMnO₃ ($x = 0.1, 0.15$). *J. Appl. Phys.* **93**(9), (2003) 5480–5483. 4.2.1

- [Tan03b] TAN G T, DUAN P, DAI S Y, ZHOU Y L, LU H B, CHEN Z H. Structural magnetic properties and spin-glass behavior in $\text{La}_{0.9}\text{Te}_{0.1}\text{MnO}_3$. *J. Appl. Phys.* **93**(12), (2003) 9920–9923. 4.2.1, 4.2.2
- [Tei04] TEICH S, GRAFSTRÖM S, ENG L. Surface photovoltage of thin organic films studied by modulated photoelectron emission. *Surf. Sci.* **552**, (2004) 77–84. 3.2.2, 3.2.2.2
- [Thi06] THIELE C. *Multiferroische Schichtsysteme: Piezoelektrisch steuerbare Gitterverzerrungen in Lanthanmanganat-Dünnschichten*. Ph.D. thesis, Technische Universität Dresden, 2006. <http://nbn-resolving.de/urn:nbn:de:swb:14-1164036126087-50324>. 2.4, 2.3
- [Tok00] TOKURA Y, NAGAOSA N. Orbital Physics in Transition-Metal Oxides. *Science* **288**, (2000) 462–468. 2
- [Tol03] TOLIŃSKI T, KOWALCZYK A, PUGACZOWA-MICHALSKA M, CHEŁKOWSKA G. The mixed-valence state of Ce in the hexagonal CeNi_4B compound. *J. Phys.: Condens. Matter* **15**, (2003) 1397–1403. 4.2.3.3
- [Tou96] TOUGAARD S. Surface nanostructure determination by x-ray photoemission spectroscopy peak shape analysis. *J. Vac. Sci. Technol. A* **14**(3), (1996) 1415–1423. 2, 4.2.3.1
- [Tuf67] TUFTE O, CHAPMAN P. Electron Mobility in Semiconducting Strontium Titanate. *Phys. Rev.* **155**(3), (1967) 796–802. 2.1.5
- [Vic97] VICKERMAN J C, ed. *Surface Analysis - The Principal Techniques*. John Wiley & Sons, Chichester, 1997. 4.1, 4.4
- [Vol54] VOLGER J. Further experimental investigations on some ferromagnetic oxidic compounds of manganese with perovskite structure. *Physica* **20**, (1954) 49–66. 2.2.1, 2.3
- [Vri83] VRIENS L, RIPPENS W. Optical constants of absorbing thin solid films on a substrate. *Appl. Opt.* **22**, (1983) 4105–4110. A.2
- [Wan06a] WANG D J, SUN J R, ZHANG S Y, LIU G J, SHEN B G, TIAN H F, LI J Q. Hall effect in $\text{La}_{0.7}\text{Ce}_{0.3}\text{MnO}_{3+\delta}$ film with variable oxygen content. *Phys. Rev. B* **73**, (2006) 144403. 4.2.4

- [Wan06b] WANG D J, XIONG C M, LIU G J, XIE Y W, SHEN B G, SUN J R. Effects of oxygen content on the transport property of $\text{La}_{0.7}\text{Ce}_{0.3}\text{MnO}_{3+\delta}$ film. *Physica B* **371**, (2006) 187–191. 4.2.4
- [Wat04] WATANABE W, OKANO M. Photoresponse of Tunneling Conduction through $\text{Pb}(\text{Ti,Zr})\text{O}_3/\text{SrTiO}_3$ Junction at Low Temperature. *Integr. Ferroelectr.* **62**, (2004) 49–54. 3.1.2.2
- [Wea59] WEAVER H E. Dielectric properties of single crystals of SrTiO_3 at low temperatures. *J. Phys. Chem. Solids* **11**, (1959) 274–277. 2.1.1
- [Wea74] WEAKLIEM H A, BRAUNSTEIN R, STEARNS R. Wavelength modulation spectra of SrTiO_3 . *Solid State Commun.* **15**, (1974) 5–8. 2.1.4
- [Wea75] WEAKLIEM H A, BURKE W J, REDFIELD D, KORSUN V. Optical properties of SrTiO_3 and LiNbO_3 . *RCA Rev.* **35**, (1975) 149–162. 2.1.4
- [Wei07] WEISSTEIN E W. Catalan’s Triangle. From *MathWorld* - A Wolfram Web Resource., 2007. [http://mathworld.wolfram.com/Catalans Triangle.html](http://mathworld.wolfram.com/Catalans%20Triangle.html). B.2.1
- [Wem71] WEMPLE S H, DIDOMENICO M. Behavior of the Electronic Dielectric Constant in Covalent and Ionic Materials. *Phys. Rev. B* **3**, (1971) 1338–1351. A.2
- [Wid03] WIDDRA W, BRÖCKER D, GIESSEL T, HERTEL I V, KRÜGER W, LIERO A, NOACK F, PETROV V, POP D, SCHMIDT P M, WEBER R, WILL I, WINTER B. Time-resolved core level photoemission: surface photovoltage dynamics of the $\text{SiO}_2/\text{Si}(100)$ interface. *Surf. Sci.* **543**, (2003) 87–94. 3.2.2
- [Wil71] WILLIAMS R. Photoconductivity in Photochromic Strontium Titanate. *J. Appl. Phys.* **42**, (1971) 1131–1135. 2.1.2
- [Win98] WINDT D L. IMD - Software for modeling the optical properties of multilayer films. *Comput. Phys.* **12**, (1998) 360–370. A.1
- [Wol73] WOLFRAM T, KRAUT E, MARTIN F. *d*-Band Surface States on Transition-Metal Perovskite Crystals: I. Qualitative Features and Application to SrTiO_3 . *Phys. Rev. B* **7**(4), (1973) 1677–1694. 2.1.3, 3.2.3.2, 3.2.3.2
- [Wui84] WUILLOUD E, DELLEY B, SCHNEIDER W D, BAER Y. Spectroscopic Evidence for Localized and Extended *f*-Symmetry States in CeO_2 . *Phys. Rev. Lett.* **53**(2), (1984) 202–205. 4.2.3.3

- [Yac73] YACOBY Y, NAVEH O. Differential Optical Spectra and Band Structure of SrTiO₃. *Phys. Rev. B* **7**(3), (1973) 3991–4000. 2.1.4, 3.2.2.2
- [Yan99] YANG Y S, KIM J P, LEE S H, JOO H J, JANG M S, YI S. Space Charge Effects in the Photocurrent Spectrum of Ferroelectric Pb(Zr,Ti)O₃ Thin Films. *J. Kor. Phys. Soc.* **35**, (1999) S1168–S1171. 3.1.2.2
- [Yan00] YANG Y S, LEE S J, YI S, CHAE B G, LEE S H, JOO H J, JANG M S. Schottky barrier effects in the photocurrent of sol-gel derived lead zirconate titanate thin film capacitors. *Appl. Phys. Lett.* **76**, (2000) 774–776. 3.1.2.2
- [Yan04a] YANAGIDA T, KANKI T, VILQUIN B, TANAKA H, KAWAI T. La_{0.7}Ce_{0.3}MnO₃ epitaxial films fabricated by a pulsed laser deposition method. *Solid State Commun.* **129**, (2004) 785–790. 4.2.1
- [Yan04b] YANAGIDA T, KANKI T, VILQUIN B, TANAKA H, KAWAI T. Metal-insulator transition and ferromagnetism phenomena in La_{0.7}Ce_{0.3}MnO₃ thin films: Formation of Ce-rich nanoclusters. *Phys. Rev. B* **70**, (2004) 184437. 4.2.1
- [Yan04c] YANG J, ZHAO B C, ZHANG R L, MA Y Q, SHENG Z G, SONG W H, SUN Y P. The effect of grain size on electrical transport and magnetic properties of La_{0.9}Te_{0.1}MnO₃. *Solid State Commun.* **132**, (2004) 83–87. 4.2.1
- [Yan05a] YANAGIDA T, KANKI T, VILQUIN B, TANAKA H, KAWAI T. Transport and magnetic properties of Ce-doped LaMnO₃ thin films. *Appl. Surf. Sci.* **244**, (2005) 355–358. 4.2.4
- [Yan05b] YANAGIDA T, KANKI T, VILQUIN B, TANAKA H, KAWAI T. Transport and magnetic properties of La_{0.9}Te_{0.1}MnO₃. *J. Appl. Phys.* **97**, (2005) 033905. 4.2.1
- [Zeg82] ZEGENHAGEN J, HAAGE T, JIANG Q D. Microscopic structure and structuring of perovskite surfaces and interfaces: SrTiO₃, RBa₂Cu₃O_{7-δ}. *Appl. Phys. A* **67**, (1982) 711–722. 2.1.3
- [Zen51] ZENER C. Interaction between the *d*-Shells in the Transition Metals. II. Ferromagnetic Compounds of Manganese with Perovskite Structure. *Phys. Rev.* **82**, (1951) 403–405. 2.2.1, 2.2.3
- [Zer05] ZERWECK U, LOPPACHER C, OTTO T, GRAFSTRÖM S, ENG L M. Accuracy and resolution limits of Kelvin probe force microscopy. *Phys. Rev. B* **71**, (2005) 125424. 17

- [Zha84] ZHAO L Z, YOUNG V. XPS studies of carbon supported films formed by the resistive deposition of manganese. *J. Electron Spectrosc. Relat. Phenom.* **34**, (1984) 45–54. 4.2.2, 4.2.2, 4.2.3.5, 4.2.3.6, 4.15
- [Zha98] ZHANG W, WANG X, BOYD I W. Incongruent transfer related to surface segregation in pulsed-laser-deposited La-Ca-Mn-O films. *Appl. Phys. Lett.* **73**(19), (1998) 2745–2747. 4.2.3.1
- [Zha02] ZHANG-STEENWINKEL Y, BECKERS J, BLIEK A. Surface properties and catalytic performance in CO oxidation of cerium substituted lanthanum-manganese oxides. *Appl. Catal., A* **235**, (2002) 79–92. 4.2.2, 4.2.3.2
- [Zha03] ZHANG X, DEMKOV A A, LI H, HU X, WEI Y. Atomic and electronic structure of the Si/SrTiO₃ interface. *Phys. Rev. B* **68**, (2003) 125323. 7, 3.1.2.1
- [Zha04] ZHANG F, WANG P, KOBERSTEIN J, KHALID S, CHAN S W. Cerium oxidation state in ceria nanoparticles studied with X-ray photoelectron spectroscopy and absorption near edge spectroscopy. *Surf. Sci.* **563**, (2004) 74–82. 4.2.3.3
- [Zha05] ZHAO K, HUANG Y, ZHOU Q, JIN K J, LU H, HE M, CHENG B, ZHOU Y, CHEN Z, YANG G. Ultraviolet photovoltage characteristics of SrTiO_{3-δ}/Si heterojunction. *Appl. Phys. Lett.* **86**, (2005) 221917. 3.1.2.1
- [Zha06] ZHAO K, JIN K, HUANG Y, ZHAO S, LU H, HE M, CHEN Z, ZHOU Y, YANG G. Ultraviolet fast-response photoelectric effect in tilted orientation SrTiO₃ single crystals. *Appl. Phys. Lett.* **89**, (2006) 173507. 3.1.2.1
- [Zho05] ZHOU Q L, JIN K L, LU H B, HAN P, CHEN Z H, ZHAO K, ZHOU Y L, YANG G Z. Transport property in SrTiO₃ p-n junction. *Europhys. Lett.* **71**, (2005) 283–289. 2.1.2
- [Zis32] ZISMAN W A. A new method of measuring contact potential differences in metals. *Rev. Sci. Instrum.* **3**, (1932) 367–370. 3.2.4.1
- [Zol00] ZOLLNER S, DEMKOV A A, LIU R, FREJES P L, GREGORY R B, CURLESS J A, YU Z, RAMDANI J, DROOPAD R, TIWALD T E, HILFIKER J N, WOOLLAM J A. Optical properties of bulk and thin-film SrTiO₃ on Si and Pt. *J. Vac. Sci. Technol. B* **18**, (2000) 2242–2254. 2.1.4

A *MATHEMATICA*[®] scripts

A.1 Electrical field intensity at buried interfaces – calculation with the Fresnel matrix formalism

In chapter 3, when reporting on surface photovoltage spectroscopy of manganite/strontium titanate interfaces, we mentioned the need of a constant photon flux over the measured wavelength spectrum at the interface of interest. Thus the spectral transmission of all optical elements in the beam path have to be known. Additionally the transmission of the manganite film, or, to be more exact, the electric field intensity at the interface must be determined.

The latter issue leads us to the complex field of thin film optics. If we follow a beam of light that travels through a layered system of thin films, we recognize that we have to consider multiple reflections and interference effects if we want to calculate the electrical field or its square, the electrical field intensity, at an arbitrary position within the film system (figure A.1). Though in principle the problem is straightforward, as the amplitudes and intensities are well defined by MAXWELL's equations and the appropriate boundary conditions, the resulting equations are quite complicated.

Several notation systems and formalisms have been developed to get the problem manageable. The following *MATHEMATICA*[®] script is based on the matrix formalism using FRESNEL coefficients by ABELÈS as presented in the monograph by HEAVENS [Hea91]. The *main message* of this formalism is that the field amplitudes in the n^{th} layer are a linear transformation of the field amplitudes in the $(n - 1)^{\text{th}}$ layer. Those linear transformations are represented by 2×2 matrices whose coefficients contain the complex refractive indices¹ of the materials involved, the wavelength, the film thicknesses, and the angle of incidence.

For our precise problem we work with the following *input* data and assumptions:

- A four-media system is assumed:
 - a half-space of air,
 - a *thin* manganite film (10 nm LCMO, 10 nm LCeMO, or 15 nm LSMO),
 - a *thick* strontium titanate layer of 0.5 mm thickness,

¹For the complex refractive index \tilde{n} we use the definition $\tilde{n} = n - ik$, where n is the real part of the refractive index and k is the extinction coefficient.

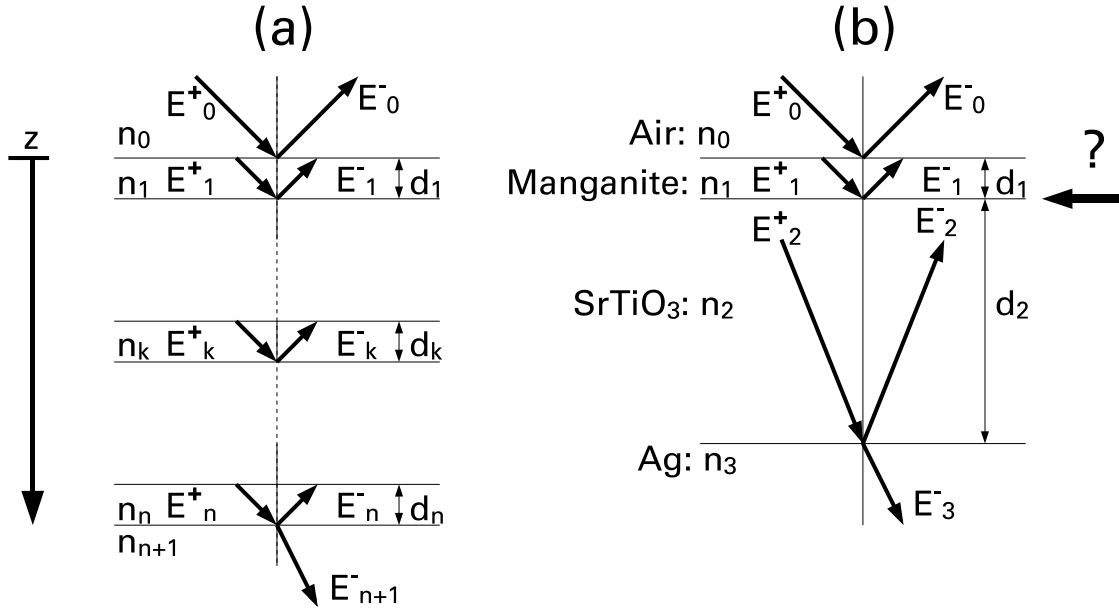


Figure A.1: Notation for optical calculations of (a) an arbitrary system of layers and (b) the special system investigated here. To calculate the amplitude of the electrical field at each position z in the system the complex refractive indices n_i of all participating media, the film thicknesses d_i , the angle of incidence, and the wavelength must be known. Note that for normal incidence as in our case the field intensity (square of the electric field) must be a continuous function of the coordinate z . In our calculation this fact is employed to establish a test procedure (*consistency check*), see text. The thick black arrow with the question mark indicates the quantity we are looking for: the electrical field intensity at the manganite/SrTiO₃ interface.

- a half-space of silver (representing the back contact made of conductive silver paste);
- the angle of incidence is 0° (normal incidence);
- the coherence length of the incident light (coming from a monochromatized white-light source) is smaller than the thickness of the second (STO) layer;
- complex refractive indices for the media involved as indicated in table A.1.

The subsequent script first reads the real and the imaginary parts of the refractive indices from ASCII files and expresses them analytically by fitting them with a polynomial of sufficiently high order (In[1]-In[18]). The plots, which indicate the real and imaginary parts of the refractive index of LSMO, SrTiO₃ and Ag as a function of wavelength (in units of nm) in this order, are used to compare the resulting polynomials with the original data and to decide whether the chosen order was high enough. Note that the wavelength is represented by x for convenience and that the example is given for the case of the 15-nm-thick LSMO film. Second, all quantities necessary for the matrix calculation are

index	material	source of data
0	air	$n = 1, k = 0$
1	LCMO, LCeMO, LSMO	[Rau02, Rau04]
2	SrTiO ₃	own measurement, see appendix A.2
3	Ag	[Pal91]

Table A.1: Sources of the optical constants for the air/manganite/STO/Ag system.

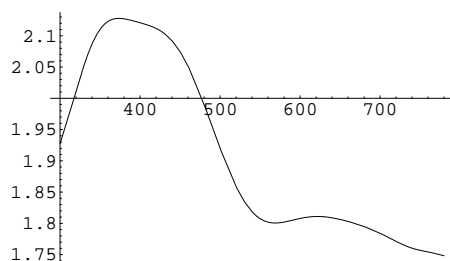
defined. After that the field intensity at the interface of interest, $I_2(0)$, is calculated, normalized with respect to the incident intensity (In[46]), which is assumed to be 1. As a consistency check the continuity of the intensity is tested. It can be seen that the plot of I_2 versus the wavelength is strongly oscillating, because our matrix formalism assumes a coherent superposition of all partial waves, also throughout the thick STO layer. To correct this unrealistic result, we convolute the result with a Gaussian distribution (In[58]). A meaningful fineness of data points for this procedure is defined after monitoring the oscillation period of the original data for I_2 (Out[53]). Figure A.2 depicts the result I_2mean as it was used for the surface photovoltage spectroscopy measurements (see again chapter 3). The algorithm can be easily adapted to other material systems and, with some extensions, for different angles of incidence. The correctness of the script has been additionally tested by comparison with results of the computer program IMD [Win98], which uses the same formalism but is not able to handle layers as thick as our STO substrate². Thus the tests were performed assuming much thinner STO layers.

²At least the Unix version showed serious memory problems.

```
In[1]:= TABnLSMO=Import["Mathematica/lists/list_LSMO_own_n_800_400.dat","Table"];
```

```
In[2]:= nLSMO=Fit[TABnLSMO, {1, x, x^2,x^3,x^4,x^5,x^6,x^7,x^8,x^9,x^10,x^11,x^12,x^13,x^14}, x];
```

```
In[3]:= Plot[nLSMO,{x,780,300}]
```

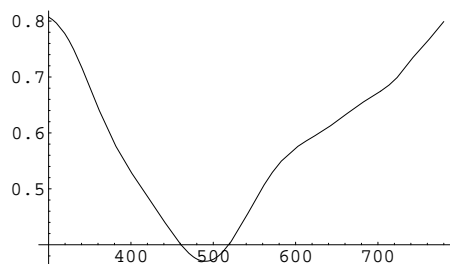


```
Out[3]= -Graphics-
```

```
In[4]:= TABkLSMO=Import["Mathematica/lists/list_LSMO_own_k_800_400.dat","Table"];
```

```
In[5]:= kLSMO=Fit[TABkLSMO, {1, x, x^2,x^3,x^4,x^5,x^6,x^7,x^8,x^9,x^10,x^11,x^12,x^13,x^14}, x];
```

```
In[6]:= Plot[kLSMO,{x,780,300}]
```

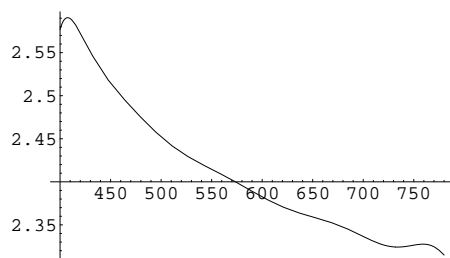


```
Out[6]= -Graphics-
```

```
In[7]:= TABnSTO=Import["Mathematica/lists/list_STO_own_n_800_400.dat","Table"];
```

```
In[8]:= nSTO=Fit[TABnSTO, {1, x, x^2,x^3,x^4,x^5,x^6,x^7,x^8,x^9,x^10,x^11,x^12,x^13,x^14,x^15,x^16}, x];
```

```
In[9]:= Plot[nSTO,{x,780,400}]
```

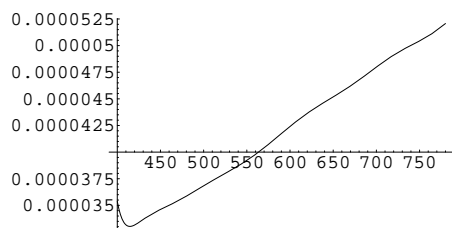


```
Out[9]= -Graphics-
```

```
In[10]:= TABkSTO=Import["Mathematica/lists/list_STO_own_k_800_400.dat","Table"];
```

```
In[11]:= kSTO=Fit[TABkSTO, {1, x, x^2,x^3,x^4,x^5,x^6,x^7,x^8,x^9,x^10,x^11,x^12,x^13},x];
```

```
In[12]:= Plot[kSTO,{x,780,400}]
```

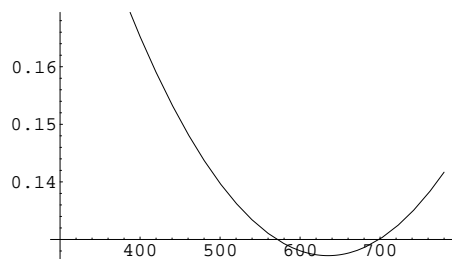


```
Out[12]= -Graphics-
```

```
In[13]:= TABnAg=Import["Mathematica/lists/list_Ag_palik_n_800_400.dat","Table"];
```

```
In[14]:= nAg=Fit[TABnAg,{1,x,x^2},x];
```

```
In[15]:= Plot[nAg,{x,780,300}]
```

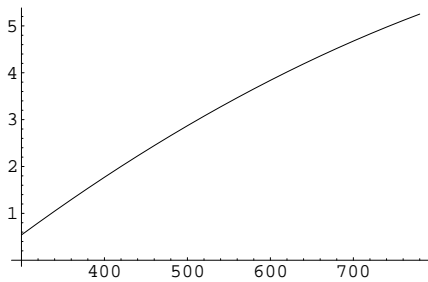


```
Out[15]= -Graphics-
```

```
In[16]:= TABkAg=Import["Mathematica/lists/list_Ag_palik_k_800_400.dat","Table"];
```

```
In[17]:= kAg=Fit[TABkAg,{1,x,x^2},x];
```

```
In[18]:= Plot[kAg,{x,780,300}]
```

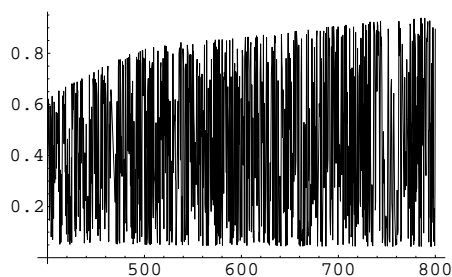


```
Out[18]= -Graphics-
```

```

In[19]:= n0:=1; (*n_air*)
In[20]:= n1=nLSMO-I*kLSMO; (*complex refractive index of LSMO*)
In[21]:= n2=nSTO-I*kSTO; (*complex refractive index of STO*)
In[22]:= n3=nAg-I*kAg; (*complex refractive index of Ag*)
In[23]:= d1:=15; (*thickness of the LSMO layer (nm)*)
          d2:=500000; (*thickness of the STO substrate (nm)*)
In[25]:= r1=(n0-n1)/(n0+n1); (*complex interface reflectances*)
          r2=(n1-n2)/(n1+n2);
          r3=(n2-n3)/(n2+n3);
In[28]:= t1=2*n0/(n0+n1); (*complex interface transmittances*)
          t2=2*n1/(n1+n2);
          t3=2*n2/(n2+n3);
In[31]:= delta1=2*Pi*n1*d1/x; (*phase angles*)
          delta2=2*Pi*n2*d2/x;
In[33]:= C1={{1, r1}, {r1, 1}}; (*matrices*)
          C2={{E^(I*delta1), r2*E^(I*delta1)},
              {r2*E^(-I*delta1), E^(-I*delta1)}};
          C3={{E^(I*delta2), r3*E^(I*delta2)},
              {r3*E^(-I*delta2), E^(-I*delta2)}};
In[36]:= Cp3=C1*C2*C3; (*product matrix*)
In[37]:= a=Cp3[[1,1]]; (*elements of the product matrix*)
          b=Cp3[[1,2]];
          c=Cp3[[2,1]];
          d=Cp3[[2,2]];
In[41]:= E0m=c/a*E0p; (*... several components of the electric field*)
In[42]:= E3p=t1*t2*t3*(d*E0p-b*E0m)/(a*d-b*c);
          E3m:=0;
In[44]:= {E2p,E2m}=1/t3*C3.{E3p,E3m};
In[45]:= {E1p,E1m}=1/t2*C2.{E2p,E2m};
In[46]:= I2=(Abs[(E2p/E0p)+(E2m/E0p)])^2; (*intensity at the LSMO/STO-interface*)
In[47]:= Plot[I2,{x,400,800}]

```



```
Out[47]= -Graphics-
```

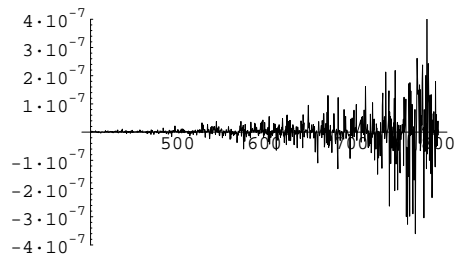
```

In[48]:= kappa1=2*Pi*n1/x; (*consistency check*)
          kappa2=2*Pi*n2/x;
In[50]:= I1=(Abs[(E1p*E^(-I*kappa1*15)/E0p)+(E1m*E^(I*kappa1*15)/E0p)])^2;

```



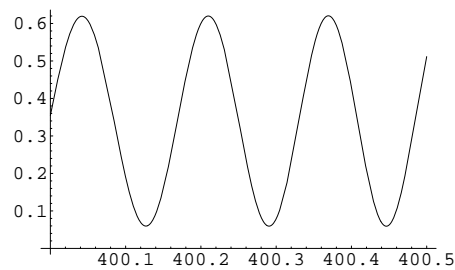
```
In[51]:= diff=I1-I2;
Plot[diff,{x,400,800},PlotRange->{-0.0000004,0.0000004}]
```



Out[52]= -Graphics-

```
In[53]:= Plot[I1,{x,400,400.5}]
```

(*oscillation period check (works also with I2)*)



Out[53]= -Graphics-

```
In[54]:= data=Table[I2,{x,400,800,0.01}];
```

(*puts I2 into a list*)

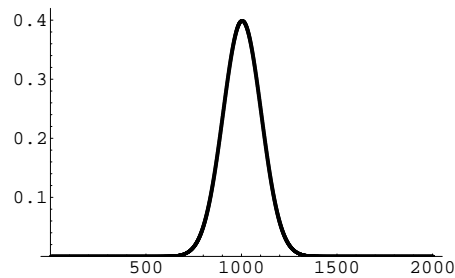
```
In[55]:= ListPlot[data];
```

(*plots the list (optional)*)

```
In[56]:= kern=Table[Exp[-n^2/2]/Sqrt[2*Pi],
{n, -10, 10, 0.01}];
```

(*generates a Gaussian distribution ("kernel"*)

```
In[57]:= ListPlot[kern,PlotRange->{0,0.42}]
```



Out[57]= -Graphics-

```
In[58]:= I2mean=ListConvolve[kern,data];
distribution*)
```

(*convolutes the I2-list with the Gaussian

```
In[59]:= Export["list.dat",I2mean]
```

(*exports the data into an ASCII file*)

Out[59]= list.dat

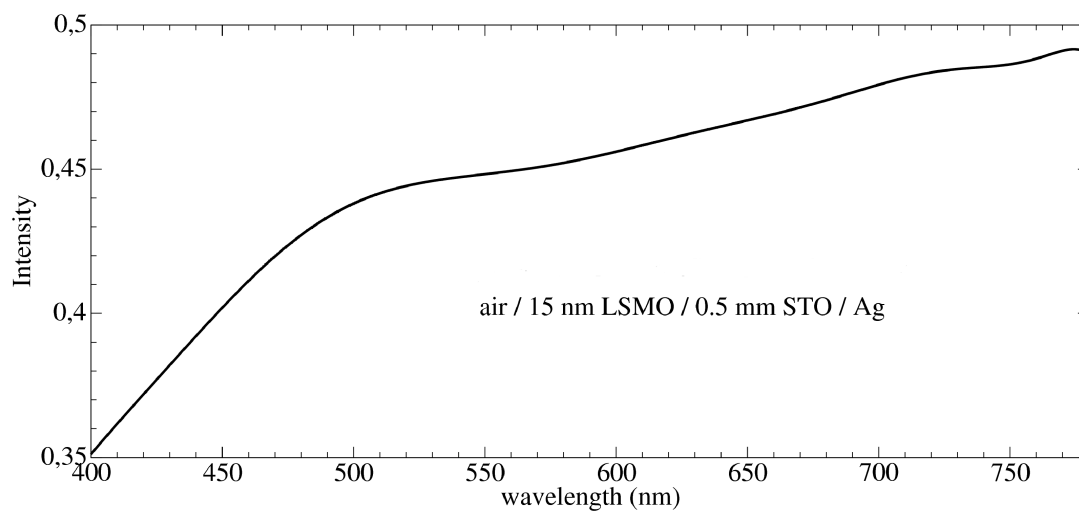


Figure A.2: Intensity at the LSMO/STO interface as calculated with the FRESNEL matrix formalism under the assumption of an *air/LSMO/STO/Ag* structure.

A.2 Calculation of the optical constants of a weakly absorbing substrate from transmission and reflection measurements

In chapter 2.1.4 we discussed the optical properties of strontium titanate and stressed that they can dramatically differ depending on the sample quality, especially on the oxygen content. Consequently it seems most appropriate to make an individual measurement for the sample of interest. Here, a SrTiO₃ substrate, polished on both sides, from the same manufacturer and with the same thickness (0.5 mm) as the substrates that were used for the deposition of the manganite films was investigated with respect to its optical transmission T and reflection R at near-normal incidence. The measurements were performed with a spectrophotometer, type UV 3100, by Shimadzu. Figure A.3 contains the data for T and R . The sample is slightly absorbing.

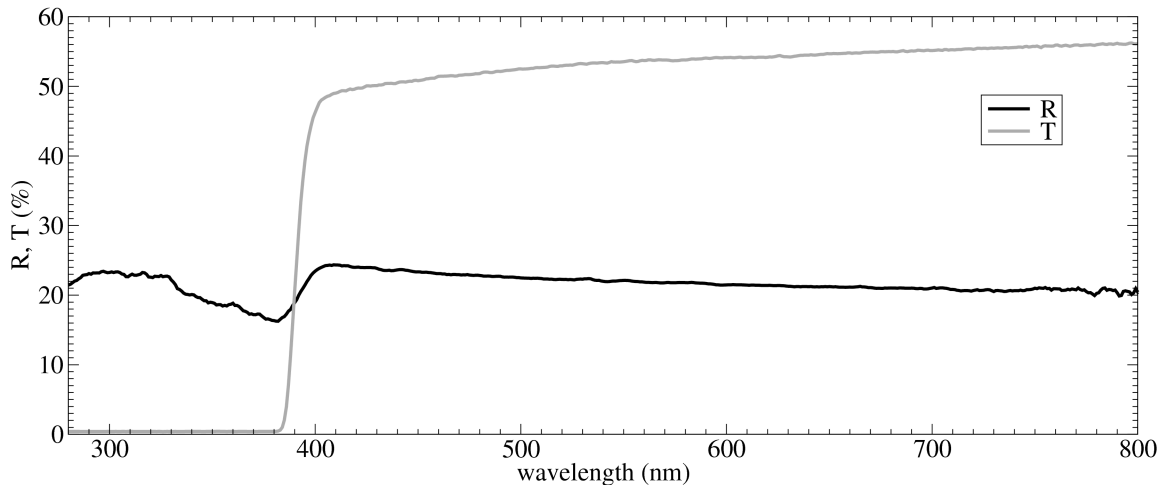


Figure A.3: Optical transmission and reflectivity of a SrTiO₃ substrate.

We use the formulae by VRIENS et al. [Vri83] to calculate the refractive index n and the absorption coefficient³ a from the (R, T) data for a weakly absorbing substrate, as documented in the following script. Note that the script shown here does not contain the complete output of (n, a) pairs and that the output has to be converted into an ASCII file by another script. The results for n and k have already been shown in appendix A.1. The data for n fit well to the universal curve for ionic compounds given by WEMPLE et al. [Wem71] (not shown here).

³Extinction coefficient k and absorption coefficient a both describe the energy loss in a medium, their connection in the notation of [Vri83] is as follows: $a = 4\pi kd/\lambda$, where d is the thickness of the substrate. However, this definition is unusual, in most cases a does not contain the length of the medium and can be then understood as an inverse absorption length.

```

(*definition of the transmitted intensity T(n,a)*)

T = (4*n)/(E^a*((n + 1)^2*(1 - (n - 1)^4/(E^(2*a)*(n + 1)^4))))
      4 e-a n
      -----
      (n + 1)2 (1 -  $\frac{e^{-2a}(n-1)^4}{(n+1)^4}$ )

(*definition of the reflected intensity R(n,a)*)

R = (16*n^2*(n - 1)^2)/(E^(2*a)*((n + 1)^6*
      (1 - (n - 1)^4/(E^(2*a)*(n + 1)^4)))) + (n - 1)^2/(n + 1)^2
      16 e-2a n2 (n - 1)2 + (n - 1)2
      -----
      (n + 1)6 (1 -  $\frac{e^{-2a}(n-1)^4}{(n+1)^4}$ ) + (n + 1)2

(*import of ASCII file with reflection data*)

p=Import["R.dat","Table"];

(*import of ASCII file with transmission data*)

q=Import["T.dat","Table"];

(*search for simultaneous solutions (n,a) for R and T*)

g[i_]:=FindRoot[{T==q[[i,2]]/100,R==p[[i,2]]/100},{n,1.8},{a,0}]

(*prints the solution for each wavelength*)

Do[Print[g[i]],{i,1801}]
{n → 2.17764, a → 0.478314}
{n → 2.19206, a → 0.471375}
{n → 2.20142, a → 0.464691}
{n → 2.21232, a → 0.462497}
{n → 2.22073, a → 0.463395}
{n → 2.25097, a → 0.456294}
{n → 2.2665, a → 0.450714}
{n → 2.20388, a → 0.462691}
{n → 2.18188, a → 0.465307}
{n → 2.197, a → 0.463735}
{n → 2.22183, a → 0.462142}
{n → 2.24707, a → 0.459955}
{n → 2.25232, a → 0.458981}

```

B Addenda to the surface photovoltage part

B.1 Collection of SPV spectra from C-SPS

In section 3.2.3.2 we discussed the results of capacitive surface photovoltage spectroscopy on three different manganite/SrTiO₃ interfaces: LSMO/STO, LCMO/STO, LCeMO/STO. There, a detailed spectrum including the assignment of interface trap state positions was given *only* for the LSMO case (figure 3.9). This appendix contains further data: first a graph showing the reproducibility of a SPV spectrum, and subsequently the SPV spectra for the LCMO and LCeMO cases, including some explanations on trap position assignment.

Figure B.1 shows two SPV spectra of the LCeMO/STO interface acquired under the same experimental conditions. The shape, including slope and slope changes, of the spectra is the same, only the signal level is slightly different. The latter effect can be attributed to different initial states of the sample before the two measurements. The term *initial state* means that the sample might contain a different amount of photo-excited carriers from a previous measurement. However, the difference is small compared with the difference in signal level between the as-prepared and annealed cases of LCMO and LCeMO (figure 3.10).

Let us now discuss the spectra of LCeMO/STO and LCMO/STO in detail:

- Figure B.2 [(a)-(c)] displays the SPV spectrum of the as-prepared LCeMO sample. The division into three overlapping diagrams serves for a better visualization, since the signal covers a range of several orders of magnitude. Panels (d)-(f) depict the respective second derivative. The energetic positions of slope changes were determined from a comparison of the original data and the second derivative as described in section 3.2.3.2. The solid and dashed vertical lines indicate (similarly to figure 3.9) positive and negative slope changes, respectively. The numbers inside the diagram denote the wavelength positions of the points of slope change. Note that the slope change at around 710 nm cannot be found in the second derivative, which becomes very noisy near the low-energy end.
- Figure B.3 depicts the SPV spectra of both the as-prepared and the annealed LCeMO sample. At the high-energy end (a) the two spectra show the clearest differences, whereas in parts (b) and (c) they exhibit the same slope change positions. Here, vertical lines were only drawn for slope changes different from those in

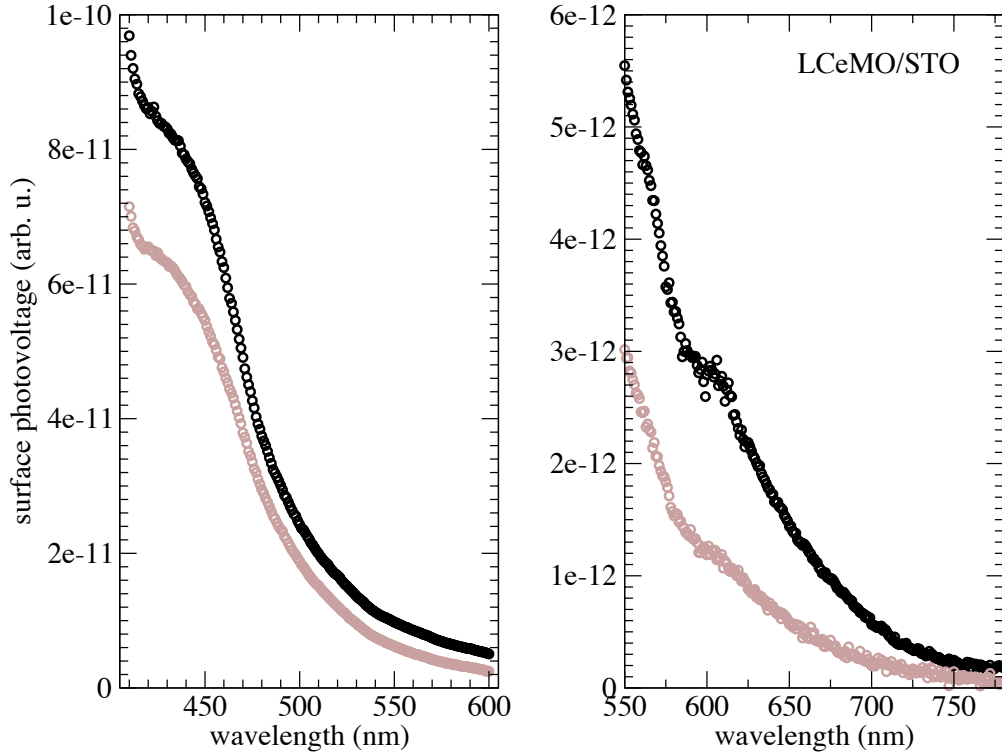


Figure B.1: Reproducibility of a C-SPS measurement on LCeMO/STO. Note again that the SPV values correspond to the photocurrent in the capacitor structure (in amps).

figure B.2.

- The SPV spectrum of LCMO is shown in figure B.4.
- In figure B.5 the spectrum of the annealed LCMO sample is analyzed by comparison with the spectrum of the as-prepared sample. Note that, in contrast to the three previous figures, part (f) does not show the second derivative but an enlarged view of part (c) to make visible the details of the data of the annealed sample. It must be admitted that the slope changes at 590 nm and 610 nm are uncertain due to the low signal-to-noise ratio.

In conclusion, it is obvious that the interpretation of the SPV spectra is not unambiguous in all cases, and only a twofold comparative approach (comparison between original data and 2nd derivative *and* between different samples) as chosen here can provide reasonable results. The trap state positions extracted from the SPV spectra were finally listed in a diagram and condensed into 17 levels (figure B.6). This diagram forms the basis for table 3.1, which additionally specifies possible origins of the distinct levels.

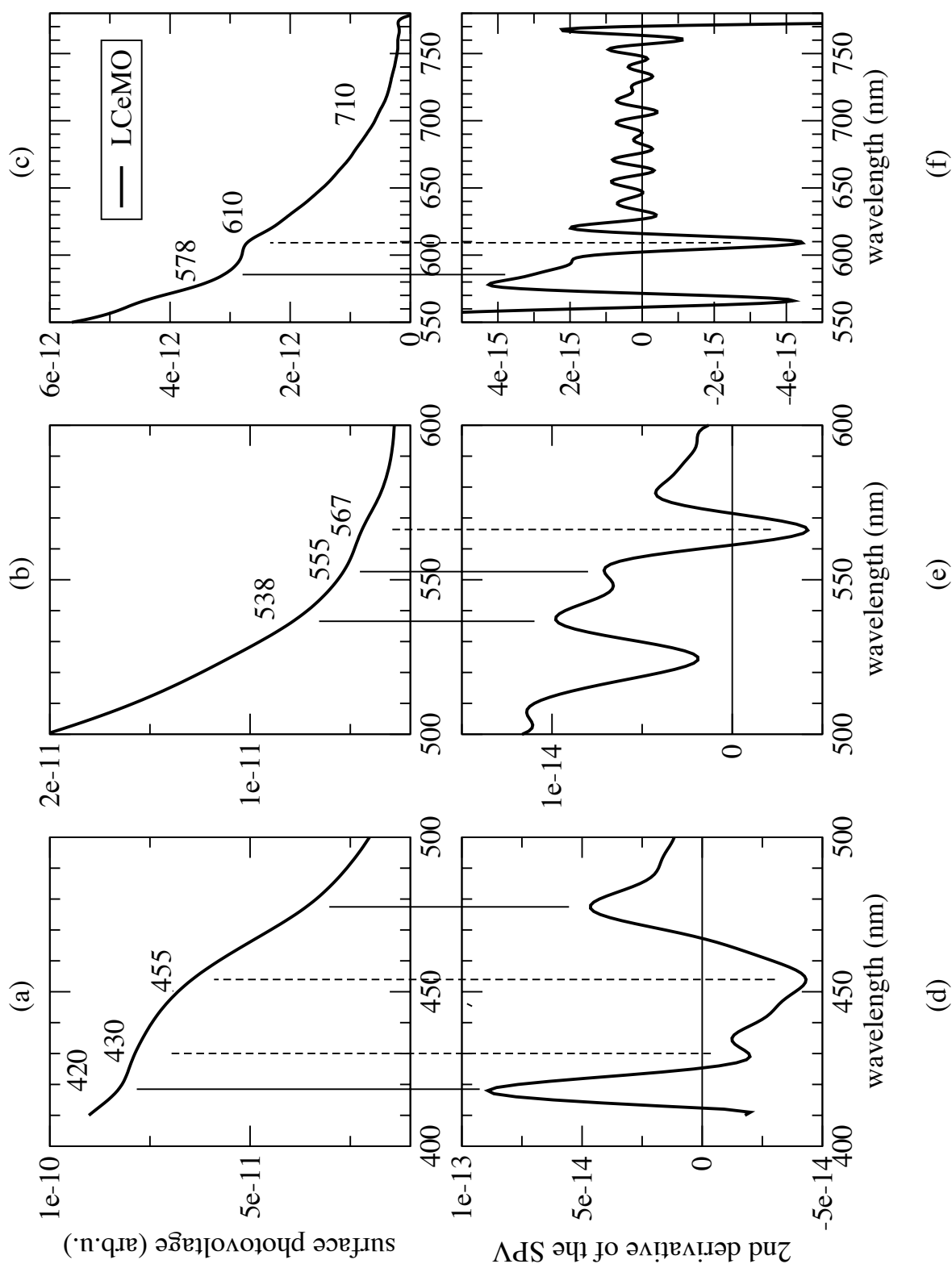


Figure B.2: SPV spectrum of the LCeMO/STO system.

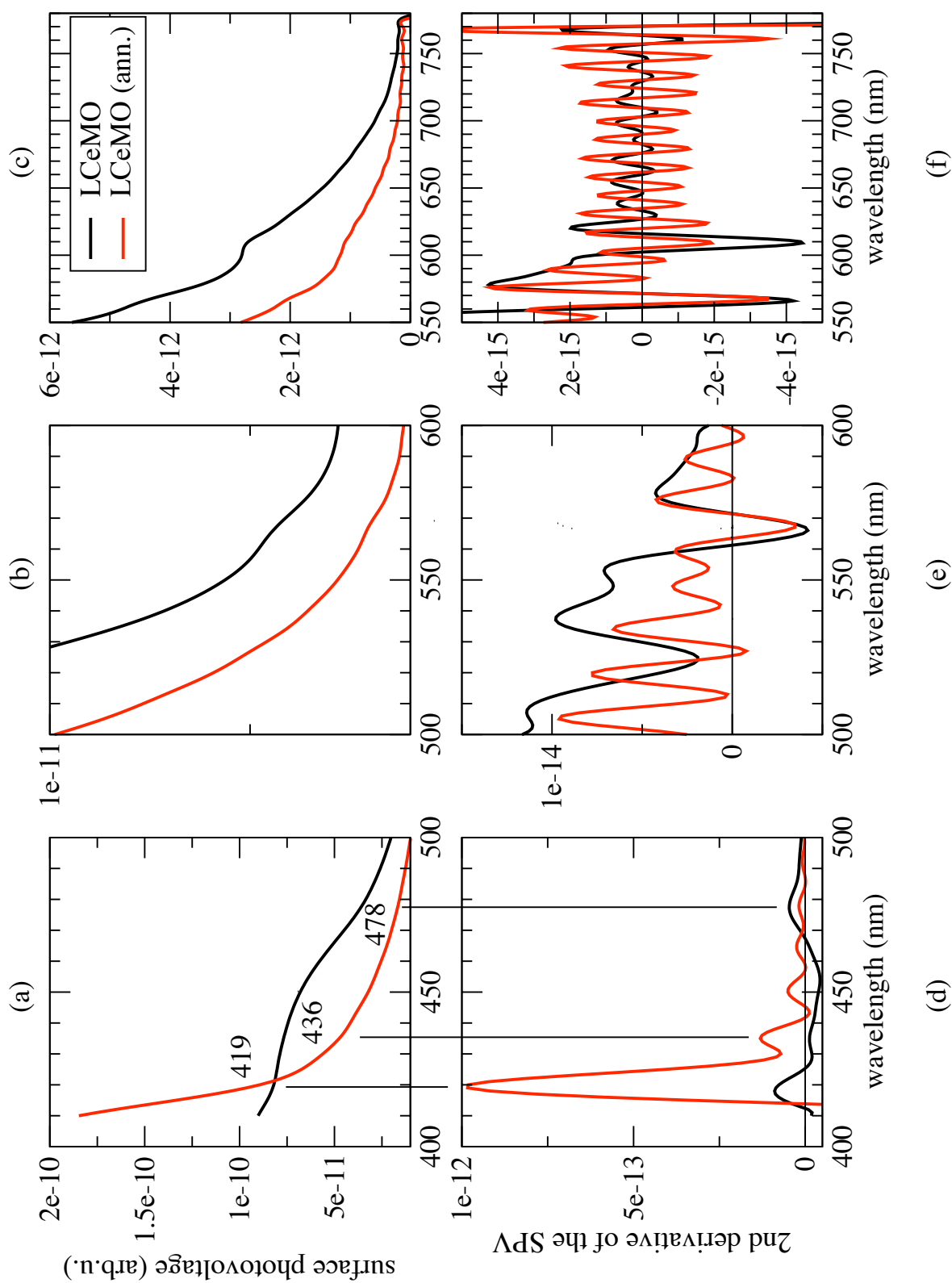


Figure B.3: SPV spectra of the LCeMO/STO system, as-prepared and annealed.

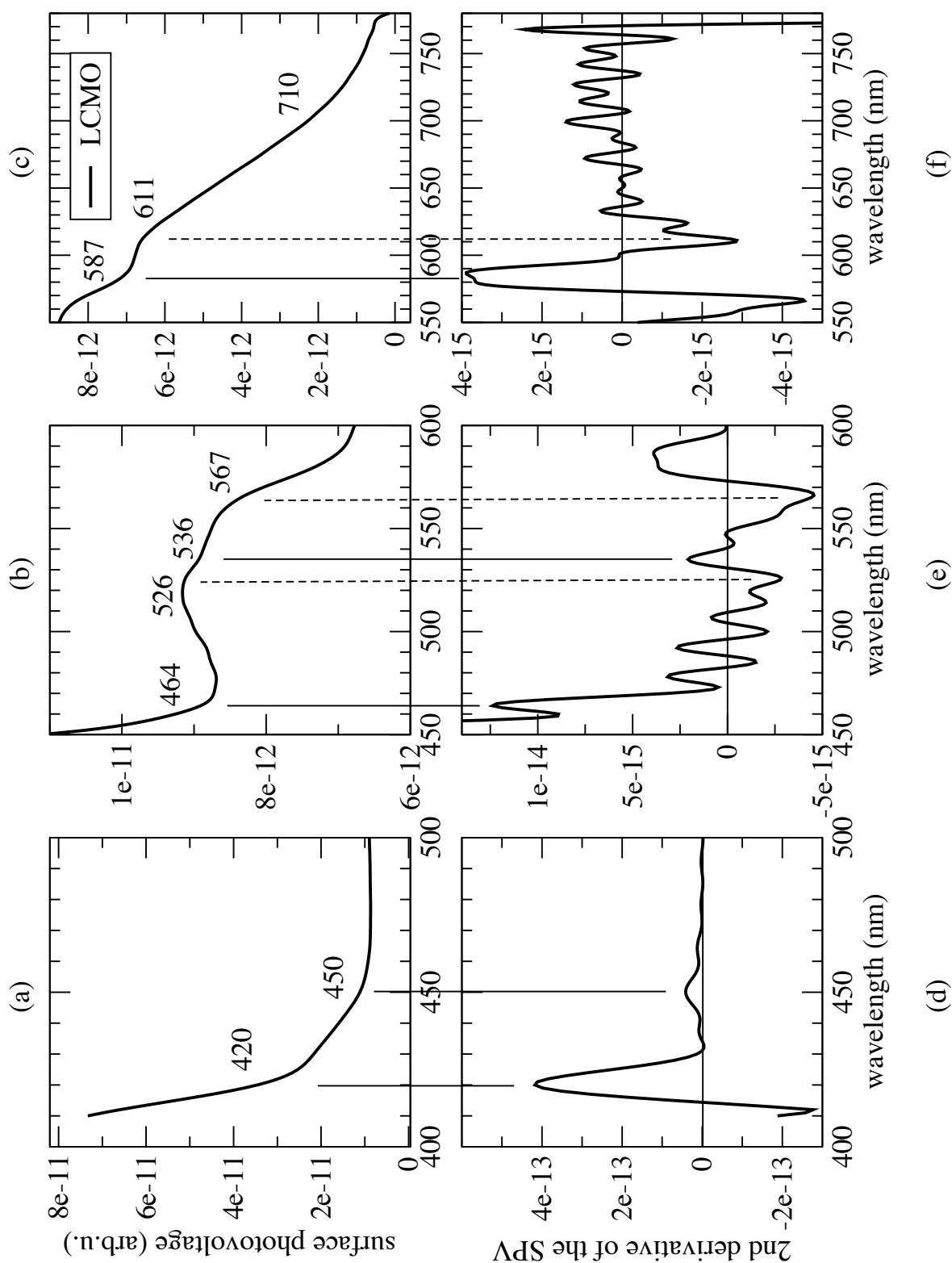


Figure B.4: SPV spectrum of the LCMO/STO system.

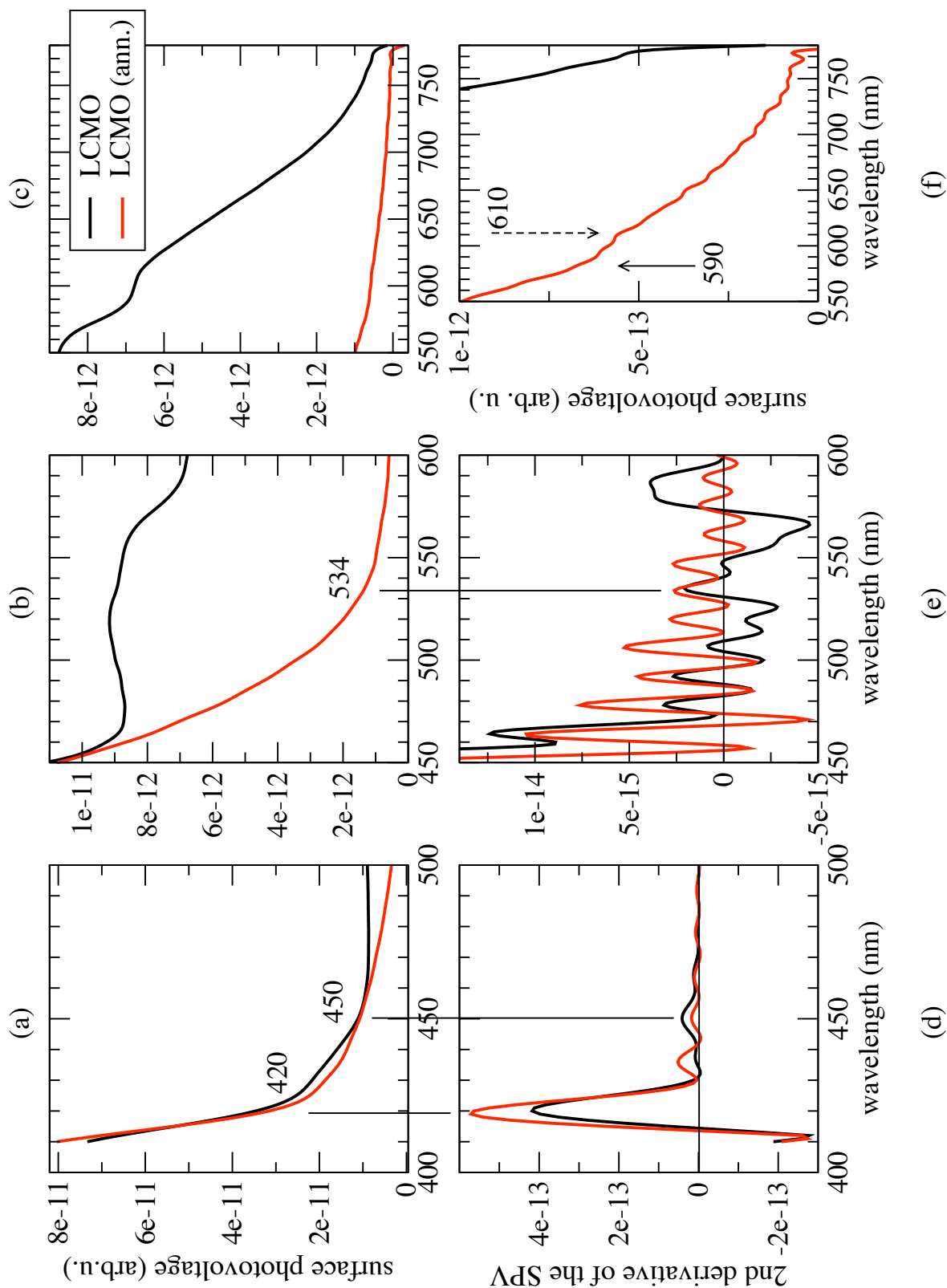


Figure B.5: SPV spectra of the LCMO/STO system, as-prepared and annealed.

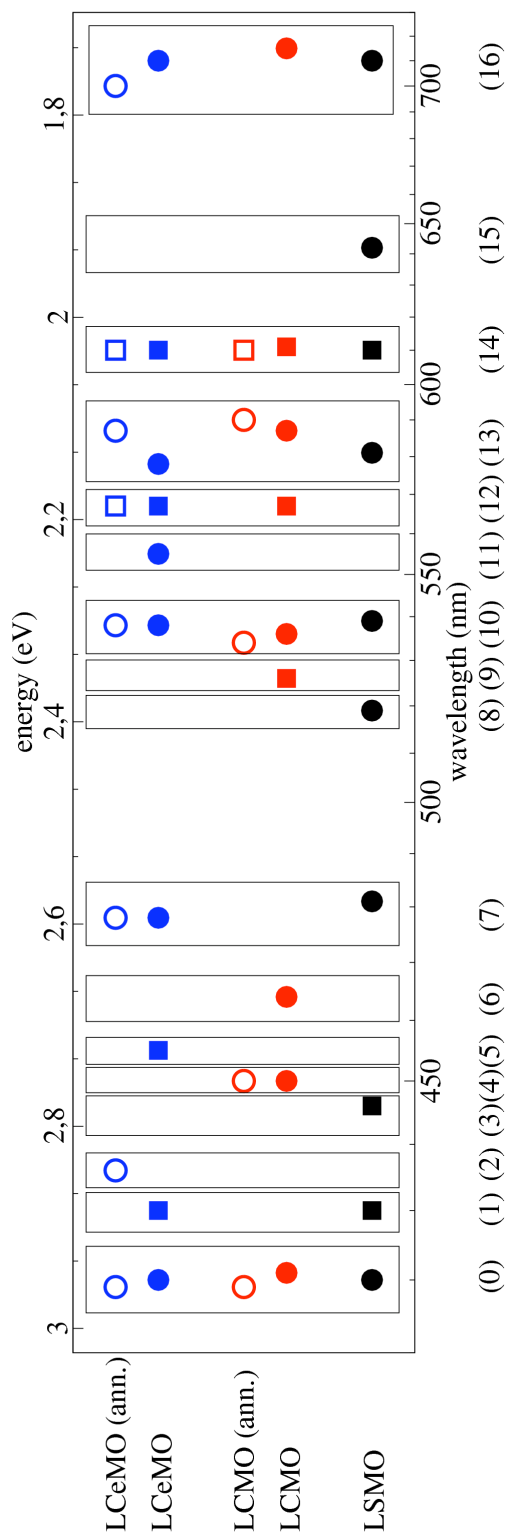


Figure B.6: Energetic positions of trap states in different manganite/STO systems. Circles and squares symbolize positive and negative slope changes, respectively.

B.2 Further theoretical treatment of the Kelvin probe current

B.2.1 Decomposition into harmonics

Here we present some further details on the analysis of the KELVIN probe current I (equation (3.7) from section 3.2.4.1), especially the calculation of the amplitudes of its harmonics. We start with the expression:

$$I = -\frac{\epsilon\epsilon_0 AU d_1 \omega \cos(\omega t)}{[d_0 + d_1 \sin(\omega t)]^2} \quad (\text{B.1})$$

with the quantities defined in section 3.2.4.1. In order to calculate the amplitude of the k^{th} harmonic of the current I , we perform a series expansion of the denominator of equation (B.1). Before, we define the following abbreviations:

$$a := \frac{d_1}{d_0} \quad (\text{B.2})$$

$$b := -\epsilon\epsilon_0 AU \omega \frac{d_1}{d_0^2} \quad (\text{B.3})$$

$$x := \omega t \quad . \quad (\text{B.4})$$

Those abbreviations simplify equation (B.1) to:

$$I = b \cos x (1 + a \sin x)^{-2} \quad . \quad (\text{B.5})$$

We use the following power series expansion [Bro83]:

$$(1 + z)^{-2} = 1 - 2z + 3z^2 - 4z^3 + 5z^4 - \dots = \sum_{n=0}^{\infty} (-1)^n (n+1) z^n \quad \text{for } |z| < 1 \quad . \quad (\text{B.6})$$

For our problem $z = a \sin x$ and the condition $|z| < 1$ is always fulfilled, because in the KELVIN probe we have $a < 1$, since the oscillation amplitude d_1 of the vibrating capacitor plate must be smaller than the average distance d_0 between the two plates [compare equation (B.2)].

With the knowledge of relation (B.6) we can rewrite the expression for I :

$$I = \sum_{n=0}^{\infty} b (-a)^n (n+1) \cos x \sin^n x \quad . \quad (\text{B.7})$$

We convert the sum (B.7) into expressions *without* powers of $\sin x$ using the *MATHEMATICA*[®] function *TrigReduce* up to $n = 10$. We rearrange the result to find the coefficients for the harmonics $\cos x$, $\sin 2x$, $\cos 3x$, $\sin 4x$, $\cos 5x$, $\sin 6x$, hoping that any *regular pattern* found there can be expanded to infinity. It turns out that the coefficients can be factorized as follows:

$$\cos x : \quad b(1 \cdot \frac{1}{1} \cdot 1 \cdot a^0 + 3 \cdot \frac{1}{4} \cdot 1 \cdot a^2 + 5 \cdot \frac{1}{16} \cdot 2 \cdot a^4 + 7 \cdot \frac{1}{64} \cdot 5 \cdot a^6 + 9 \cdot \frac{1}{256} \cdot 14 \cdot a^8 + 11 \cdot \frac{1}{1024} \cdot 42 \cdot a^{10} + \dots) \quad (\text{B.8})$$

$$\sin 2x : \quad -ba(2 \cdot \frac{1}{2} \cdot 1 \cdot a^0 + 4 \cdot \frac{1}{8} \cdot 2 \cdot a^2 + 6 \cdot \frac{1}{32} \cdot 5 \cdot a^4 + 8 \cdot \frac{1}{128} \cdot 14 \cdot a^6 + 10 \cdot \frac{1}{512} \cdot 42 \cdot a^8 + \dots) \quad (\text{B.9})$$

$$\cos 3x : \quad -ba^2(3 \cdot \frac{1}{4} \cdot 1 \cdot a^0 + 5 \cdot \frac{1}{16} \cdot 3 \cdot a^2 + 7 \cdot \frac{1}{64} \cdot 9 \cdot a^4 + 9 \cdot \frac{1}{256} \cdot 28 \cdot a^6 + 11 \cdot \frac{1}{1024} \cdot 90 \cdot a^8 + \dots) \quad (\text{B.10})$$

$$\sin 4x : \quad ba^3(4 \cdot \frac{1}{8} \cdot 1 \cdot a^0 + 6 \cdot \frac{1}{32} \cdot 4 \cdot a^2 + 8 \cdot \frac{1}{128} \cdot 14 \cdot a^4 + 10 \cdot \frac{1}{512} \cdot 48 \cdot a^6 + \dots) \quad (\text{B.11})$$

$$\cos 5x : \quad ba^4(5 \cdot \frac{1}{16} \cdot 1 \cdot a^0 + 7 \cdot \frac{1}{64} \cdot 5 \cdot a^2 + 9 \cdot \frac{1}{256} \cdot 20 \cdot a^4 + 11 \cdot \frac{1}{1024} \cdot 75 \cdot a^6 + \dots) \quad (\text{B.12})$$

$$\sin 6x : \quad -ba^5(6 \cdot \frac{1}{32} \cdot 1 \cdot a^0 + 8 \cdot \frac{1}{128} \cdot 6 \cdot a^2 + 10 \cdot \frac{1}{512} \cdot 27 \cdot a^4 + \dots) \quad (\text{B.13})$$

It is obvious that the coefficient of each harmonic is a sum of products, where each product contains four factors (three numeric factors and one power of a). While the 1st, 2nd, and 4th factors follow easy-to-find patterns, the third factors seem to be strange at the first glance. They are given once more in the following table [numbers in brackets were not shown in the expressions (B.8)-(B.13) but were also calculated with *MATHEMATICA*[®]]:

harmonic						
1 st	1	1	2	5	14	42
2 nd	1	2	5	14	42	
3 rd	1	3	9	28	90	
4 th	1	4	14	48	(165)	
5 th	1	5	20	75	(275)	
6 th	1	6	27	(110)	(429)	

It turns out that those factors follow the rule of the CATALAN triangle¹ [Wei07, Slo07], in which the number C_{lm} at position (l, m) is given by

$$C_{lm} = \frac{(l+m)!(l-m+1)}{m!(l+1)!} \quad (\text{B.14})$$

In our case, the coefficient of $\cos x$ contains $C_{10}, C_{21}, C_{32}, \dots$, for the coefficient of $\sin 2x$ the numbers $C_{20}, C_{31}, C_{42}, \dots$ are relevant, and so forth. After several rearrangements we get a compact equation for the k^{th} harmonic $I_{k\omega}$ of the KELVIN probe current I :

¹The numbers of the CATALAN triangle appear in many problems in combinatorics.

$$I_{k\omega} = kb \sum_{n=0}^{\infty} \left(\frac{a}{2}\right)^{2n+k-1} \frac{(2n+k)!}{n!(n+k)!} \{(-1)^{(k-1)/2} \Theta[(-1)^{(k+1)}] \cos(kx) + (-1)^{k/2} \Theta[(-1)^k] \sin(kx)\} \quad , \quad (\text{B.15})$$

with Θ being the HEAVISIDE function, which becomes necessary because the harmonics alternately follow a sine or cosine function. Furthermore, the terms $(-1)^{(k-1)/2}$ and $(-1)^{k/2}$ in the $\{\dots\}$ -term of equation (B.15) create the proper sign.

In order to remove the discontinuous HEAVISIDE function we use (i) $(-1)^{1/2} = i$, (ii) the EULER relations $\cos z = (e^{iz} + e^{-iz})/2$ and $\sin z = (e^{iz} - e^{-iz})/2i$, and (iii) the relations

$$\Theta[(-1)^{(k+1)}] + \Theta[(-1)^k] = 1 \quad (\text{B.16})$$

$$\Theta[(-1)^{(k+1)}] - \Theta[(-1)^k] = (-1)^{k-1} \quad , \quad (\text{B.17})$$

and finally obtain an alternative, more esthetic expression for $I_{k\omega}$:

$$I_{k\omega} = kb \sum_{n=0}^{\infty} \left(\frac{a}{2}\right)^{2n+k-1} \frac{(2n+k)!}{n!(n+k)!} \frac{i^{k-1}}{2} \{e^{ikx} + (-1)^{k-1} e^{-ikx}\} \quad . \quad (\text{B.18})$$

Formulae (B.15) and (B.18) have been cross-checked with *MATHEMATICA*[®] for $k = 1, 2, \dots, 6$ (and n up to 10) to see whether they reproduce the coefficients from the expressions (B.8)-(B.13).

The total current I can then be written as

$$I = \sum_{k=1}^{\infty} I_{k\omega} \quad . \quad (\text{B.19})$$

The expressions for the first- and second-harmonic part of I are given again [compare equations (3.8) and (3.9) in section 3.2.4.1]:

$$I_{\omega} = -\epsilon\epsilon_0 AU \omega \frac{d_1}{d_0^2} \cos(\omega t) \sum_{n=0}^{\infty} \left(\frac{1}{2} \frac{d_1}{d_0}\right)^{2n} \frac{(2n+1)!}{n!(n+1)!} \quad (\text{B.20})$$

$$I_{2\omega} = 2\epsilon\epsilon_0 AU \omega \frac{d_1}{d_0^2} \sin(2\omega t) \sum_{n=0}^{\infty} \left(\frac{1}{2} \frac{d_1}{d_0}\right)^{2n+1} \frac{(2n+2)!}{n!(n+2)!} \quad , \quad (\text{B.21})$$

where a, b and x have been substituted according to equations (B.2)-(B.4).

From relation (B.18) it becomes clear that the ratio d_1/d_0 determines how strong the

influence of higher harmonics on the total current is. The smaller the ratio d_1/d_0 the better the current I is represented by solely its first harmonic. The following subsection will demonstrate the role of this ratio more clearly.

B.2.2 Plots of the total current and its first two harmonics

To illustrate the nature of the current I , it is plotted together with I_ω , $I_{2\omega}$, and the sum $I_\omega + I_{2\omega}$ for three different ratios d_1/d_0 in figures B.7-B.9. The total current I is represented by the thicker gray line, the other quantities by thin black lines. The plate area A was set to $\frac{\pi}{4}(5 \cdot 10^{-3})^2 \text{ m}^2$, the average plate distance d_0 to 10^{-4} m , the voltage (which is the sum of the contact potential difference (CPD) and the bias voltage) U to 1 V, the dielectric constant ϵ to 1 for an air gap, and the frequency ω to $2\pi \cdot 175 \text{ Hz}$. All the values correspond to the true experimental conditions during this work (except the value for U , which varies during a measurement). For the calculation of I_ω and $I_{2\omega}$ equations (B.20) and (B.21) were employed with $n = 0, 1 \dots 20$. Higher summands have only marginal influence, which had been checked separately before. Even $n = 0, 1, 2$ would have given sound results. Only in the limit $d_1/d_0 \rightarrow 1$ decisively more summands become essential.

In figure B.7 the vibration amplitude d_1 was set to $2.5 \cdot 10^{-5} \text{ m}$ ($d_1/d_0 = 0.25$), which corresponds to the experimental conditions within this work. The amplitude of I is around 550 pA. The amplitude of the first harmonic I_ω is around 500 pA, while the second-harmonic amplitude $I_{2\omega}$ is smaller but still of the same order of magnitude: 150 pA. The sum of the first and the second harmonics is very close to the total current. If a CPD resolution of 1 mV is desired and the first harmonic is used for the feedback loop, a current as small as 500 fA has to be measured, which is, with a certain effort, possible.

For the calculation of the current signals in figure B.8 the ratio d_1/d_0 was enlarged to 0.8, which corresponds to a vibration amplitude of $8 \cdot 10^{-5} \text{ m}$. The total current becomes strongly asymmetric and the influence of higher harmonics to the total current clearly increases. The signal amplitudes are one order of magnitude higher than in the previously discussed case and the amplitudes of the first and the second harmonics are comparable.

The opposite effect can be observed when d_1/d_0 is decreased, as shown in figure B.9, where d_1/d_0 is only 0.05 ($d_1 = 5 \cdot 10^{-6} \text{ m}$). There, the total current consists mainly of its first harmonic. Thus, in an experiment, in which the second harmonic is used in the feedback loop (see discussion in section 3.2.4.1), the vibration amplitude should not be chosen too small with respect to the average plate distance.

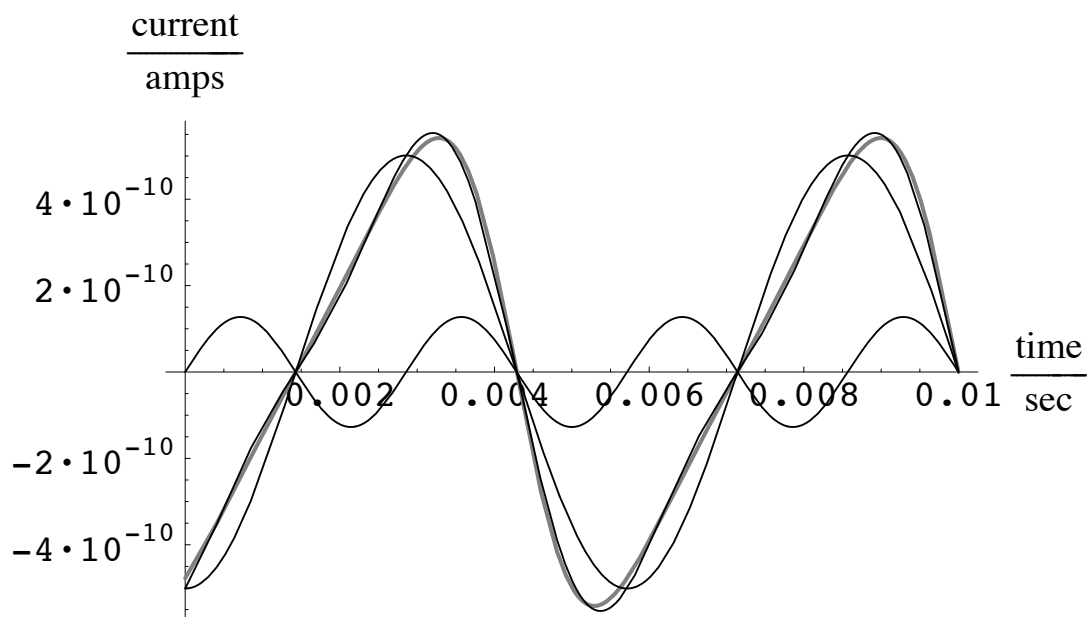


Figure B.7: KELVIN probe current (thick gray line), its first and second harmonics, as well as the sum of these two harmonics (thin black lines) for a ratio $d_1/d_0 = 0.25$. Both harmonics are strong enough to be used for feedback control.

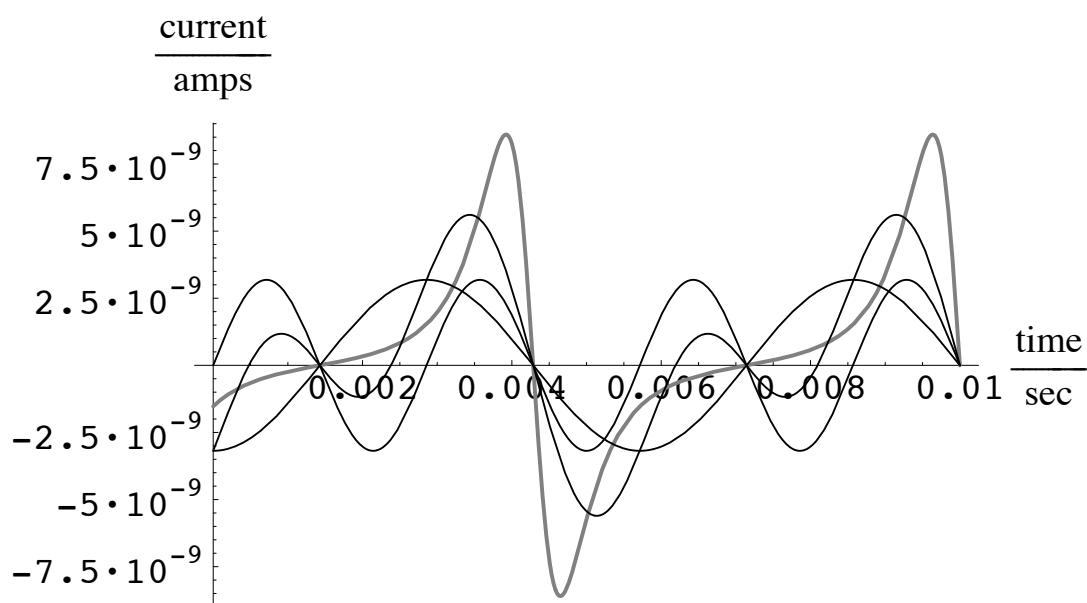


Figure B.8: KELVIN probe current (thick gray line), its first and second harmonics, as well as the sum of these two harmonics (thin black lines) for a ratio $d_1/d_0 = 0.8$. Both harmonics might be used for feedback control. To represent the strongly asymmetric total current correctly, also harmonics higher than the second would be necessary. Note that the amplitude of the k^{th} harmonic can be even higher than that of the $(k - 1)^{\text{th}}$ one if the ratio d_1/d_0 comes sufficiently close to 1.

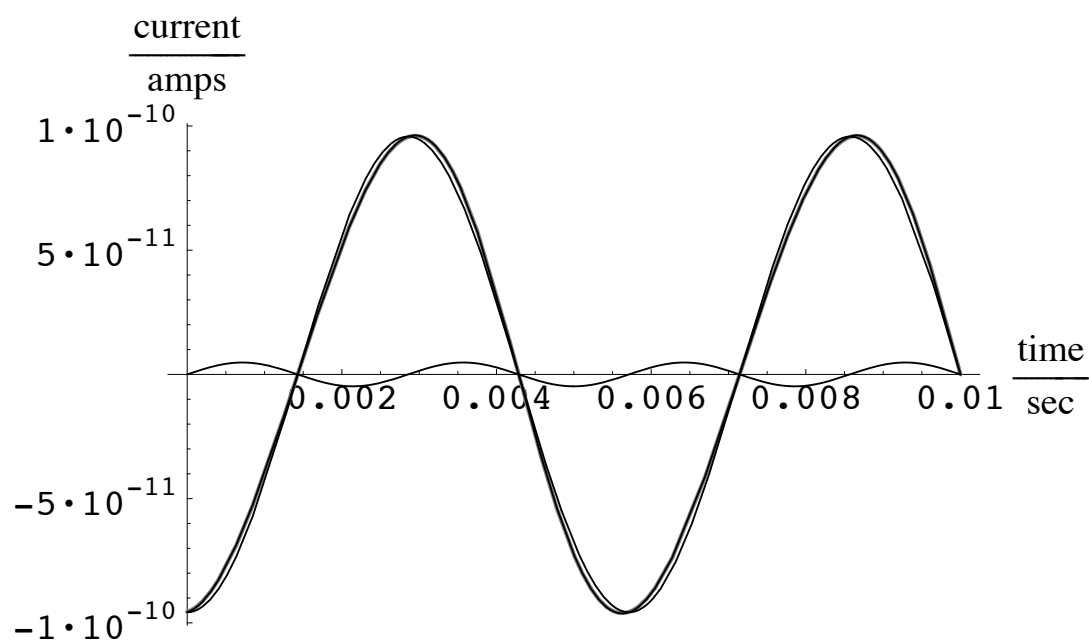
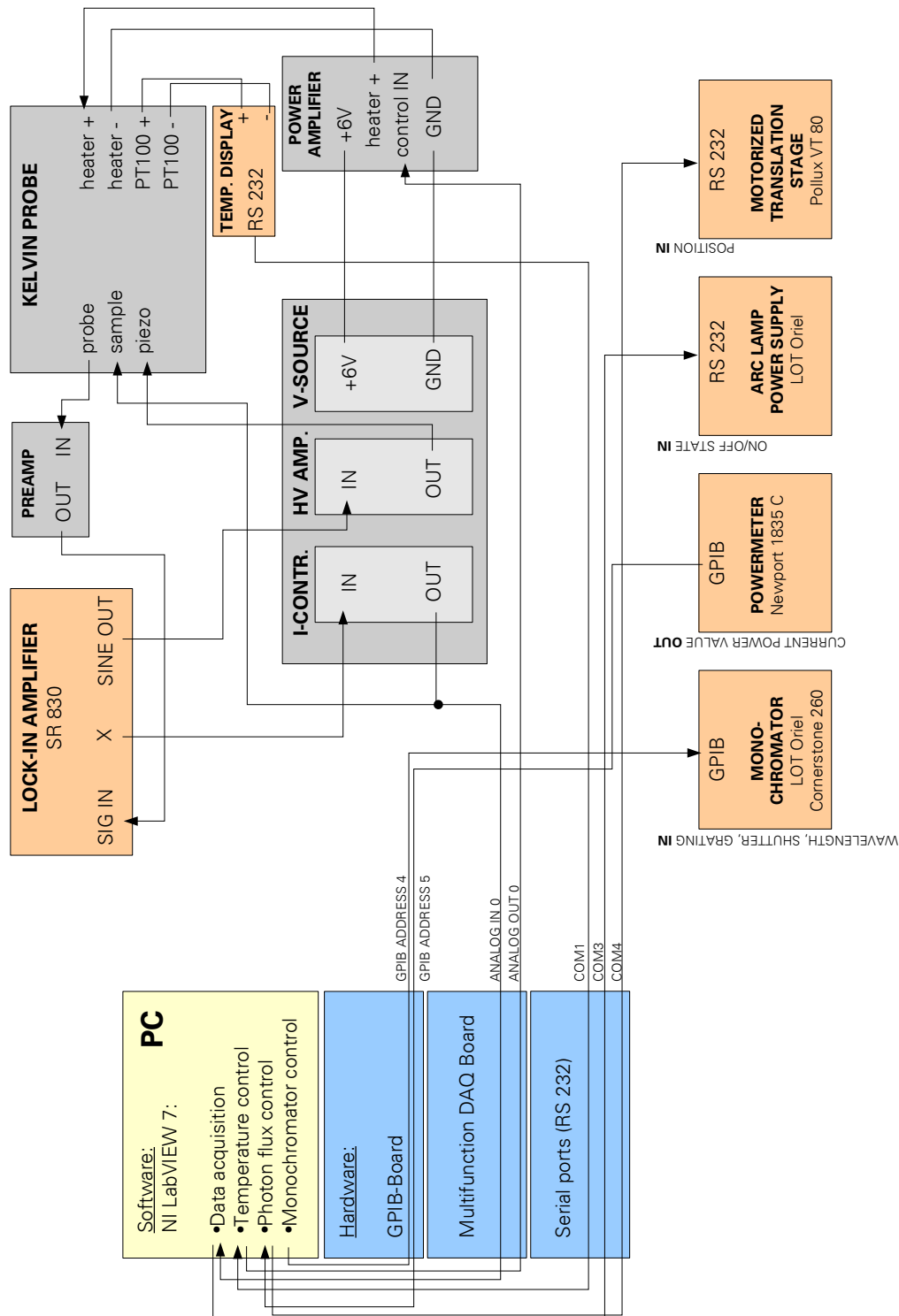


Figure B.9: KELVIN probe current (thick gray line), its first and second harmonics, as well as the sum of these two harmonics (thin black lines) for a ratio $d_1/d_0 = 0.05$. Here, the second harmonic is one order of magnitude smaller than the first harmonic and the total current is nearly identical to its first harmonic.

B.3 Signal flow diagram of the Kelvin probe SPV measurement



C Own publications

C.1 Journal articles

- E. Beyreuther, R. Beyer, J. von Borany, J. Weber: *Charge Storage in SiO₂ Layers with embedded Nanoclusters Studied by Scanning Capacitance Spectroscopy*, AIP Conf. Proc. 12th International Conference on Scanning Tunneling Microscopy/ Spectroscopy and Related Techniques, Vol. **696**, 720-727 (2003)
- R. Beyer, E. Beyreuther, J. von Borany, J. Weber: *Scanning capacitance microscopy and -spectroscopy on SiO₂ films with embedded Ge and Si nanoclusters*, Microelec. Eng. **72**, 207-212 (2004)
- C. Loppacher, U. Zerweck, S. Teich, E. Beyreuther, T. Otto, S. Grafström, L.M. Eng: *FM demodulated Kelvin probe force microscopy for surface photovoltage tracking*, Nanotechnology **15**, S1-S6 (2004)
- C. Thiele, K. Dörr, L. Schultz, E. Beyreuther, W.-M. Lin: *Piezo-electrically induced resistance modulations in La_{0.7}Sr_{0.3}MnO₃/ Pb(Zr,Ti)O₃ field effect devices*, Appl. Phys. Lett. **87**, 162512 (2005)
- R. Beyer, E. Beyreuther, J. von Borany, J. Weber: *Charge storage in silicon-implanted silicondioxide layers examined by scanning probe microscopy*, Thin Solid Films **513**, 159-165 (2006)
- E. Beyreuther, S. Grafström, L.M. Eng, C. Thiele, K. Dörr: *Surface Photovoltage Spectroscopy for the Investigation of Perovskite Oxide Interfaces*, Mat. Res. Soc. Symp. Proc. **902E**, T7.5.1-T7.5.11 (2006)
- E. Beyreuther, S. Grafström, L.M. Eng, C. Thiele, K. Dörr: *XPS investigation of Mn valence in lanthanum manganite thin films under variation of oxygen content*, Phys. Rev. B **73**, 155425 (2006)

C.2 Conference contributions

C.2.1 Talks

- E. Beyreuther, S. Grafström, L.M. Eng, C. Thiele, K. Dörr: *Surface Photovoltage Spectroscopy for the Investigation of Perovskite Oxide Interfaces*, MRS Fall Meeting, 28.11.-02.12.2005, Boston, USA
- E. Beyreuther, S. Grafström, L.M. Eng, C. Thiele, K. Dörr: *XPS investigation of the Mn valence in lanthanum manganite thin films under variation of the oxygen content*, DPG-Frühjahrstagung des AK Festkörperphysik, Dresden, 27.-31. 03. 2006
- E. Beyreuther, L.M. Eng: *Photoassisted Identification of Electronic Interface States in Complex Oxide Thin Films*, Materials Science & Technology 2006, Cincinnati, USA, 15.-19. 10. 2006

C.2.2 Posters

- E. Beyreuther, S. Grafström, C. Thiele, K. Dörr, L. Eng: *Investigation of the $\text{La}_{0.7}\text{Sr}_{0.3}\text{MnO}_3/\text{SrTiO}_3(100)$ -interface by X-ray photoelectron spectroscopy under optical excitation*, 2nd International Workshop on Oxidic Interfaces, Lutherstadt Wittenberg, 24.-26. 02. 2005
- E. Beyreuther, S. Grafström, C. Thiele, K. Dörr, L. Eng: *Investigation of the $\text{La}_{0.7}\text{Sr}_{0.3}\text{MnO}_3/\text{SrTiO}_3(100)$ -interface by X-ray photoelectron spectroscopy under optical excitation*, DPG-Frühjahrstagung des AK Festkörperphysik, Berlin, 04.-09. 03. 2005
- U. Zerweck, C. Loppacher, S. Teich, T. Otto, E. Beyreuther, S. Grafström, L.M. Eng: *FM demodulated Kelvin probe force microscopy for surface photovoltage tracking*, DPG-Frühjahrstagung des AK Festkörperphysik, Berlin, 04.-09. 03. 2005
- E. Beyreuther, S. Grafström, L.M. Eng, C. Thiele, K. Dörr: *Investigation of Manganite/Strontium Titanate Interfaces by Surface Photovoltage Spectroscopy*, DPG-Frühjahrstagung des AK Festkörperphysik, Dresden, 27.-31. 03. 2006
- E. Beyreuther, S. Grafström, L.M. Eng, C. Thiele, K. Dörr: *Tuning of the Mn valence in hole- and electron-doped LaMnO_3 thin films*, 9th International Symposium on Ferroic Domains (ISFD-9), Dresden, 26.-30. 06. 2006

- E. Beyreuther, S. Grafström, L.M. Eng, C. Thiele, K. Dörr: *Identification of electronic states at perovskite oxide interfaces*, 9th International Symposium on Ferroic Domains (ISFD-9), Dresden, 26.-30. 06. 2006

Acknowledgments

I am very grateful to:

- Prof. Lukas Eng for providing an excellent scientific environment, and for his encouraging and motivating enthusiasm.
- Prof. Susan Trolier-McKinstry and Prof. Ludwig Schultz for acting as referees.
- The SPM² group with all its current and former members for the friendly atmosphere, especially Dr. Stefan Grafström for all the advices, discussions, and proof reading of this thesis, and Sebastian Teich for the teamwork at our surface photovoltage setups.
- All the people from the Institute of Applied Photophysics, who have helped me in one or an other way during my time there.
- The group of Dr. Kathrin Dörr at the IFW Dresden, especially Dr. Christian Thiele and Jong-Woo Kim for providing the manganite thin film samples. Special thanks to Kathrin for many discussions on electron- and hole-doped manganites and all the fruitful ideas.
- The German Research Foundation (FOR520) and the Saxonian Ministry for Science and Art for financial support.
- My family, especially my husband Stefan, my parents Ute and Roland Beyreuther, and my grandparents, for their continuous love, support, and encouragement.

Erklärung

- Hiermit versichere ich, dass ich die vorliegende Arbeit ohne unzulässige Hilfe Dritter und ohne Benutzung anderer als der angegebenen Hilfsmittel angefertigt habe; die aus fremden Quellen direkt oder indirekt übernommenen Gedanken sind als solche kenntlich gemacht. Die Arbeit wurde bisher weder im Inland noch im Ausland in gleicher oder ähnlicher Form einer anderen Prüfungsbehörde vorgelegt.
- Die vorliegende Arbeit wurde am Institut für Angewandte Physik, Teilinstitut Photophysik, der Technischen Universität Dresden unter wissenschaftlicher Betreuung von Prof. Dr. Lukas Eng angefertigt.
- Ein früheres erfolgloses Promotionsverfahren hat nicht stattgefunden.
- Ich erkenne die Promotionsordnung der Fakultät Mathematik und Naturwissenschaften der Technischen Universität Dresden an.

Dresden, den 26.07.2007

Elke Beyreuther